

Long-term variability of internal  
waves and diapycnal mixing:  
The role of the North Atlantic  
Deep Western Boundary Current

Janna Köhler

Universität Bremen, 2013



# Long-term variability of internal waves and diapycnal mixing: The role of the North Atlantic Deep Western Boundary Current

Vom Fachbereich für Physik und Elektrotechnik der  
Universität Bremen genehmigte Dissertation  
zur Erlangung des akademischen Grades  
Doktor der Naturwissenschaften (Dr. rer. nat.)

von

Dipl. Phys. Janna Köhler

aus Bremen

1. Gutachterin: Prof. Dr. Monika Rhein
2. Gutachter: Prof. Dr. Torsten Kanzow

Eingereicht am: 23.10.2013

Tag des Promotionskolloquiums: 9.12.2013



# Zusammenfassung

Der Einfluss des Tiefen Westlichen Randstroms (DWBC) auf das interne Wellenfeld sowie auf die vertikale Vermischung über dem Kontinentalhang bei  $16^\circ$  N im westlichen tropischen Atlantik wird anhand von Zeitreihen von zwei Verankerungen (durchgängig von 2000 bis 2005) in Kombination mit Schiffsmessungen von fünf Reisen untersucht. Aufgrund der hohen zeitliche Variabilität in der Strömungsintensität und der damit verbundenen Strömungsgeschwindigkeit, bietet diese Region ideale Voraussetzungen für die Untersuchung des direkten Einflusses starker Strömungen sowie deren Interaktion mit der Topographie auf die Erzeugung von internen Wellen und die Intensität von vertikaler Vermischung.

Die Verankerungsdaten beinhalten 2-stündliche Geschwindigkeitsmessungen sowie Temperatur/Leitfähigkeit-Zeitreihen mit einer zeitlichen Auflösung von 5 – 20 min. Aufgrund dieser kurzen Messintervalle werden Zeitskalen von der niederfrequenten Variabilität des großräumigen Randstroms, welcher für die Erzeugung der internen Wellen verantwortlich ist, bis hin zu hochfrequenter vertikaler Vermischung aufgrund von brechenden internen Wellen aufgelöst. Diapyknische Vermischungsraten wurden mit Hilfe einer Feinstrukturparameterisierung bestimmt und zeigen erhöhte Vermischungsraten von bis zu  $10^{-3} \text{ m}^2 \text{ s}^{-1}$  in den untersten 1500 m zu Zeiten eines starken DWBC (maximale Strömungsgeschwindigkeiten von bis zu  $50 \text{ cm s}^{-1}$ ). Ein erhöhtes Verhältnis von Geschwindigkeitsscherung zu Dehnung des Dichtefeldes während dieser Perioden ist ein Zeichen für die Zunahme von niederfrequenten internen Wellen während Zeiten hoher Strömungsgeschwindigkeiten.

Aus Verankerungsdaten bestimmte Variabilität im hochfrequenten Bereich wird als Indikator für vertikale Vermischung genutzt und ist signifikant mit der Stärke des Randstromes korreliert. Dies belegt ebenfalls eine Zunahme von vertikaler Vermischung zu Zeiten eines starken DWBC.

Während dieser Perioden zeigen besonders unterhalb von 1200 m Spektren der horizontalen Geschwindigkeiten sowie von verfügbarer potentieller Energie einen Anstieg in der Energie von internen Wellen vor allem im niederfrequenten Bereich

---

nahe der Coriolis Frequenz  $f$ . Diese Zunahme ist dabei stärker an der küstennahen Verankerung.

Die Interaktion des DWBC mit dem Kontinentalhang westlich der Verankerungen, wo die lokale Wassertiefe der Tiefe des Maximums des DWBC entspricht, wird als Erzeugungsmechanismus vorgeschlagen, welcher zu der beobachteten Zunahme in der Energie insbesondere von niederfrequenten internen Wellen sowie der Intensität der vertikalen Vermischung führt; Ausbreitungspfade, die für am Kontinentalhang erzeugte interne Wellen abgeschätzt wurden, stimmen gut mit den beobachteten Änderungen in den Spektren der internen Wellen in den unterschiedlichen Tiefen überein. Weiterhin wurde die vertikale Energieausbreitung mit Hilfe von Rotationspektren von LADCP Messungen bestimmt und zeigt eine Divergenz der Energieflüsse in der ungefähren Tiefe des DWBC Kerns. Oberhalb des Kerns herrscht eine aufwärtsgerichtete Ausbreitungsrichtung vor, wohingegen darunter im Mittel ein abwärtsgerichteter Energiefluss dominiert. Dies ist in guter Übereinstimmung mit den abgeschätzten Ausbreitungscharakteristika der (niederfrequenten) internen Wellen, die westlich der Verankerungen durch die Interaktion des DWBC mit dem Kontinentalhang erzeugt wurden.

# Abstract

Five years of continuous mooring data combined with CTD/LADCP measurements from five cruises are used to investigate the influence of the Deep Western Boundary Current (DWBC) on the internal wave field and associated vertical mixing at the continental slope at 16°N in the western Atlantic. As the temporal variability in current strength and corresponding flow speeds within the DWBC is very high, this geographic location provides an ideal setting to analyze the direct influence of strong currents or their interaction with topography on the generation of internal waves and the magnitude of vertical mixing rates.

The mooring data include two-hourly rotor current meter measurements and temperature/conductivity time series with high temporal resolution of 5-20 minutes. Thus, the data resolve timescales ranging from the low-frequency variability of the large scale DWBC that generates internal waves due to interactions with the topography, to high frequency vertical mixing induced by breaking internal waves. Diapycnal diffusivities obtained from a finescale parameterization show elevated mixing rates of up to  $10^{-3} \text{ m}^2 \text{ s}^{-1}$  in the bottommost 1500 m during times of a strong DWBC where velocities at the mooring site reach up to  $50 \text{ cm s}^{-1}$ . Enhanced shear to strain ratios during these times denote an increase in low frequency waves during phases of strong flow.

Variability in the high frequency range calculated from mooring data, considered as a proxy for turbulent mixing, is significantly correlated with the DWBC strength above the continental slope which also indicates a pronounced increase of vertical mixing during strong flow.

During these periods spectra of horizontal velocity and internal wave available potential energy change substantially at depths below 1200 m and show a strong increase of energy in internal waves particularly in the near inertial frequency band. This increase is stronger at the mooring over the continental slope than slightly more offshore over the continental rise. The generation of low frequency, near inertial waves due to the interaction of the DWBC with the slope topography

---

to the west of the moorings where the local water depth equals the depth of the DWBC core is the mechanism proposed for the generation of the observed intensification of low frequency waves and enhanced vertical mixing rates; ray paths estimated for internal waves generated at the continental slope agree well with the observed spectral changes at different depths. Furthermore the vertical energy propagation direction estimated from rotary spectra of shipboard LADCP measurements shows a divergence at depths approximately corresponding to the depth of the DWBC core. Above the core the energy propagation is dominantly upward whereas it is downward below. This is consistent with the estimated ray path for (near inertial) internal waves generated by the interaction of the DWBC core with the slope topography to the west of the moorings.

# Contents

<b>1</b>	<b>Introduction</b>	<b>1</b>
<b>2</b>	<b>Internal waves and diapycnal mixing</b>	<b>9</b>
2.1	Internal waves . . . . .	9
2.1.1	Critical topographic slopes . . . . .	12
2.1.2	Lee waves . . . . .	13
2.1.3	Critical layers . . . . .	15
2.1.4	Resonant interactions . . . . .	16
2.1.5	The Garrett-Munk model . . . . .	17
2.2	Turbulence and vertical mixing . . . . .	19
<b>3</b>	<b>Oceanographic setting and the mooring array</b>	<b>25</b>
<b>4</b>	<b>Data</b>	<b>33</b>
4.1	Timeseries data . . . . .	33
4.2	Hydrographic data . . . . .	38
<b>5</b>	<b>Methodology</b>	<b>39</b>
5.1	Finescale parametrization of diapycnal diffusivities . . . . .	39
5.2	Internal wave available potential energy . . . . .	45
5.3	Internal wave spectra . . . . .	47
5.4	Rotary spectra . . . . .	48
<b>6</b>	<b>Boundary current induced mixing</b>	<b>51</b>
<b>7</b>	<b>Variability in the internal wave field induced by the DWBC</b>	<b>55</b>
7.1	Internal wave kinetic energy . . . . .	55

7.1.1	Mean spectra of internal wave kinetic energy . . . . .	55
7.1.2	Velocity dependence of internal wave kinetic energy . . . . .	57
7.2	Internal wave available potential energy . . . . .	61
7.2.1	Mean spectra of internal wave potential energy . . . . .	61
7.2.2	Velocity dependence of internal wave available potential energy	63
<b>8</b>	<b>Discussion</b>	<b>69</b>
8.1	Diapycnal mixing . . . . .	69
8.2	Internal wave energy from timeseries . . . . .	70
8.3	High frequency variability as proxy for mixing intensity . . . . .	71
8.4	Vertical propagation of internal waves . . . . .	76
<b>9</b>	<b>Summary and Conclusions</b>	<b>81</b>
<b>10</b>	<b>Outlook</b>	<b>85</b>
	<b>Bibliography</b>	<b>89</b>

# 1 | Introduction

Internal waves - waves in the interior of the ocean - induced by disturbances of the steady background state are important mechanism for the horizontal and vertical transport of energy. Formerly perceived as noise distorting the real signal, the challenge to identify and quantify the sources and generation processes of internal waves is now ongoing for several decades. Nevertheless this is a well worthwhile endeavour not only for their inherent interesting, complex three dimensional dynamics, their generation, interaction and dissipation characteristics but also for their important role in transport processes of e.g. heat, energy, nutrients or sediments.

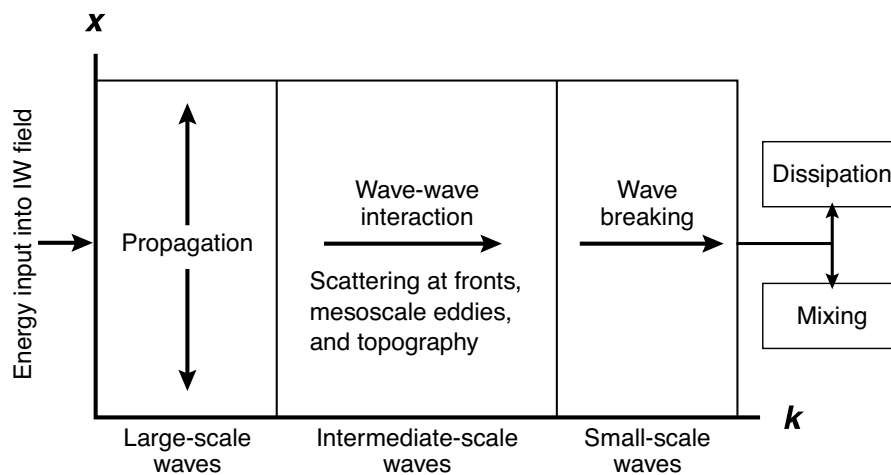


**Figure 1.1:** Large scale internal waves are generated and propagate in physical ( $x$ ) and wavenumber ( $k$ ) space until they finally break and vertical mixing and dissipation is induced. Reproduced and modified from Müller and Briscoe (2000)

Large scale internal waves are generated e.g by wind, tides or flow-topography interactions. As they propagate away from their generation site, energy is transferred to smaller scales by nonlinear wave-wave interactions and interaction with fronts, eddies or topography until they finally break and turbulent mixing is induced (Fig. 1.1). In total internal waves in the global ocean are estimated to

contain an energy of  $14 \times 10^{18}$  J (Fig. 1.2). Because of the energy transport over large physical and wavenumber scales, internal waves are an important link in the closure of the energy budget of the ocean circulation (Fig. 1.2), eventually providing the energy needed for turbulent diapycnal mixing.

Turbulent diapycnal mixing plays an important role in the oceanic circulation system: In polar regions cold and dense water is formed by convection, sinks down and spreads in the deep ocean. Without a subsequent upward transport mechanism, this cold and dense water would eventually fill up the entire ocean basins and heating by the sun would only induce a very shallow surface current (Wunsch and Ferrari, 2004). Even though part of this deeper water masses are brought back up by Ekman pumping particularly in the Southern Ocean due to the strong westerly winds, vertical mixing was found to be a main driver in the upkeep of the observed ocean stratification and current systems (Kuhlbrodt et al., 2007). If the formation of deep water would have to be solely balanced by vertical mixing, Munk (1966) estimated from an advective/diffusive balance model (as already used by Wyrтки, 1961) that in the global mean a diapycnal diffusivity of  $K_\rho = 10^{-4} \text{ m}^2 \text{ s}^{-1}$  is needed to maintain the observed abyssal stratification. However measured mixing rates were shown to be highly variable. While in the oceans interior away from boundaries they were found to be about an order of magnitude lower than this estimate (Ledwell et al., 1993; Kunze and Sanford, 1996; Ledwell et al., 2010), it is exceeded by two orders of magnitude at mixing hot spots like e.g. rough topography (e.g. Polzin et al., 1997; Garabato et al., 2004). The combination of these locally significantly enhanced mixing rates and Ekman upwelling is likely to compensate for the lesser diapycnal mixing observed in the ocean interior in order to close the energy budget of the overturning circulation.

The strength of vertical mixing is currently observationally estimated by mainly three techniques: in large scale tracer release experiments (e.g. Ledwell et al., 1993; Ledwell et al., 2000, 2010; Watson et al., 2013) tracers such as sulphur hexafluoride are induced at specific density interfaces and their dispersal is measured during follow up cruises several months later. A finescale parameterization based on wave-wave interaction theory and subsequent wave breaking inducing vertical mixing uses shear and strain spectra obtained from hydrographic measurements to infer the intensity of vertical mixing (e.g. Gregg, 1989; Polzin et al., 1995; Gregg

et al., 2003; Kunze et al., 2006). Energy dissipation rates are obtained directly using microstructure profilers measuring temperature or velocity fluctuations with a very high temporal resolution (e.g. Carter and Gregg, 2002; St. Laurent et al., 2012; Polzin et al., 1997).

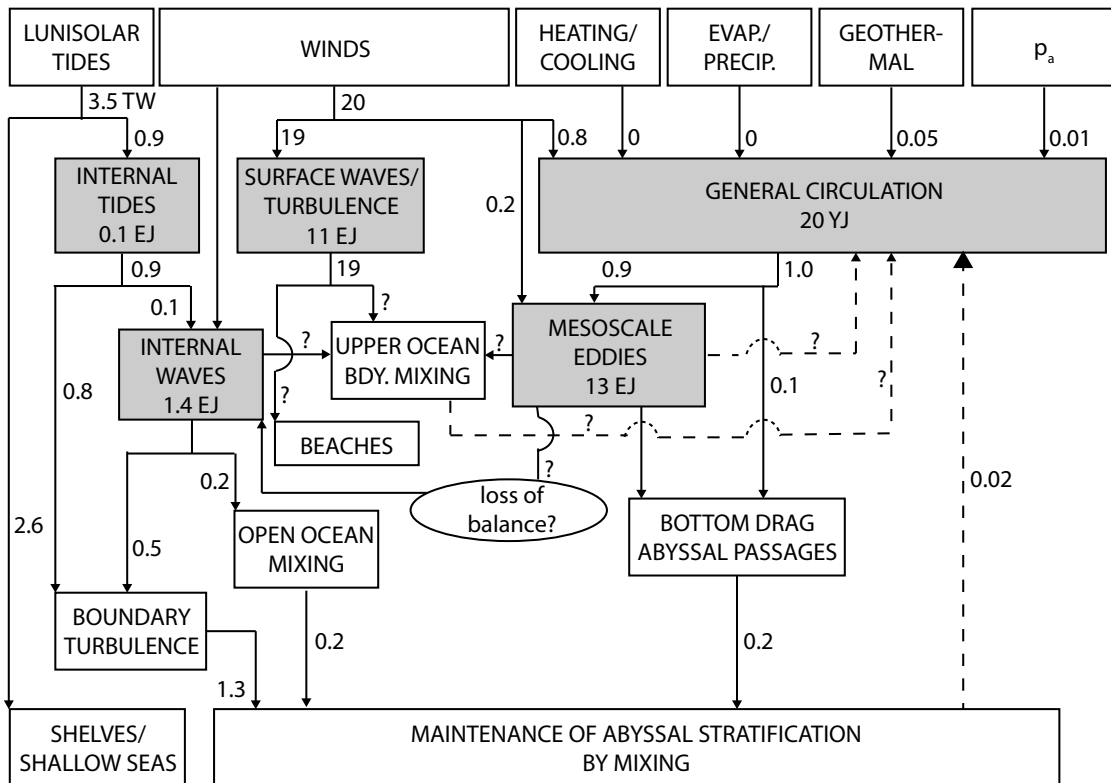


**Figure 1.2:** Flowchart of the energy budget of the global ocean circulation with EJ denoting exajoules ( $10^{18}$  J), YJ denoting yottajoules ( $10^{24}$  J) and TW denoting terawatts ( $10^{12}$  W). Possible energy sources in the top row; all given estimates have uncertainties of a factor 2 to possibly up to 10. Energy that is returned to the main circulation by mixing is denoted by dashed lines. Reproduced from Wunsch and Ferrari (2004); stated internal wave energy was modified following Thorpe (2005).

The strength of vertical mixing induced by the breaking of internal waves depends on the energy in the internal wave field that is related, among others, to tides. Internal tides are generated by the interaction of barotropic tides e.g. with topography and subsequently their energy is propagated from the internal tidal frequency through the internal wave continuum until finally diapycnal mixing is induced (Fig. 1.3). Thereby primarily low mode internal waves are generated at

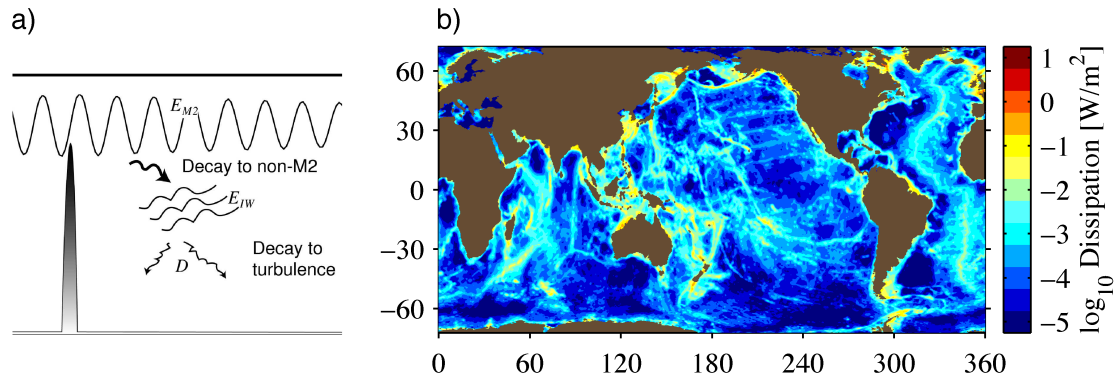


**Figure 1.3:** a) Schematic sketch of the energy cascade of tidal internal waves generated at a steep ridge. Energy is cascaded from the internal tide frequency to the internal wave continuum ( $E_{IW}$ ) and cascaded to turbulence. From Klymak et al. (2006) b) Model results for global tidal energy dissipation including bottom and internal wave drag. From Jayne and St. Laurent (2001)

topographic scales of 20 km to 100 km which will propagate away and not dissipate locally, whereas over rougher topography e.g. at the Mid Atlantic Ridge (MAR) higher modes are generated and dissipated locally (St. Laurent and Garrett, 2002). Therefore strongest mixing rates induced by internal tides occur over rough topography and can also show a spring neap cycle (Carter and Gregg, 2002; Klymak et al., 2006) or a tidal cycle (Walter et al., 2010). In total tides provide up to 0.9 TW for global abyssal mixing (Fig. 1.2, Munk and Wunsch, 1998). Other factors influencing the mixing intensity are topographic roughness (Fig. 1.4, Kunze and Sanford, 1986; Polzin et al., 1997; Eriksen, 1998; Ledwell et al., 2000; Mauritzen et al., 2002; Shcherbina et al., 2003; Garabato et al., 2004; Waterman et al., 2012; Sheen et al., 2013), meso-scale eddies (Tandon and Garrett, 1996; Eden and Greatbatch, 2008), the position of fronts (D’Asaro et al., 2011; Johnston et al., 2011; Walter and Mertens, 2013) and the strength of geostrophic flow impinging on small-scale topography (Nikurashin and Ferrari, 2010a,b; Nikurashin et al., 2013; Watson et al., 2013). Diapycnal diffusivities in the Deep Western Boundary Current (DWBC) in the tropical Atlantic obtained from a parameterization based on the internal wave spectrum strongly increase with increasing background velocities (Stöber et al., 2008). Elevated diapycnal diffusivities were also observed in the DWBC of the subpolar North Atlantic by Walter et al. (2005) and by Lauderdale

et al. (2008) whereas comparatively low mixing rates ( $K_\rho \approx 10^{-5} \text{ m}^2 \text{ s}^{-1}$ ) in the open ocean were obtained from a tracer release experiment west of the Canary Islands (Ledwell et al., 1993) or in the Antarctic Circumpolar Current west of Drake Passage (Ledwell et al., 2010).

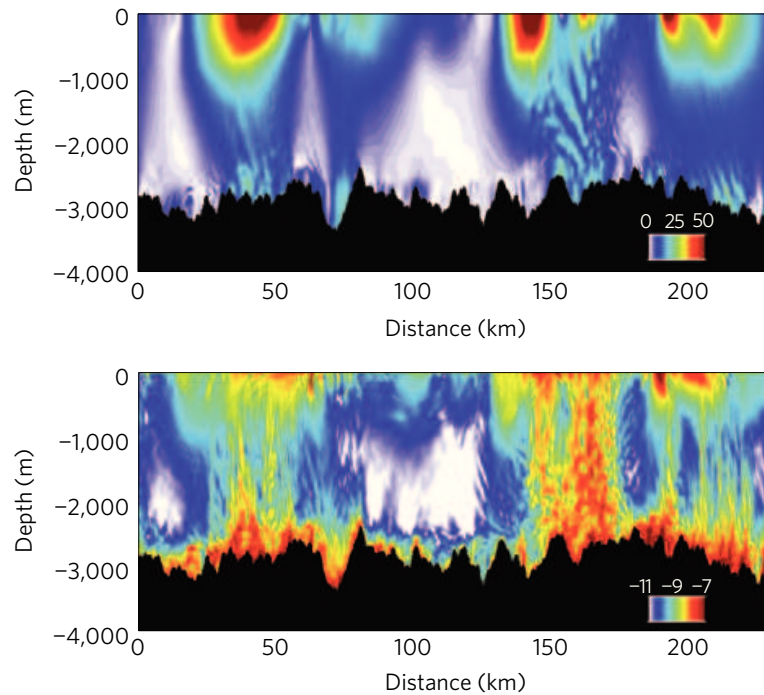


**Figure 1.4:** Snapshot of model results for kinetic energy ( $\text{cm s}^{-1}$ , upper panel) interacting with rough topography and inducing energy dissipation ( $\log_{10} \text{ W kg}^{-1}$ , lower panel) in the Southern Ocean. Energy dissipation is enhanced in the deep ocean above topography, in the interior in regions of enhanced wave activity and at the surface in regions of eddies and fronts. From Nikurashin et al. (2013)

However, internal waves not only play an important role in the upkeep of the ocean's stratification and current system by providing the energy needed for diapycnal mixing, but also for e.g. biological processes as they for example influence the vertical transport of nutrients into the euphotic zone (Sandstrom and Elliott, 1984) and they effect the shape of the ocean floor by influencing sediment transports (Friedrichs and Wright, 1995).

The shape of the internal wave field in frequency and wavenumber space was found to be quite universal away from direct generation sites and the semi-empirical

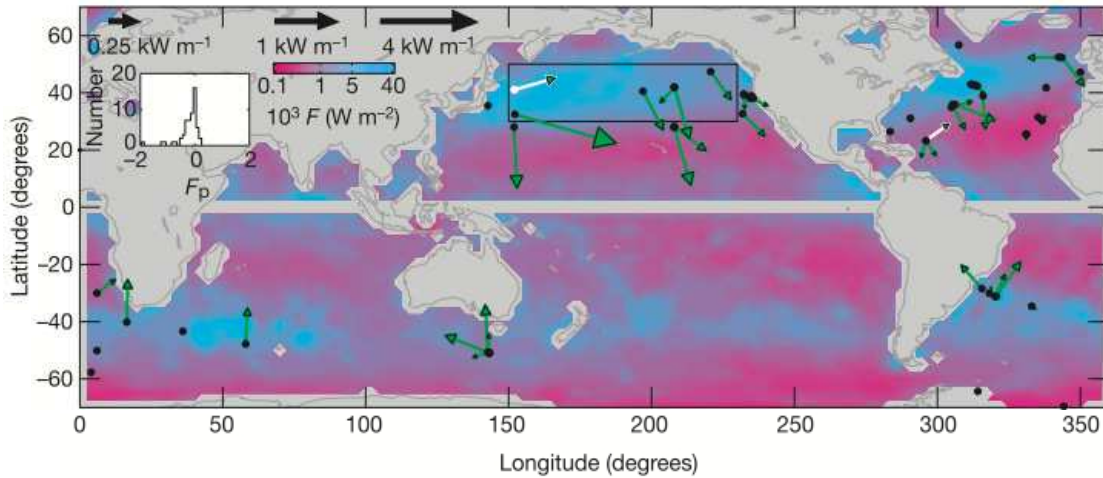


**Figure 1.5:** Annual mean of depth-integrated near inertial energy flux from modes 1 and 2 from 60 historical moorings. Arrow length is logarithmically related to the flux and poleward flux is denoted by white arrows. The majority of the observed energy fluxes is equatorward in good agreement with linear internal wave theory permitting the poleward propagation of inertial waves. Colormap shows annual mean energy input from the wind to near inertial mixed layer motions. From Alford (2003)

Garrett-Munk (GM) spectrum (Garrett and Munk, 1972a) is widely used as a representation of the universal internal wave spectrum. However, local and temporal characteristics of the internal wave field were shown to vary strongly in response to local properties and on timescales from days to months; the local buoyancy frequency for example influences the slope of the continuum spectrum (van Haren et al., 2002). The wind induces changes in horizontal near inertial internal wave energy fluxes (Fig. 1.5, Alford, 2003; Alford and Whitmont, 2007) and thereby also imposes a seasonal cycle on the energy in near inertial waves particularly close to the surface with a maximum in local winter (Alford and Whitmont, 2007). A near inertial gravity wave was found to radiate away from the Subtropical Front in the North Pacific (Alford et al., 2013) and topographic roughness, the stratification and the velocity of the mean flow control the generation of internal lee waves (Nikurashin and Ferrari, 2010a,b; Scott et al., 2011).

In a theoretical study Nikurashin and Ferrari (2010b) found that geostrophic and near inertial currents flowing over rough topography can not only generate steady lee waves, but can also lead to a positive feedback for the generation of near in-

---

ertial waves and their harmonics. Energy is transferred to the inertial frequency  $f$  via a triad interaction between lee waves and waves with harmonic frequencies of  $f$  that are forced by inertial currents. Subsequent breaking of the near inertial waves deposits their momentum and increases the inertial oscillations in the mean flow (Nikurashin and Ferrari, 2010b). A corresponding disproportionately high increase in near inertial wave energy due to interactions of deep reaching eddies with bottom topography at the East Pacific Rise was observed in a study by Liang and Thurnherr (2012). Nikurashin and Ferrari (2010b) further showed that the vertical shear associated with the inertial oscillations promotes enhanced wave breaking which then induces increased vertical mixing. St. Laurent et al. (2012) found elevated vertical mixing rates in the Drake passage which might be related to internal waves and their subsequent breaking induced by the processes proposed by Nikurashin and Ferrari (2010b).

Several studies have already been carried out to investigate the spatial and depths distribution of internal wave energy and vertical mixing intensity (e.g. Eriksen, 1998; Polzin et al., 1997; Ledwell et al., 2000; Jayne and St. Laurent, 2001; Garabato et al., 2004; Klymak et al., 2006; Kunze et al., 2006; Nikurashin and Ferrari, 2011; Scott et al., 2011; Alford et al., 2011). However besides seasonally and tidally induced changes their temporal variability is not well known. In this study five years of continuous mooring data permit such an observational analysis of temporal variations in internal wave energy and the analysis of the direct influence of strong currents and their interaction with (slope) topography on the internal wave field.

The generation of low frequency, near inertial waves by the interaction of the DWBC with the topography of the continental slope and an associated increase of vertical mixing intensity will be the main subject of this study. The strength and position of the Atlantic DWBC off the Lesser Antilles is highly variable over time (Kanzow et al., 2006; Rhein et al., 2004). Therefore this location is ideal to study the variability of the internal wave field and its frequency content in relation to changes in the current strength using mooring data. Changes in the internal wave field, induced by the DWBC, might lead to changes in turbulent mixing and temporal variability in diapycnal diffusivities (derived from a finescale parameterization) will be investigated in relation to the DWBC strength.

An introduction to the theoretical background of internal waves and diapycnal mixing will be given in Chapter 2 followed by a description of the oceanographic setting of the study area and a brief overview of the mooring array deployed in the framework of the Meridional Overturning Variability Experiment (MOVE) (Kanzow et al., 2006, 2008) in Chapter 3. An extensive data set (Chapter 4) is provided by five years of continuous measurements of temperature, salinity, pressure and horizontal velocities from two moorings at the continental slope and rise in the DWBC at 16°N in combination with shipboard Conductivity-Temperature-Depth (CTD)/ Lowered Acoustic Doppler Current Profiler (LADCP) data (Rhein et al., 2004) from five cruises in the same area. The mooring instrumentation permits the investigation of the influence of the DWBC strength and position (Chapter 5.3) on the internal wave field on a long time period and over a large depth range. Shipboard CTD/LADCP measurements are used to obtain diapycnal diffusivities  $K_\rho$  from an application of a finescale parameterization for the diffusivity for different flow situations at the mooring locations (Chapters 5.5.1 and 6). Changes in the internal wave spectrum of horizontal velocities and available potential energy induced by the variability in DWBC strength at the mooring locations are analyzed in Chapters 5.5.2, 5.3 and 7. Results will be discussed in Section 8 including an estimation of the vertical energy propagation direction during different DWBC phases deduced from rotary spectra as well as an estimation of a direct correlation between internal wave energy and proxies for vertical mixing intensities during the entire five years of mooring data considered in this study. An outlook on further possible studies on the generation of internal waves and vertical mixing is given in Chapter 10.

## 2 | Internal waves and diapycnal mixing

### 2.1 Internal waves

Internal waves have a variety of energy sources and generation processes. Major generation mechanisms are e.g. a fluctuating wind stress at the ocean surface

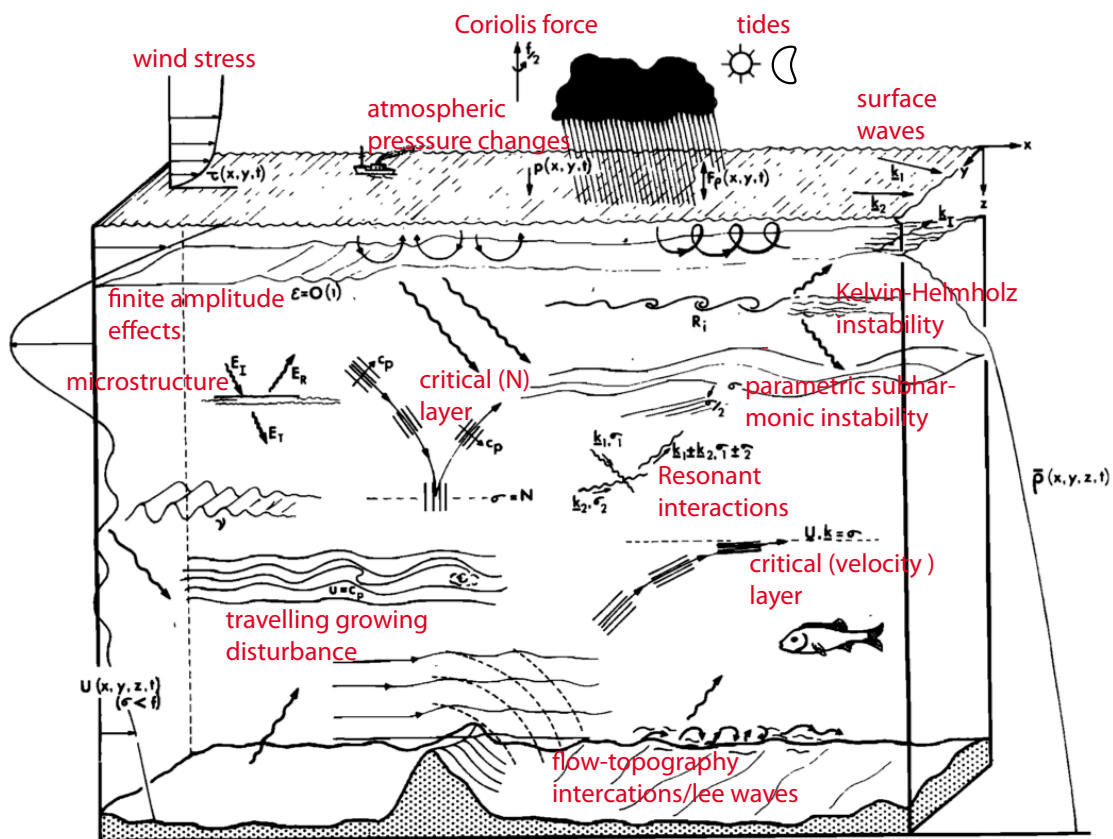


**Figure 2.1:** Sketch showing various processes of internal wave generation, propagation, interaction and breaking. Modified from Thorpe (1975)

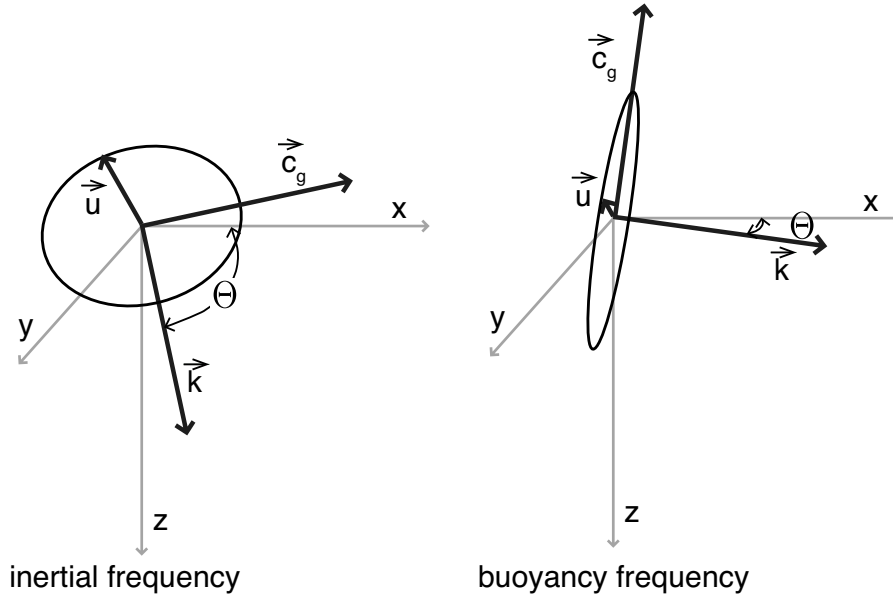


**Figure 2.2:** Wavenumber vector  $\vec{k} = (k, m)$ , group velocity  $\vec{c}_g$  and hodograph of particle velocity  $\vec{u}$  near the inertial frequency  $f$  and the buoyancy frequency  $N$ . Reproduced from Garrett and Munk (1979)

inducing downward propagating low frequency, near inertial (near the Coriolis frequency  $f$ ) internal waves; they can be generated by interactions of the barotropic tides with the bottom topography inducing internal waves with tidal frequencies (baroclinic tides) or large scale currents interacting with topography (Figure 2.1). Once the internal waves are generated, they undergo a multitude of specific propagation (Chapters 2.1.1 and 2.1.3) and interaction processes (Chapter 2.1.4) which induce a propagation of energy through wavenumber space toward smaller scales until the internal waves finally break and cause vertical mixing and dissipation (Chapter 2.2).

Internal waves horizontally and vertically radiate energy and momentum through the ocean, thereby changing the density field as they distort (i.e. vertically displace) the background density interfaces. These vertical displacements can reach up to some hundred meters, depending on the internal wave energy and the local stratification whereas horizontal scales of internal waves range in the order of  $10^2 - 10^3$  m.

Using the boussinesq approximation and the equations of motion the dispersion

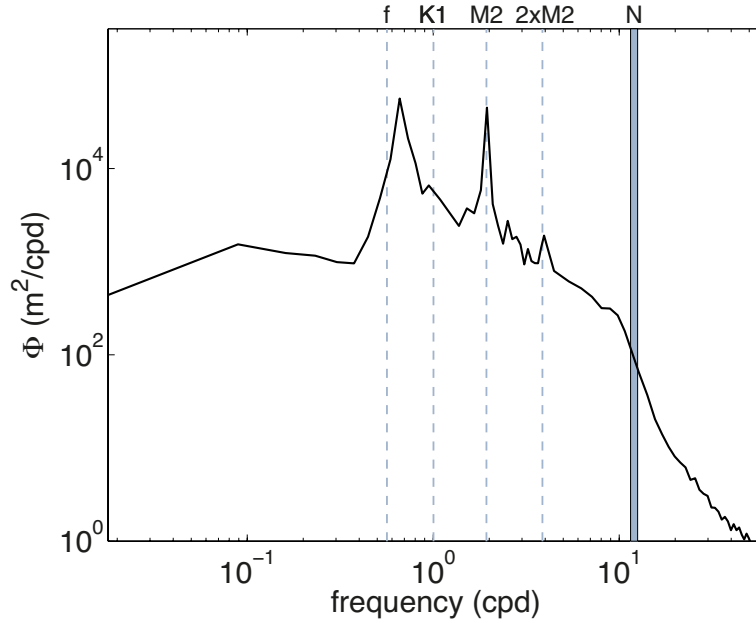


**Figure 2.3:** Mean spectra of vertical displacements measured in an approximate depth of 3200 m at the MOVE mooring in the center of western Atlantic basin during the fourth deployment period. Due the mooring location in the open ocean a typical open-ocean internal wave spectrum with sharp drop offs below the inertial frequency  $f$  and above the buoyancy frequency  $N$  is obtained. Additionally main tidal constituents are denoted by vertical dashed lines.

relation for internal waves is found to be

$$\omega_0^2 = \frac{N^2 k^2 + f^2 m^2}{k^2 m^2} = N^2 \cos^2 \Theta + f^2 \sin^2 \theta \quad (2.1)$$

where  $\omega_0$  is the internal wave frequency,  $k$  the horizontal and  $m$  the vertical wavenumber. The local inertial frequency is denoted by  $f = 2\Omega \sin(\phi)$  and  $N$  is the buoyancy frequency  $N^2 = g\rho^{-1}\partial\rho/\partial z$ . The permissible frequency range for free internal waves therefore is given by  $f \leq \omega \leq N$  (Fig. 2.3). Furthermore it follows from the dispersion relation that the angle to the horizontal  $\Theta$  under which internal waves propagate only depends on their frequency; particle motion is circular and almost horizontal at frequencies slightly higher than  $f$  in combination with an almost vertical wavenumber vector and gets increasingly more vertical in combination with an almost horizontal wavenumber vector when approaching the

upper frequency limit  $N$  (Fig. 2.2). A further consequence of this permissible frequency range also is that low frequency, near inertial waves can only propagate equatorwards (Fig. 1.5) since poleward propagating waves are reflected at the critical latitude where their frequency equals the local inertial frequency.

The group velocity  $\vec{c}_g$  of internal waves is perpendicular to the propagation direction of the wavenumber vector  $\vec{k}$  and is given by

$$\vec{c}_g = \left( \frac{\partial \omega_0}{\partial k}, \frac{\partial \omega_0}{\partial m} \right) = \left( \frac{km}{\omega_0} \frac{N^2 - f^2}{(k^2 + m^2)^2} m, \frac{km}{\omega_0} \frac{N^2 - f^2}{(k^2 + m^2)^2} k \right) \quad (2.2)$$

Internal waves propagating in regions with strong mean currents  $\vec{u}$  can be subject to Doppler shifting which changes the internal wave frequency such that the intrinsic frequency  $\omega_0$  is given by

$$\omega_0 = \omega - \vec{u} \cdot \vec{k}. \quad (2.3)$$

Furthermore relative vorticity  $\zeta$  shifts the low frequency limit of internal waves (Kunze, 1985), thus internal waves with effective frequencies  $f_{\text{eff}}$  below the inertial frequency can be observed in regions of negative relative vorticity:

$$f_{\text{eff}} = f + \zeta/2 \quad (2.4)$$

### 2.1.1 Critical topographic slopes

The propagation characteristics of internal waves given by the dispersion relation (Equ. 2.1) has important implications for the reflection of internal waves at topography sloping at an angle  $\alpha$ . While being reflected from these boundaries, the internal waves will preserve their frequency and hence their propagation direction relative to the horizontal (angle  $\Theta$ , Fig. 2.4). Therefore incident waves with propagation angles  $\Theta$  are reflected offshore for  $\alpha > \Theta$  and shoreward for  $\alpha < \Theta$  (Fig. 2.4). This has important consequences e.g. for the focusing of internal wave energy as it can be accumulated in small areas due to the topographic settings. A special role for the generation and dissipation of internal waves plays topography with the so called "critical angle" to the horizontal. Here the sloping angle of the local bottom topography  $\alpha$  equals the propagation angle  $\Theta$  of incident internal waves.

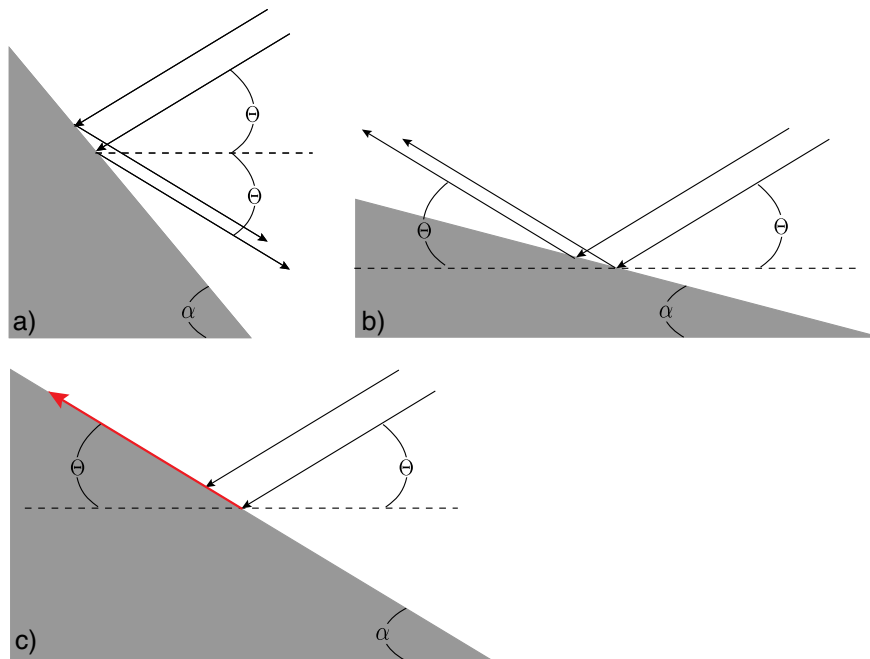


**Figure 2.4:** Internal waves incident on topography: panel a) shows internal waves impinging on a slope with supercritical angle  $\alpha$ , panel b) a subcritical slope and panel c) a slope with a critical angle for the impinging wave.

These waves have to be dissipated at the topography since the angle under which they would be reflected from the slope equals the sloping angle of the topography (Fig. 2.4). On the other hand this topography can also generate internal waves with the frequency that corresponds to the critical angle (e.g. shown at the Fieberling Guyot by Eriksen, 1998). This generation mechanism is especially important if  $\alpha$  equals the propagation angle of internal waves with tidal frequencies as here the conversion of barotropic tides into internal (tidal) waves is particularly efficient.

### 2.1.2 Lee waves

The bottom topography does not only influence the internal wave field via reflections but can also generate lee waves when a geostrophic current is flowing over topography with specific characteristics. When a current with flow speed  $U$  is

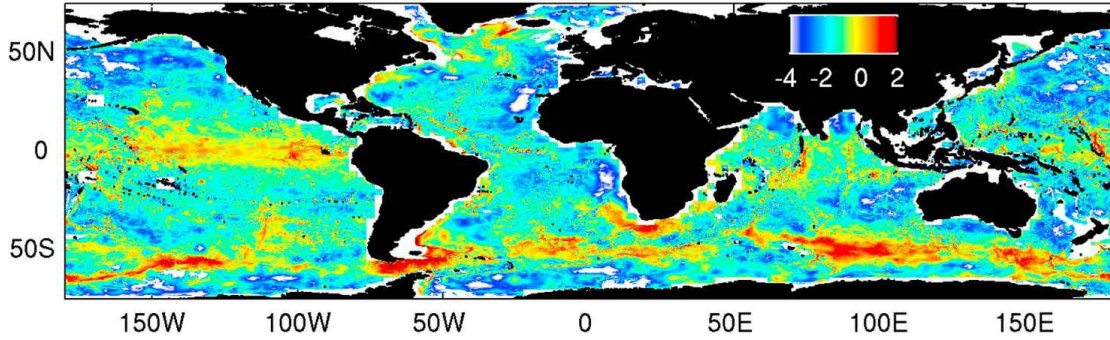


**Figure 2.5:** Global distribution of energy flux from geostrophic flows into lee waves in  $\log_{10}(\text{mW m}^{-2})$  using linear theory applied to bottom topography from single beam echo soundings, climatological bottom stratification and bottom velocity obtained from a global ocean model. From Nikurashin and Ferrari (2011).

flowing over a topography having a sinusoidal shape with wavenumber  $k$ , it generates lee waves with the frequency  $\omega = Uk$ . These waves can radiate upward from their topographic source if  $\omega$  lies between the inertial frequency  $f$  and the buoyancy frequency  $N$ . This is the limiting factor for topographic scales that can generate this type of waves as the topographic wavenumber has to fall into the range

$$N/U < k < |f|/U \quad (2.5)$$

Waves generated at such topographic features can provide a net upward energy transport as they have an upward group velocity  $c_g$  and therefore transport energy upward that can be dissipated higher up in the water column. Waves generated at topographic scales that do not fall in the range given in Equ. 2.5 are evanescent waves that are trapped at the ground and do not radiate energy.

Lee wave generation is strongest in the Southern Ocean and a global total energy of approximately 0.2 TW is contained in lee waves (Fig. 2.5, Nikurashin and Ferrari, 2011).

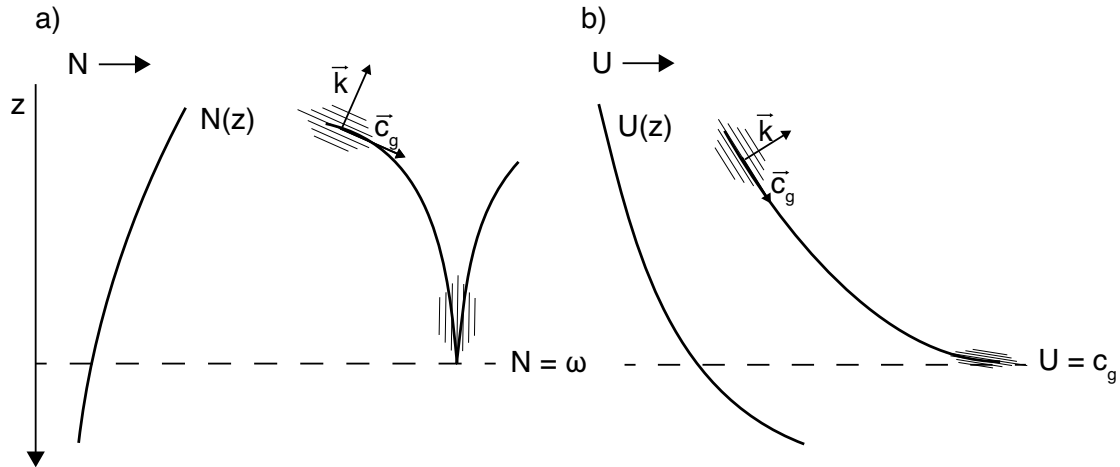


**Figure 2.6:** Critical layers occur at depths where the frequency of a propagating internal wave equals the local buoyancy frequency  $N$  (a) and at depths where the geostrophic mean velocity equals the group velocity  $c_g$  of the internal wave (b). Plot reproduced and modified from Munk (1981).

### 2.1.3 Critical layers

Another process which is very important for the propagation of internal waves is the response of internal waves to so called "critical layers". There are two types of critical layers: one where a propagating internal wave encounters a depth where its frequency equals the local buoyancy frequency  $N$  and the second where the group velocity  $c_g$  equals the velocity of the geostrophic mean current.

When an internal wave propagates into a layer where the local  $N$  equals its frequency, the vertical wave number and the group velocity approach zero and the wave is vertically reflected (Fig. 2.6a). This can lead to a trapping of internal waves in specific depth ranges when a local maximum occurs in the buoyancy frequency profile.

For the second form of a critical layer the effect of the geostrophic mean current on the local dispersion relation as given in Equ. 2.3 has to be taken into account. The intrinsic frequency  $\omega_0$  of an internal wave group propagating through a background with increasing background velocity  $U(z)$  will decrease as  $U$  increases and can eventually encounter a depth where  $\omega_0 = f$ . At this depth the vertical wavenumber approaches infinity and the group velocity tends toward the horizontal (Fig. 2.6b).

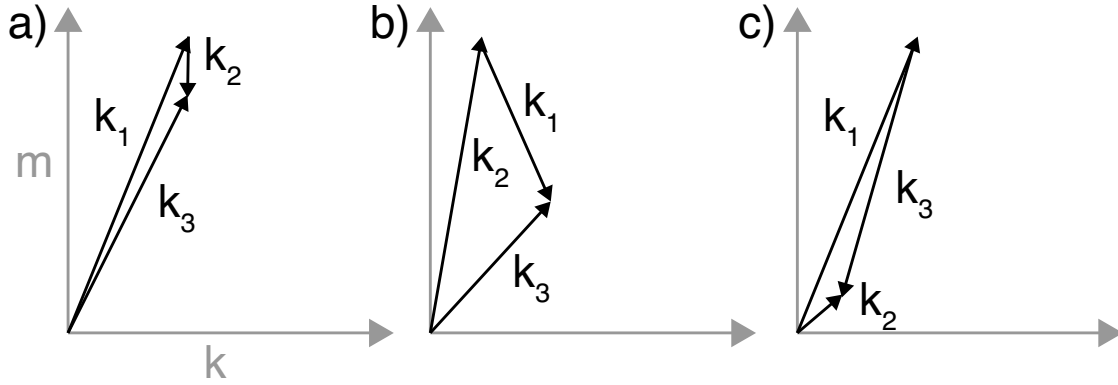


**Figure 2.7:** Wave-wave interaction processes involving three waves: a) induced diffusion, b) elastic scattering and c) parametric subharmonic instability. The aspect ratio  $m/k$  corresponds to a fixed frequency  $\omega$  following the dispersion relation given in Equ. 2.1. Plot reproduced and modified from e.g. McComas and Bretherton (1977).

Different from the simple reflection at the critical N-layer the effect of the critical U(z)-layer depends on the background Richardson number and waves can either be enhanced or absorbed by the mean flow (Jones, 1968; Munk, 1981).

### 2.1.4 Resonant interactions

Interactions between a triad of internal waves can occur if their wavenumbers and frequencies obey to the conditions of resonant interactions:

$$\begin{aligned}\omega_1 &= \omega_2 \pm \omega_3 \\ \vec{k}_1 &= \vec{k}_2 \pm \vec{k}_3\end{aligned}\tag{2.6}$$

McComas and Bretherton (1977) found three distinct processes dominating the resonant interactions: the induced diffusion, elastic scattering and the parametric subharmonic instability (Fig. 2.7).

In the induced diffusion a high frequency/high wavenumber wave ( $\vec{k}_3$ , Fig. 2.7) interacts with a low frequency/low wavenumber wave ( $\vec{k}_2$ ). Thereby the high frequency/high wavenumber wave propagates through a shear field of scales much larger than the wave packet. This induces a diffusion of wave action (internal

wave energy/frequency) along constant horizontal wavenumbers  $k$  and towards increasing vertical wavenumbers  $m$  ( $\vec{k}_1$ ). In this processes the energy is not conserved but interacts with the frequency/low wavenumber wave.

In the elastic scattering a wave with high frequency is scattered at a low frequency, near inertial wave with approximately twice the vertical wavenumber ( $\vec{k}_2$ ) inducing a wave with almost opposite vertical wavenumber ( $\vec{k}_1 = -\vec{k}_3$ ). This results in an almost balanced vertical energy transport for all but near inertial frequencies which also implies that if an asymmetry in the vertical energy propagation in higher frequencies is observed, the source of these waves has to be in close proximity (McComas and Bretherton, 1977).

The third form of resonant interaction, the parametric subharmonic instability, transfers energy from a low wavenumber ( $\vec{k}_1$ ) wave with frequency  $f_1$  to two waves with higher wavenumbers and approximately half the frequency of  $f_1$  until the internal wave action is distributed almost equally among the three waves. This process therefore primarily generates near inertial frequency waves with high wavenumbers.

### 2.1.5 The Garrett-Munk model

Even though the exact shape and magnitude of the internal wave spectrum was shown to be influenced by local properties such as e.g. topography, wind, currents or the stratification, its overall shape was found to be quite universal away from immediate generation sites. This prompted Garrett and Munk to develop a semi-empirical model describing internal wave energy in the frequency as well as in the wavenumber domain. The so called Garrett-Munk (GM) spectrum was fitted to the existing data at that time and its first form proposed in Garrett and Munk (1972b) was slightly modified over time (Garrett and Munk, 1975; Cairns and Williams, 1976; Munk, 1981; Levine, 2002) to achieve better agreement with (new) observational results. The model was successfully tested against observational results from the Internal Wave EXperiment (IWEX) (Briscoe, 1975; Müller et al., 1978). This experiment was located in the Sargasso Sea where current

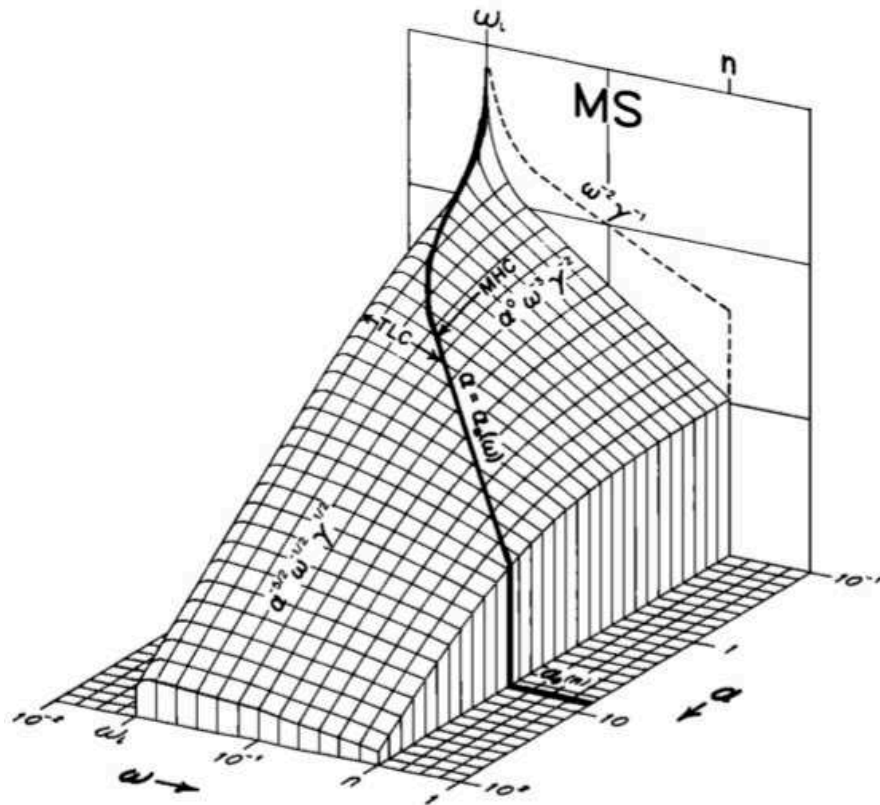


**Figure 2.8:** Garrett-Munk spectrum for internal wave energy at frequencies  $\omega$  and horizontal wavenumber  $\alpha$ . The integration  $MS(\omega) = \int E(\alpha, \omega) d\alpha$  yields the prediction of the internal wave spectrum measured by moored instruments. From Garrett and Munk (1975).

and temperature measurements were carried out with a three-dimensional moored tetrahedron array. This experimental setup allows the simultaneous measurement of internal waves in wavenumber and frequency spectra.

Major factors in the upkeep of the universal shape of the internal wave spectrum are the processes of resonant interactions between internal waves that were discussed above. They quickly (within few wave periods) redistribute internal wave energy within the spectrum thereby giving rise to the relatively smooth internal wave spectrum away from immediate internal wave sources.

The GM spectrum can be factorized into:

$$E(\alpha, \omega) = E_{\text{tot}} B(\omega) A(\alpha, \omega) \quad (2.7)$$

with the horizontal wave number  $\alpha$ , the wave frequency  $\omega$  and the total local energy  $E_{\text{tot}}$ . As the GM model assumes horizontal isotropy, different representation of the energy spectrum are related by:

$$\begin{aligned} \int \int \int E(\alpha_1, \alpha_2, \beta) d\alpha_a d\alpha_2 d\beta &= \int \int E(\alpha, \beta) d\alpha d\beta = \int \int E(\alpha, \omega) d\alpha d\omega \\ &= \int \int E(\beta, \omega) d\beta d\omega = E \end{aligned} \quad (2.8)$$

with  $E$  being a dimensionless constant related to the energy per unit area and  $\beta$  representing the vertical wavenumber. Consequently the GM spectra for moored measurements  $MS_\xi$  (of vertical displacements  $\xi$ ) can be obtained by

$$MS_\xi = \int Z^2(\omega) E(\alpha, \omega) d\alpha \quad (2.9)$$

as with moored observations contributions from different wavenumbers but equal frequencies can not be distinguished. The GM spectra for horizontal wavenumber  $\alpha$  and frequency  $\omega$  can be seen in Fig. 2.8 and shows the characteristic fall off below the inertial frequency  $f$  and the local buoyancy frequency  $N$ .

## 2.2 Turbulence and vertical mixing

When internal waves eventually break, they generate turbulent motion. This turbulence results in an irreversible loss of kinetic energy and in a vertical transport (flux) of e.g. heat, salt and nutrients.

In order to analyze the effect of turbulence in the ocean, motions are often sepa-

rated in mean and fluctuating parts (Reynolds decomposition):

$$\begin{aligned}\tilde{T} &= \bar{T} + T' & (\tilde{S} &= \bar{S} + S', \tilde{\rho} = \bar{\rho} + \rho') \\ \tilde{u}_i &= U_i + u_i \\ \tilde{p} &= P + p\end{aligned}\tag{2.10}$$

where properties denoted by tildes are instantaneous values of temperature ( $\tilde{T}$ ), salt ( $\tilde{S}$ ), density ( $\tilde{\rho}$ ), velocities ( $\tilde{u}_i$ ) and pressure ( $\tilde{p}$ ), capital letters or overbars respectively denote average values and fluctuations are indicated by small letters or primes. The definition of the fluctuating parts is such, that their mean is equal to zero.

If this decomposed properties are used in the equations of motion, the nonlinear term  $\tilde{u}_j (\partial \tilde{u}_i / \partial \tilde{x}_i)$  induces an additional stress  $\tau = -\rho_0 \overline{u_i u_j}$  where  $\rho_0$  is the background density. The so called Reynold stress tensor represents an additional stress acting on the mean flow due to turbulent motions. The Reynolds stress is a symmetric tensor whose off diagonal elements vanish for isotropic turbulence and it tends to decrease gradients in the mean flow as it transports e.g. momentum across diapycnals.

The x-z component of the Reynolds stress is related to the mean vertical velocity gradient via the eddy viscosity  $K_v$ :

$$\tau \approx -\rho \overline{uw} = \rho K_v dU/dz\tag{2.11}$$

where  $u$  denotes horizontal and  $w$  the vertical velocity.

Analog to this vertical transport of momentum eddy diffusivities can be obtained for other properties so that e.g. the vertical heat flux can be formulated in terms of an eddy diffusivity of temperature  $K_T$ :

$$F = \langle \rho c_p w T' \rangle = -\rho c_p K_T dT/dz\tag{2.12}$$

where  $c_P$  is the specific heat capacity of the water. The vertical transport of density can be obtained from:

$$F = \langle w \rho' \rangle = -K_\rho d\rho/dz\tag{2.13}$$

with the eddy diffusivity of density  $K_\rho$ .

The effect of turbulent motions on the kinetic energy budget of the mean flow can be evaluated using again the Reynolds decomposition into mean and fluctuating properties along with the resulting Reynolds stress in the equations of motion (Navier stokes equations). Multiplication of the equation of motion for the mean flow by  $U_i$  yields the mean kinetic energy. Following the notation of Kundu and Cohen (2008) it is given by

$$\begin{aligned} \frac{D}{Dt} \left( \frac{1}{2} U_i^2 \right) = & \frac{\partial}{\partial x_j} \left( \underbrace{-\frac{P U_j}{\rho_0} + 2\nu U_i E_{ij} - \overline{u_i u_j} U_i}_{\text{transport}} \right) \\ & - \underbrace{2\nu E_{ij} E_{ij}}_{\text{viscous dissipation}} + \underbrace{\overline{u_i u_j} \frac{\partial U_i}{\partial x_j}}_{\text{loss to turbulence}} - \underbrace{\frac{g}{\rho_0} \overline{\rho} U_3}_{\text{loss to potential energy}} \end{aligned} \quad (2.14)$$

where  $E_{ij}$  is the mean strain rate

$$E_{ij} = \frac{1}{2} \left( \frac{\partial U_i}{\partial x_j} + \frac{\partial U_j}{\partial x_i} \right) \quad (2.15)$$

and  $\nu$  the viscosity of seawater. The first terms in equation 2.14 describe the transport of kinetic energy by the mean pressure, by viscous stresses and by Reynold stresses.

An expression for the budget of the kinetic energy of the turbulent flow can be obtained by subtracting the equation of motion for the mean flow from the total flow, thus only the kinetic energy of the turbulence remains:

$$\begin{aligned} \frac{D}{Dt} \left( \overline{\frac{1}{2} u_i^2} \right) = & - \frac{\partial}{\partial x_j} \left( \underbrace{\frac{1}{\rho_0} \overline{p u_j} + \frac{1}{2} \overline{u_i^2 u_j} - 2\nu \overline{u_i e_{ij}}}_{\text{transport}} \right) \\ & \underbrace{- \overline{u_i u_j} \frac{\partial U_i}{\partial x_j}}_{\text{shear production}} + \underbrace{g \alpha \overline{w T'}}_{\text{buoyant production}} - \underbrace{s \nu \overline{e_{ij} e_{ij}}}_{\epsilon = \text{viscous dissipation}} \end{aligned} \quad (2.16)$$

where  $e_{ij}$  is rate of the fluctuating strain:

$$e_{ij} = \frac{1}{2} \left( \frac{\partial u_i}{\partial x_j} + \frac{\partial u_j}{\partial x_i} \right) \quad (2.17)$$

The kinetic energy lost by the mean kinetic energy to the turbulence production term is now part of the kinetic energy of the turbulence whereas the buoyant production term can either be a source or sink of turbulent kinetic energy depending on the stratification. Unlike for the kinetic energy of the mean flow, the viscous dissipation term  $\epsilon$  in the kinetic energy of the turbulence is of the same order of magnitude as the shear and buoyant production terms and always is a sink for turbulent energy. It is related to the eddy coefficient  $K_\rho$  discussed above by

$$K_\rho = \frac{R_f}{1 - R_f} \frac{\epsilon}{N^2} = \frac{\Gamma \epsilon}{N^2} \quad (2.18)$$

where  $\epsilon$  is the viscous dissipation.  $\Gamma$  is the mixing efficiency factor and a function of the flux Reynolds number  $R_f$

$$R_f = \frac{\overline{gw\rho'}\rho_0}{-\overline{uw}dU/dz} \quad (2.19)$$

that gives the ratio at which buoyancy forces reduce the mean kinetic energy for the production of turbulent kinetic energy by eddy stress on the mean shear. It exists an upper boundary above which turbulence is suppressed, a theoretical prediction of  $R_f = 0.15$  was given by Ellison (1957), hence Osborn (1980) proposed an upper boundary of  $\Gamma \leq 0.2$ . Even though  $\Gamma$  was shown to be somewhat variable a value of 0.2 is now widely used.

The scale at which finally viscous dissipation takes place is given by the Kolmogorov microscale

$$\eta = \left( \frac{\nu^3}{\epsilon} \right)^{1/4} \quad (2.20)$$

The energy spectrum for wavenumbers  $k \ll l^{-1}$  with  $l$  denoting the size of the energy containing eddies can be represented by an isotropic frequency spectrum given by

$$E(k) = \alpha \epsilon^{2/3} k^{-5/3} \quad (2.21)$$

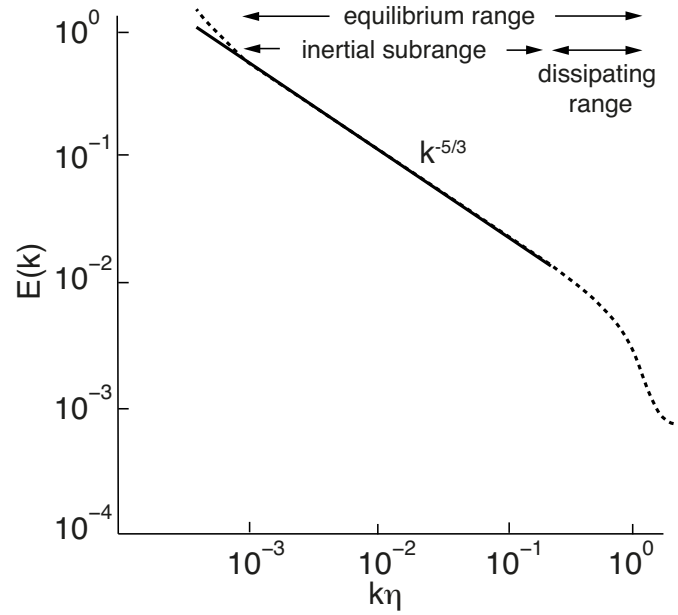


**Figure 2.9:** Energy-wavenumber spectrum with dashed line denoting theoretical data. Reproduced and modified from Kundu and Cohen (2008)

with the constant  $\alpha \approx 0.5$  (Tennekes and Lumley, 1972), Fig. 2.9. The upper wavenumber limit for this spectrum is equal to  $k \sim \eta^{-1}$  as dissipation occurs at smaller scales leading to a fall off in the spectrum for higher  $k$ . The wavenumber range  $l^{-1} \ll k \ll \eta^{-1}$  is called the inertial subrange. Even though energy is not dissipated in the inertial subrange, energy has to be transferred through the spectrum in dependence on the magnitude of  $\epsilon$  in order to maintain an equilibrium state. Furthermore Kolmogorov argued, that the equilibrium range is independent of the viscosity. The spectral dependence in  $\epsilon$  and  $k$  was subsequently deduced by Kolmogorov based on dimensional grounds. For wavenumbers above the Kolmogorov scale  $\eta$  dissipation sets in and a sharp drop off occurs in the spectrum.



### 3 | Oceanographic setting and the mooring array

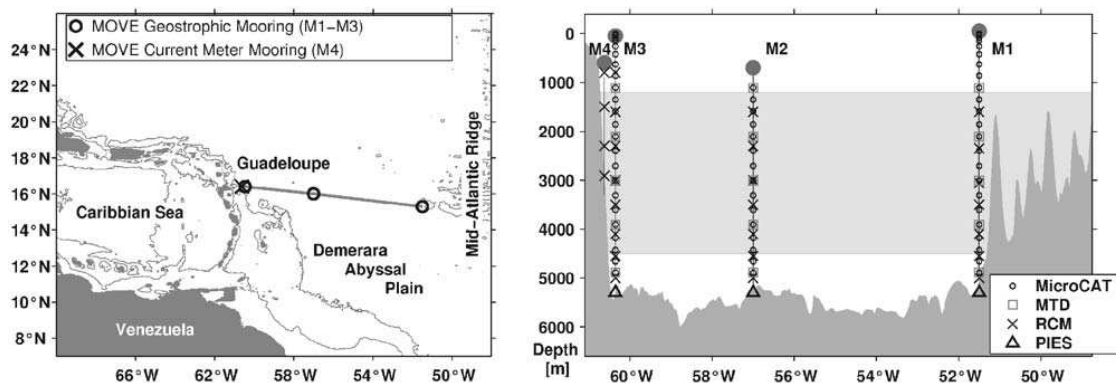


**Figure 3.1:** The MOVE array is located between the Lesser Antilles and the Mid Atlantic Ridge at about 16°N (left). From 2000 – 2005 it continuously consisted of three geostrophic and one current meter mooring to measure the flow over the continental slope (right). Its main purpose is to measure the transport of North Atlantic Deep Water (NADW) which is approximately located in the depth range denoted by the gray shading. From Kanzow et al. (2006)

Along with five hydrographic sections spanning the western tropical Atlantic at 16°N this study is based on data obtained by two moorings at the westernmost end of a mooring array deployed in the framework of the Meridional Overturning Variability Experiment (MOVE) (Fig. 3.1, Kanzow et al., 2006, 2008; Rhein et al., 2004, 2005; Send et al., 2011). The MOVE array was installed in 2000 and is in continuous operation since then. It spans the west Atlantic basin at 16°N from the Lesser Antilles to the Mid Atlantic Ridge (MAR). The primary objective of this mooring array is to obtain measurements of transport fluctuations of the meridional transport of the North Atlantic Deep Water (NADW, Kanzow et al., 2006, 2008).

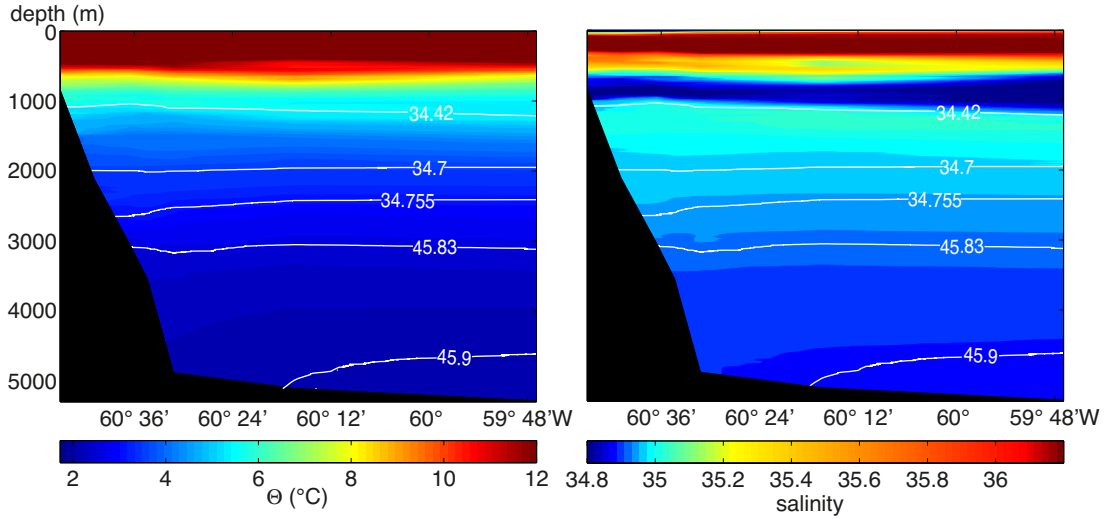


**Figure 3.2:** Exemplary sections of potential temperature (left) and salinity (right) along  $16^{\circ}\text{N}$  obtained during M53/3. The main temperature/salinity characteristics do not significantly depend on the strength of the DWBC. Density interfaces between watermasses forming the NADW, which is transported southward by the DWBC, are depicted by white isopycnals (density intervals from Rhein et al., 2004). In the density range  $34.42 < \sigma_{1.5} < 34.70$  the upper Labrador Seawater (uLSW) is found followed by the classical Labrador Seawater (cLSW  $34.70 < \sigma_{1.5} < 34.755$ ). Between  $\sigma_{1.5} = 34.755$  and  $\sigma_4 = 45.83$  the middle North Atlantic Deep Water (mNADW) is located, between  $\sigma_4 = 45.83$  and  $\sigma_4 = 45.90$  the Denmark Strait Overflow Water (DSOW). The deepest watermass ( $\sigma_4 > 45.90$ ) below the NADW is the Antarctic Bottom Water (AABW) (Rhein et al., 2004). The salinity minimum slightly above 1000 m is induced by Antarctic Intermediate Water (AAIW), the higher salinity below by water from the Mediterranean Sea.

The NADW is transported southward in the Deep Western Boundary Current (DWBC) which is the cold southward return flow of the Atlantic Meridional Overturning Circulation (AMOC). The NADW is localized at depths between approximately 1200 m and 4000 m (Rhein et al., 1995) and consists of several watermasses which are subsumed as NADW at  $16^{\circ}\text{N}$ : the upper Labrador Sea Water (uLSW), the classical Labrador Sea Water (cLSW) the middle NADW (mNADW) and the Denmark Strait Overflow Water (DSOW) (Rhein et al., 2004).

In addition to the watermasses forming the NADW, the surface water at the location of the westernmost moorings of the MOVE array is a mixture of water coming from the South Atlantic (Schott et al., 1998) and water discharged by the Amazon (Hellweger and Gordon, 2002).

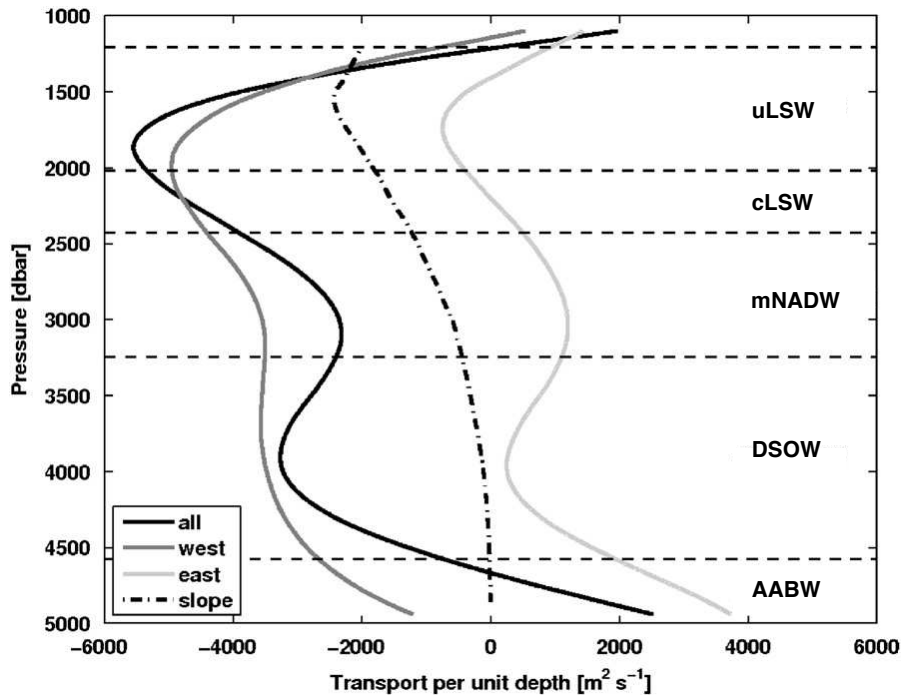


**Figure 3.3:** Mean geostrophic transport (February 2000 – May 2005) per unit depth between the three geostrophic moorings of the MOVE array and over the continental slope obtained from the current meter mooring. Different water mass boundaries are denoted on the right and roughly correspond to the definitions given in Rhein et al. (2004). Modified from Kanzow et al. (2008).

A layer of high salinities is found below the surface (Fig. 3.2); here the Salinity Maximum Water (SMW) which is formed by subduction of water north and south of the equator (Schott et al., 1998) is located.

At a depth of approximately 1000 m a salinity minimum layer is induced by the Antarctic Intermediate Water (AAIW) whereas warm and salty Mediterranean Water which is transported westward causes an elevated salinity at a depth of approximately 1200 m in the density layer of the uLSW at the mooring location. Below the NADW the Antarctic Bottom Water (AABW) is found, which is the densest water found in the Atlantic and subsumes several watermasses that are formed around Antarctica.

The position of the MOVE array fulfills several constraints in order to establish a reliable transport measurement (Kanzow et al., 2006): the continental slope on the

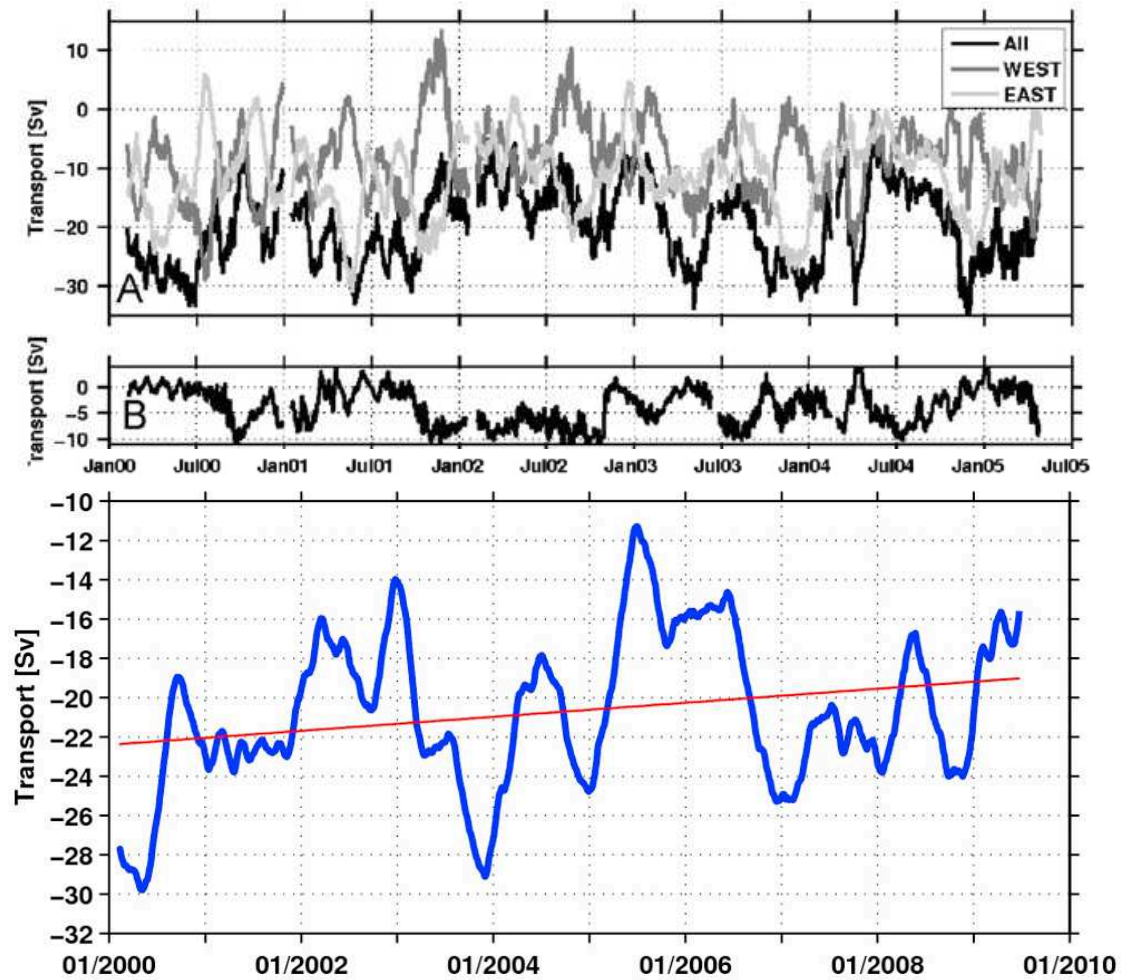


**Figure 3.4:** top: Internal transports (zonally integrated meridional geostrophic transports relative to the reference pressure of 4950 dbar) between the three geostrophic moorings M1 - M2 (west), M2 - M3 (east) between 1180 dbar and 4950 dbar relative to 4950 dbar. center: Transport over the continental slope west of the M3 mooring below 1180 dbar obtained from current meter measurements. bottom: 120-day low-pass filtered time-series of volume transport across the MOVE array in the NADW layer. Top and center panel from Kanzow et al. (2008), bottom panel from Send et al. (2011).

western end of the mooring array is very steep allowing for a transport calculation with a minimum of additional current meter moorings on the continental slope, all moorings are located on approximately the same latitude and the topography between the end points is not shallower than the bottom depths at the two end point moorings. This allows the calculation of transport timeseries using geostrophy. Furthermore the seasonal variability at this latitude is smaller than further

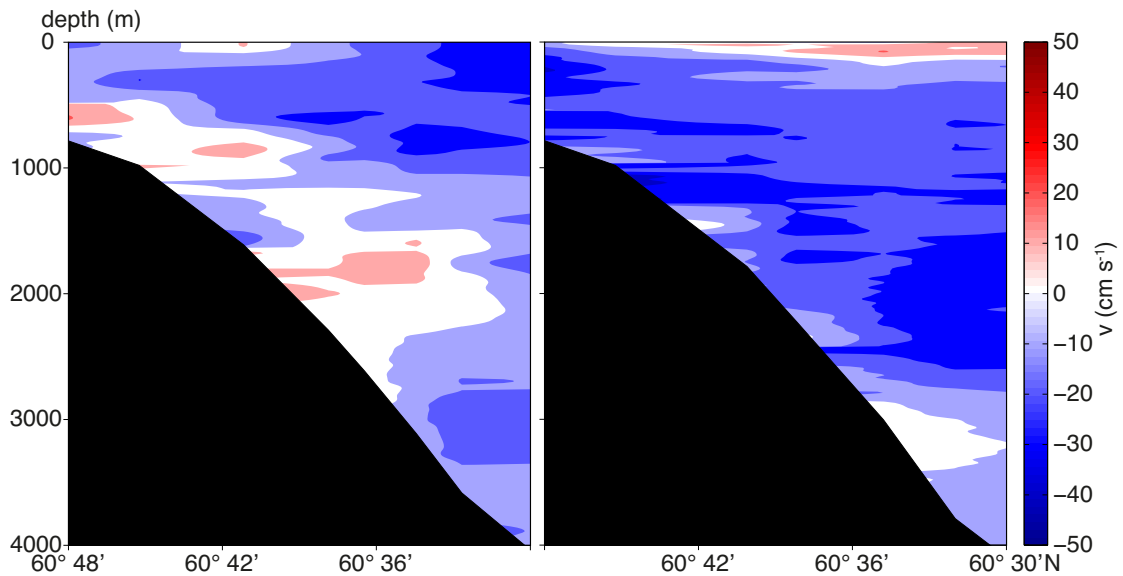


**Figure 3.5:** Sections of meridional velocities obtained during cruises Sonne 171 in June 2003 (left) and Meteor 62/1 in July 2004 (right).

south, yet at this latitude the majority of southward flowing water is found in the western basin whereas further north a significant amount is found in the eastern basin (Kanzow et al., 2006).

In this study data from 2000 to 2005 are being used. During this timespan three geostrophic moorings and one additional current meter mooring (Fig. 3.1), deployed to estimate the flow over the continental slope, in combination with bottom pressure measurements were continuously used to obtain transport timeseries. Both moorings are directly located in the flow path of the DWBC that is a confined jet of less than 100 km width at this latitude (Kanzow et al., 2006). Shipboard measurements showed that it carried between 25.6 – 28.9 Sv southward in 2000, 2002 and 2003 at 16° N (Rhein et al., 2004). However the strength and position of the DWBC is highly variable resulting in pronounced differences in the observed flow structure directly over the continental slope (Fig. 3.5). During some periods (e.g. during the Sonne 171 cruise during June 2003) the flow directly over the continental slope is weak whereas it was very strong in July 2004 during the Meteor 62/1 cruise.

Using the mooring data from the entire MOVE array Kanzow et al. (2008) de-

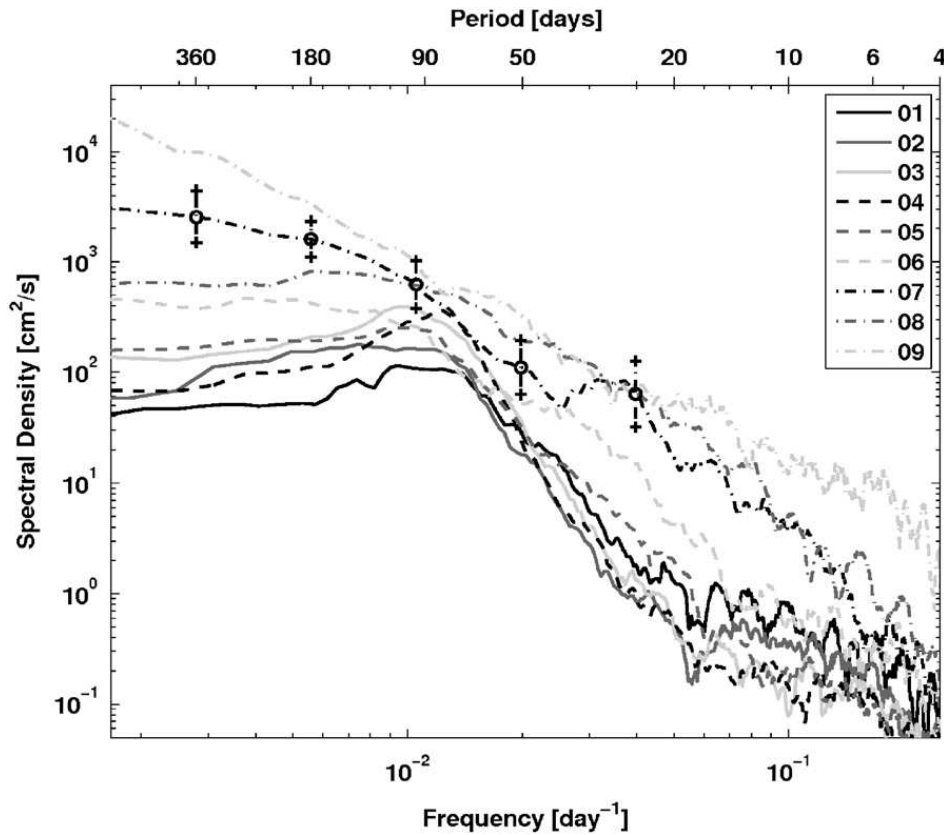


**Figure 3.6:** Long-term variability of meridional velocity averages between 1600 m and 3000 m obtained from the 9 moorings that were deployed in the framework of MOVE and GAGE (Guyana Abyssal Gyre Experiment). Sites 1, 6 and 9 correspond to MOVE moorings M1, M2 and M3 (Fig. 3.1), 95% confidence intervals are denoted by vertical lines. From Kanzow et al. (2008).

terminated  $-15.9 \text{ Sv}$  as the total mean transport of NADW in the western Atlantic basin between 2000 – 2005 (Fig 3.3). This mean southward transport is far from continuous as very high temporal variability of up to  $40 \text{ Sv}$  within one month within the entire MOVE section (Kanzow et al., 2008) was observed (Fig. 3.4).

In almost 10 years of continuous NADW transport measurements within the MOVE section a decrease of approximately  $0.3 \text{ Sv}$  per year is found with a statistical significance of 85% (Send et al., 2011) and if a constant depth of the level of no motion is assumed. This trend is supposed to be part of the natural multi-decadal transport fluctuations.

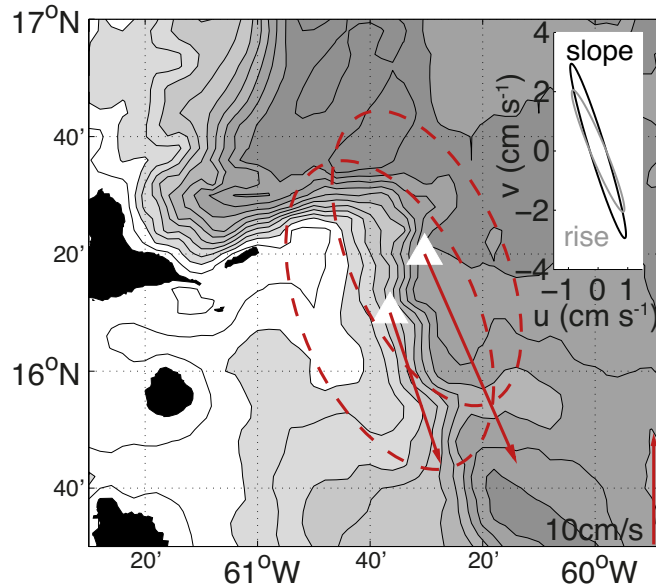


**Figure 3.7:** Mean meridional and zonal velocities (2000 – 2005) at both moorings along with ellipses denoting the standard deviation in the five years in the rotated velocities at a depth of approximately 1500 m (red). M2 tidal ellipses for moorings at the continental slope and rise at approximately 1500 m (maximum of the DWBC) are shown in the inset. Topography in the background is from the ETOPO2 database (Etopo2, 2001).

Long term variability in mean meridional velocities between 1600 m and 3000 m at the easternmost (MAR) MOVE mooring shows a peak at approximately 80 – 120 days probably induced by westward propagating Rossby waves (Kanzow et al., 2008, Fig. 3.6). Moving further west, the spectral energy level increases and the 80 – 120 days peak is less pronounced at the central MOVE mooring and is no longer found at the mooring in the DWBC. Here additional features like North Brasil Current rings additionally influence the long-term current variability (Kanzow et al., 2008).

Velocities measured at the westernmost moorings within the DWBC vary considerably over time (Fig. 4.2) and reach peak values of up to  $50 \text{ cm s}^{-1}$  in the core of the DWBC (approx. 1500 m – 2500 m). Velocities decrease towards the sea floor down to values close to zero. The flow direction reverses to a weak northward flow during four periods in the five years (early 2000, mid 2001, November 2002 and April 2003) during which the DWBC might shift eastward (Kanzow et al., 2006).

The mean flow as well as the ellipse of the dominant M2 tidal constituent in the core of the DWBC are following the bathymetry in a southeastward direction at both moorings (Fig. 3.7).

## 4 | Data

### 4.1 Timeseries data

Next to the DWBC transport calculations, the MOVE timeseries also provides an excellent data base to study the long term variability of the internal wave field due to the large number of sensors and the small sampling intervals.

This study focuses on data from one mooring location on the continental rise and a second mooring location on the continental slope (Fig. 4.1). Information on the deployment periods, location, instrumentation and sampling intervals for the various moorings that occupied these sites during the mooring deployments are provided in Tables 4.1 and 4.2 respectively. Data were used from five mooring deployment periods covering the time from 2000 to 2005. The mooring on the continental rise was equipped with 15 to 22 Sea-Bird temperature/conductivity recorders (SBE 37 MicroCAT) with a sampling interval of 5 to 20 min and 5 to 8 RCM8 Aanderaa current meters with a sampling interval of 120 min. During the first two deployment periods, the topmost instrument was at a depth of 1200 m and 600 m respectively. From the third deployment period onward instrumentation was extended to the surface. The vertical spacing between the instruments was 200 m at the top of the mooring, 330 m at mid-depth and decreasing towards the bottom to 200 m.

Data calibration, quality control and depths assignment for the MOVE data set were carried out by Torsten Kanzow (see Kanzow et al., 2006, 2008) and are shortly summarized below.

Temperature and conductivity measurements were calibrated against a Sea-Bird CTD probe prior and after each deployment and a linear drift correction was applied. This yields a temperature accuracy of  $0.002^{\circ}\text{C}$  and an accuracy of  $0.002\text{ m S cm}^{-1}$  for conductivity.

Pressure was measured with a temporal resolution of 20 min – 60 min by up to five custom build miniature temperature and pressure loggers (MTD) which were

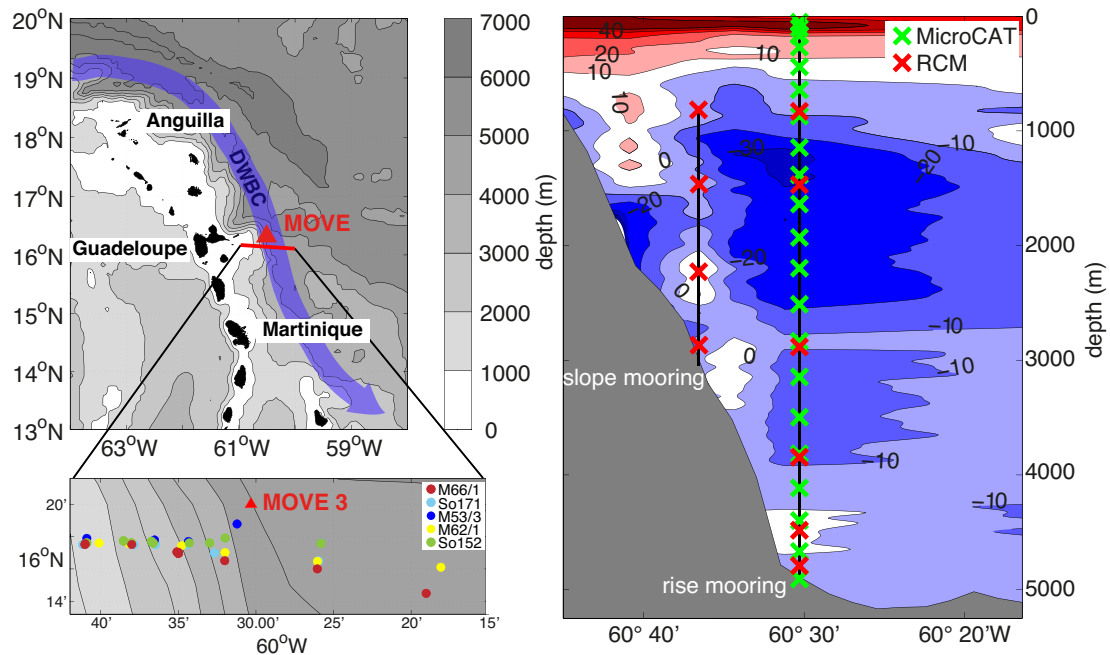


**Figure 4.1:** Two moorings of the MOVE array were deployed in the pathway of the DWBC and equipped with the instrumentation exemplarily shown for the 4th deployment period (2003 - 2004, right). Contours show a strong DWBC with meridional velocities of up to  $50 \text{ cm s}^{-1}$  determined from LADCP measurements during the Meteor 53/3 cruise in June 2002. Positions of CTD/LADCP measurements are denoted by the dots in the detailed map at the bottom left.

attached to the mooring close to the MicroCATs. Additionally, pressure was measured by one of the upper MicroCATs from the 3rd deployment period onward. Accuracy of both instrument types is approximately 0.1% (0.5 dB).

MicroCAT depths were determined for 2 h intervals for all MicroCats that were not deployed close to an MTD either by linear interpolation or using a mooring curvature model during times when the mooring was heavily knocked down. Thereby a depth assignment with an accuracy of  $\pm 3 \text{ m}$  is achieved.

Data records are continuous except for a small gap of approximately two and a half months at the end of 2001 due to a loss of buoyancy elements in the upper part of the mooring, including the upper part of the depth range of the DWBC (Fig. 4.2). As the main focus of this study is on variability in the internal wave field in the DWBC, all data measured during this time span were not used. Additionally, one MicroCAT (nominal depth 3900 m) of the first deployment did not provide good

quality data for a period of approximately two months, therefore data from this instrument were not used. Data from the topmost MicroCAT of the third deployment were not used because no accurate pressure could be assigned.

The mooring located on the continental slope is used to supplement the analysis of internal wave velocity spectra as it was continuously equipped with four RCMs at depths between 800 m and 2900 m during the full time period from 2000 to 2005. Data are continuous except for few gaps (Fig. 4.2) during the third and fourth deployment period.

deployment period	location	topmost instrument	# of $\mu$ CATs	sampling interval	# of RCMs	sampling interval
02/04/00 - 12/30/00	16° 20.0' N, 60° 30.2' W	1185 m	15	5 min	7	120 min
01/14/01 - 01/23/02	16° 20.4' N, 60° 30.3' W	586 m	18	10 min*	8	120 min
02/07/02 - 06/15/03	16° 20.4' N, 60° 30' W	18 m	22	10 min	5	120 min
06/27/03 - 02/18/04	16° 20.4' N, 60° 30' W	53 m	21	10 min	7	120 min
03/01/04 - 04/30/05	16° 20.0' N, 60° 31' W	31 m	21	15 min	5	120 min

\*uppermost 2 instruments just measured with a resolution of 20 min, data were interpolated to 10 min resolution to obtain a consistent temporal resolution.

**Table 4.1:** Geographic position, position of uppermost instrument, number of instruments and instruments sampling intervals of the moorings at the continental rise during the five deployment periods. Instrument distribution with depth is shown in Fig. 4.2.

deployment period	location	instrumentation range	# of RCMs	sampling interval
02/04/00 - 01/10/01	16° 20.0' N, 60° 36.2' W	1087 m - 2945 m	4	120 min
01/14/01 - 01/23/02	16° 20.4' N, 60° 36.5' W	1098 m - 2951 m	4	120 min
02/05/02 - 05/15/03	16° 20.0' N, 60° 36.4' W	771 m - 2930 m	4	120 min
06/27/03 - 02/17/04	16° 20.0' N, 60° 36.4' W	772 m - 2931 m	4	120 min
03/02/04 - 04/30/05	16° 20.0' N, 60° 36.4' W	824 m - 2919 m	4	120 min

**Table 4.2:** Geographic position, position of uppermost instrument, number of instruments and instruments sampling intervals of the moorings at the continental slope during the five deployment periods. Instrument distribution with depth is shown in Fig. 4.2.

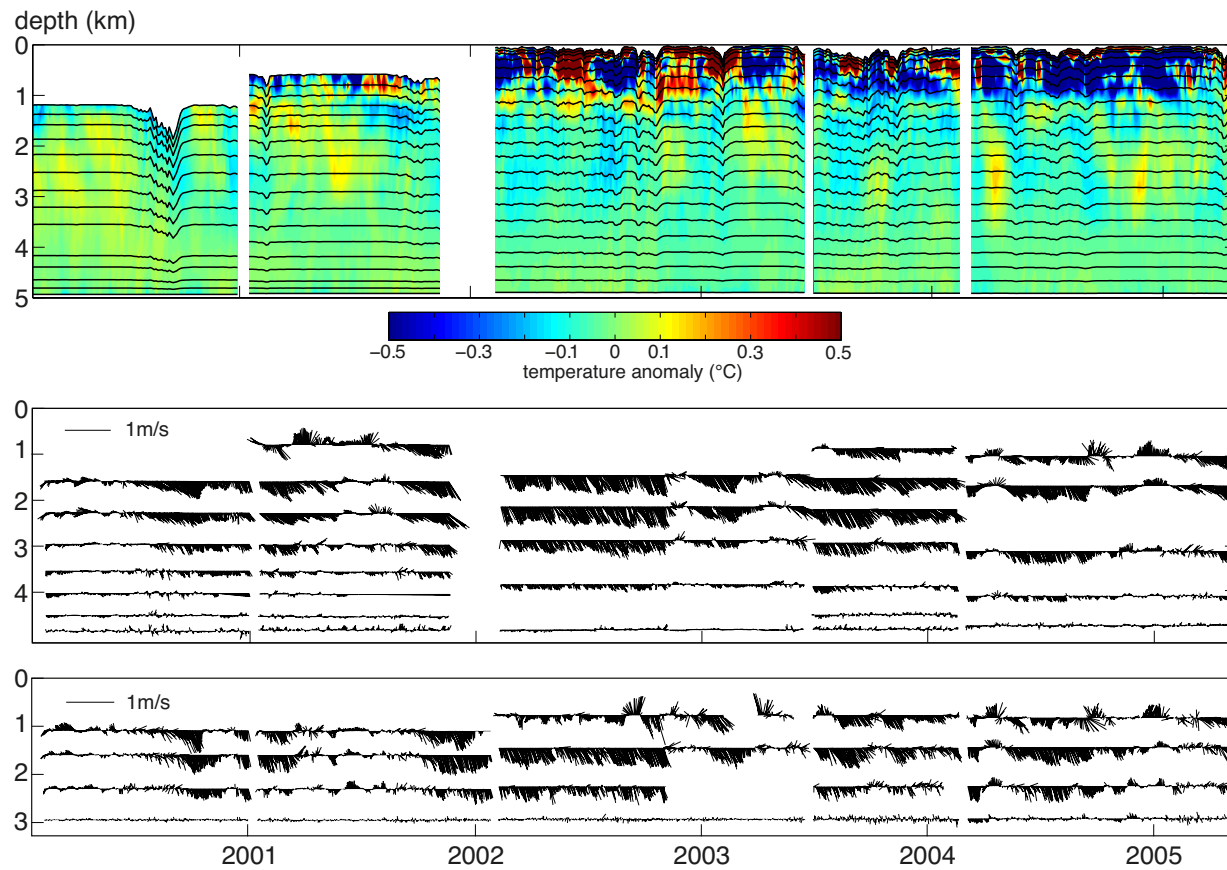


**Figure 4.2:** Top: Time series of 3-day mean temperature anomalies from mean temperature at the respective depths at the continental rise, black lines denote instrument depth. The data gap between second and third deployment period results from a breakage of the upper part of the mooring at the end of the second deployment period. Data measured by the remaining deeper instruments during this time were not used in the analyses. Center: RCM time series of horizontal velocities at the continental rise. Bottom: RCM time series of horizontal velocities at the continental slope.

## 4.2 Hydrographic data

LADCP and CTD stations were occupied close to the moorings along 16°N and provide data that were used to determine diapycnal diffusivities using a finescale parameterization. Measurements were carried out during five cruises between 2000 and 2005. The positions of the stations during each cruise are depicted in Fig. 4.1, LADCP configurations are given in Table 4.3.

The CTD probe used on all cruises was a SBE 911plus with an accuracy of 0.002 °C for temperature and of 0.002 - 0.003 for salinity. Velocities were measured either by two RDI 300 kHz Workhorse Monitor ADCPs or a customized RDI 150 kHz Narrowband ADCP (Rhein et al., 2004, 2005; Kirchner et al., 2008). Available velocity profiles were processed by an inverse method (Visbeck, 2002) with applied bottom track, barotropic and smoothness constraints. Bin length  $z_{\text{bin}}$  were set to 10 m (17.6 m) for the 300 KHz (150 KHz) instrument resulting in a nominal accuracy of 2 cm s<sup>-1</sup> (3.2 cm s<sup>-1</sup>) for the horizontal velocity of each individual bin.

Ship	Time period	number of stations	LADCP				DWBC present
			frequency	$z_{\text{bin}}$	$z_{\text{grid}}$	$d'$	
Sonne 152	Dec 2000	3	150 kHz	17.36 m	10 m	12.5 m	yes
Meteor 53/3	Jun 2002	4	150 kHz	17.36 m	10 m	12.5 m	yes
Sonne 171	Jun 2003	6	150 kHz	17.36 m	10 m	12.5 m	no
Meteor 62/1	Jul 2004	6	300 kHz	10 m	10 m	9 m	yes
Meteor 66/1	Aug/Sept 2005	14	300 kHz	10 m	10 m	9 m	no

**Table 4.3:** Cruise details and instrument specifications for LADCP data obtained off the Lesser Antilles along 16°N.

## 5 | Methodology

If strong currents, such as the DWBC, or their interaction with topography can lead to variability in the near inertial frequency range of the internal wave field, these currents could play an important role in generating internal waves and promoting vertical mixing. Should a downscale energy transfer from currents via internal waves (as proposed by e.g. Nikurashin and Ferrari, 2010b,a; Liang and Thurnherr, 2012) to vertical mixing occur throughout significant volumes of the world oceans, its influence on the internal wave field and global vertical mixing rates would need to be incorporated in future parameterizations of vertical mixing.

The extensive data set available for this study allows to address this issue with a high temporal resolution and over a long time span. Combined with the CTD/LADCP data the five year long time series allows to deduce significant correlations between DWBC strength and position and variability in the internal wave field and vertical mixing.

### 5.1 Finescale parametrization of diapycnal diffusivities

To investigate the influence of the high velocities within the DWBC on mixing rates, diapycnal diffusivities were calculated from CTD and LADCP data using a finescale parameterization based on shear  $\langle V_z^2 \rangle$  and strain variances  $\langle \xi_z^2 \rangle$  (Gregg et al., 2003). This is an indirect method to estimate diapycnal diffusivities  $K_\rho$  based on the theory of wave-wave interactions. In the finescale parameterization the spectral energy transport rate in the vertical wavenumber domain is used to infer mixing intensities. It provides a smoothed integral estimate of the mixing rate as it considers a signal at larger scales (intermediate internal waves) to infer diapycnal diffusivities by assuming that the spectral energy transport rate in the

vertical wavenumber domain equals the rate of turbulent production.

Gregg (1989) found that mean estimates of mixing intensities obtained from microstructure measurements agree to a factor of 2 with estimates obtained from the finestructure parameterization. A more recent study by Sheen et al. (2013) found a general overprediction of mixing rates obtained from the finescale parameterization compared to microstructure measurements by typically a factor of 2 and up to a factor of 8 in extreme cases. However the general pattern of the intensity of vertical mixing obtained from the finescale parameterization seems to be robust. The influence of the choice of the integration limits in the integration of our shear and strain variance spectra on the magnitude of the calculated  $K_\rho$  values is discussed at the end of this subsection.

The calculation of  $K_\rho$  closely follows the method described in Kunze et al. (2006) and diapycnal diffusivities were obtained from:

$$K_\rho = K_0 \frac{\langle V_z^2 \rangle^2}{GM \langle V_z^2 \rangle^2} h_1(R_\omega) j \left( \frac{f}{N} \right) \quad (5.1)$$

with buoyancy frequency  $N$ , inertial frequency  $f$ ,  $K_0 = 0.05 \times 10^{-4} \text{ m}^2 \text{ s}^{-1}$  and shear variance  $GM \langle V_z^2 \rangle^2$  as defined by the GM model spectrum in the same frequency range as  $\langle V_z^2 \rangle^2$ . Shear/strain variance ratio and latitudinal correction terms are given by

$$h_1(R_\omega) = \frac{3(R_\omega + 1)}{2\sqrt{2}R_\omega\sqrt{R_\omega - 1}}, \quad (5.2)$$

$$j(f/N) = \frac{f \operatorname{arccosh}(N/f)}{f_{30} \operatorname{arccosh}(N_0/f_{30})}, \quad (5.3)$$

with  $f_{30} = f(30^\circ)$  and  $N_0 = 5.2 \times 10^{-3} \text{ rad s}^{-1}$ . The shear/strain variance ratio  $R_\omega$  is defined as

$$R_\omega = \frac{\langle V_z^2 \rangle}{N^2 \langle \xi_z^2 \rangle}. \quad (5.4)$$

Using CTD and LADCP data from the same cruises analyzed here, Stöber et al. (2008) found a correlation between the velocities in the DWBC and diapycnal diffusivities. Here the integration limits (see discussion below) as well as the applied transfer function were modified compared to Stöber et al. (2008). In this study the most recent transfer function developed by Thurnherr (2012) for velocity profiles

calculated using the inverse method is applied. Nevertheless as Thurnherr (2012) finds only minor differences between the different transfer functions for wavelengths above 150 m the difference in  $K_\rho$  induced by the different transfer function is not crucial for the used integration range (wavelengths between 320 m and 110 m). Using this most recent transfer function the data used in Stöber et al. (2008) were reprocessed and grouped into the two flow situations of a strong and an absent DWBC over the continental slope in order to obtain a synoptic picture of the calculated mixing rates and the dominant wave frequencies via the shear to strain ratio  $R_\omega$  for the different flow strengths.

The transfer function by Thurnherr (2012) corrects for the attenuation in the shear spectra at high wavenumbers induced by the LADCP data processing and is given by:

$$S_{\text{correct}} = \frac{1}{\text{sinc}^4\left(\frac{z_{\text{bin}}}{\lambda_z}\right) \text{sinc}^4\left(\frac{z_{\text{grid}}}{\lambda_z}\right) \text{sinc}^2(d')} \quad (5.5)$$

where  $\lambda_z$  is the considered vertical wavelength,  $z_{\text{bin}}$  is the LADCP bin length,  $z_{\text{grid}}$  the vertical grid size and  $d'$  the range maxima. This correction accounts for range averaging, depth binning, pre-binning into super-ensembles before the inversion and instrument tilt. The cruise dependent parameters  $z_{\text{bin}}$ ,  $z_{\text{grid}}$  and  $d'$  are given in Table 4.3.

Resulting shear and strain spectra were grouped depending on flow situation to obtain regime average diffusivity profiles: three of the cruises (So152, M53/3 and M62/1) were carried out during times when a coherent southward flow was observed at several adjacent stations above the continental slope and two cruises (M66/1 and So171) where the flow is rather dominated by a mesoscale eddy structure (Rhein et al., 2004; Stöber et al., 2008). Thereby a synoptic picture of the intensity of vertical mixing and its spatial distribution could be obtained for both flow situations of a strong or an absent DWBC over the slope.

Vertical wavenumber spectra of shear and strain as well as corresponding estimates of the GM model (Gregg and Kunze, 1991) were calculated from all profiles and grouped according to the two different flow situations of a strong or an absent DWBC at the moorings. Furthermore spectra were binned with respect to meters above bottom (mab) and mean spectra in different depth ranges are shown in Fig. 5.1. All calculated mean shear and strain variance spectra are well above

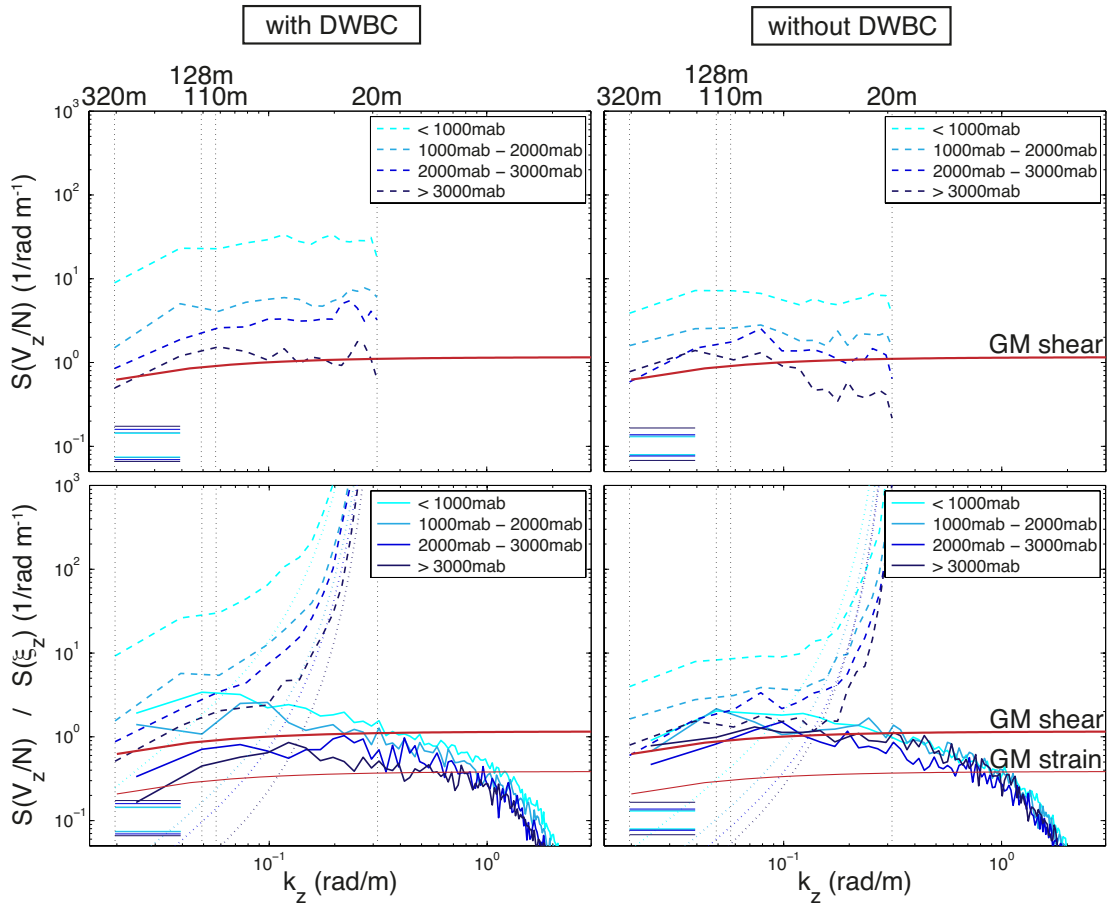


**Figure 5.1:** Top: Mean uncorrected shear vertical wavenumber spectra from all cruises grouped according to meters above bottom (mab) and divided into two groups: All cruises where the DWBC was found at the mooring location (So152, M53/3 and M62/1, left) and cruises during which there was no DWBC at this position (M66/1 and So171, right). Bottom: Mean shear (dashed lines) and strain (solid lines) vertical wavenumber spectra from all cruises grouped according to meters above bottom (mab) and divided into the two different flow situations. GM shear and strain spectral values are shown in red, estimates for noise in LADCP data are denoted by dotted lines. Noise levels were either determined by fitting the noise spectrum (Kunze et al., 2006) to shear spectral values at wavelengths shorter than 40 m or were set to a fixed noise level of  $3 \text{ cm s}^{-1}$  whichever is higher. Integration limits are denoted by vertical dotted lines and 95% confidence intervals are shown on the bottom left in each plot.

GM estimates except the uppermost strain variance spectra during phases when the DWBC was at the mooring. Overall, changes in magnitude of shear and strain variance spectra with depths are more pronounced during these times as both shear and strain variances increase significantly towards the bottom (Fig. 5.1).

Especially during phases of a strong DWBC uncorrected shear variance does not show the decrease at higher wavenumbers (induced by the LADCP data processing, top panel in Fig. 5.1) which is commonly observed and which is also found in spectra obtained from data measured during weak flows at depths more than 2000 m above the bottom. This leads to blue spectra especially during phases of strong flows (lower left panel of Fig. 5.1) after the correction term accounting for attenuations in the high wavenumber range due to the LADCP data processing has been applied. However it is unclear whether this is a result of an elevated noise level or caused by real signals. Noise spectra (following Kunze et al., 2006) were fitted to shear spectral values at wavenumbers corresponding to wavelength of less than 40 m. For shear spectra closer than 2000 to the bottom during strong DWBC phases noise was found to be highest (up to  $5.8 \text{ cm s}^{-1}$ ), for all remaining spectra the noise level is significantly lower and the noise spectra shown in the bottom panel of Fig. 5.1 correspond to an upper estimate of the noise level of  $3 \text{ cm s}^{-1}$ .

The influence of the choice of the integration limits used in the integration of the shear (blue) and strain (red) spectra was estimated by calculating diapycnal diffusivities with different upper wavenumber limits (Fig. 5.2). To evaluate the sensitivity of the calculated  $K_\rho$  values to variations in the upper wavenumber limit in the integration of the shear spectra, the wavenumber limits in the integration of the strain spectra were kept constant and vice versa. Mean diapycnal diffusivities in different depth ranges were calculated for both flow situations of a strong and an absent DWBC over the continental slope. Mean  $K_\rho$  values were grouped depending on depth as the noise in the shear spectra is expected to increase with increasing depth due to the decrease in scatterers in the water column at greater depths.

Fig. 5.2b shows that the calculated  $K_\rho$  values do not strongly depend on the upper wavenumber limit (within the analyzed range between approximately 50 m and 160 m) during phases when the DWBC is not flowing over the continental slope. When the flow is strong (Fig. 5.2a) the calculated  $K_\rho$  values increase with increasing wavenumber/decreasing wavelength limit especially at depths below 2000 m and for wavelengths smaller than approximately 110 m. At this wavelength the noise (estimated by fitting the noise spectrum to the shear spectra) is below 10% in all spectra shown in Fig. 5.1. Even though it is not clear whether the elevated spectral values at higher wavenumbers close to the bottom during strong DWBC

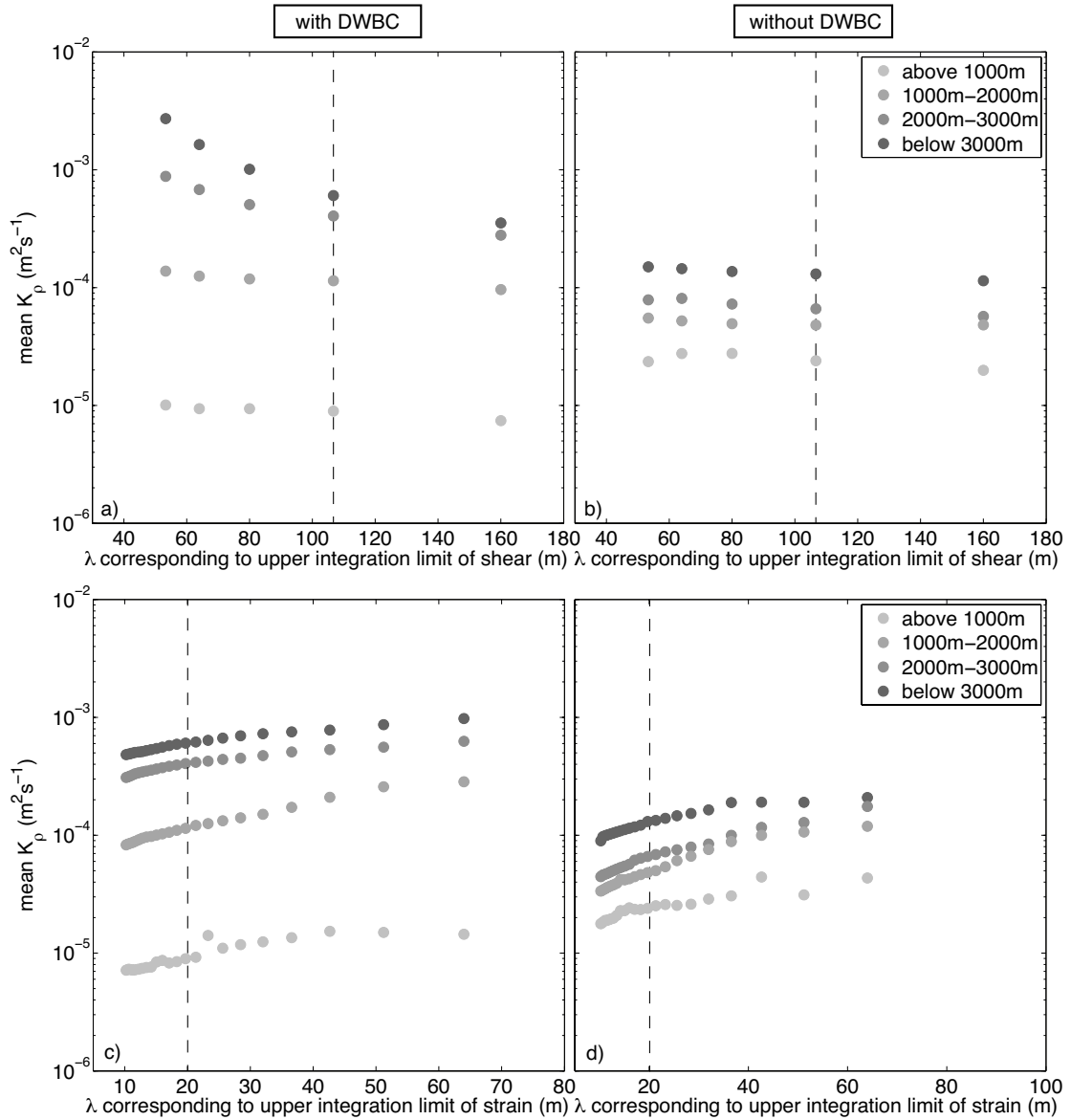


**Figure 5.2:** Sensitivity of the mean  $K_\rho$  in different depth ranges during phases of a strong DWBC (panels a and c) and during an absent DWBC (panels b and d) on the choice of the upper wavenumber/lower wavelength in the integration of the shear and strain spectra. Panels a and b show the response of the mean diapycnal diffusivity to variations in the upper wavenumber/lower wavelength limit. The low wavenumber limit was kept constant at a corresponding wavelength of 320 m and the wavenumber range used in the integration of the strain spectra was kept constant at a wavenumber range corresponding to wavelengths of 128 m – 20 m. Panels c and d show the sensitivity on variations in the upper wavenumber limit in the integration of the strain spectra. The low wavenumber limit was set to a corresponding wavelength of 128 m and the integration interval in the shear spectra was kept constant at a wavenumber range corresponding to wavelengths of 320 m – 110 m. Dashed lines denote chosen integration limits.

phases are mainly caused by noise or real signals, 110 m was chosen as the lower wavelength integration limit as it gives the most robust estimate of the energy level and avoids an overestimation of the mixing rate. The maximum change in  $K_\rho$  due to variations in the upper integration limit within the considered wavelength range roughly corresponds to a factor of 8 but typically ranges between 2 and 3.

No pronounced difference in the sensitivity of  $K_\rho$  on the upper wavenumber limit in the integration of the strain spectra between the two flow situations was found (Fig. 5.2c and d). In general  $K_\rho$  increases with decreasing upper wavenumber limit. As a small decrease in the calculated  $K_\rho$  values is found at a wavenumber corresponding to approximately 20 m in some depth bins, this was chosen as the upper wavenumber limit for the calculation of  $K_\rho$ . The maximum factor induced in  $K_\rho$  by varying the upper wavenumber limit in the integration of the strain spectra is approximately 4.

Based on the preceding analyses integration limits were chosen as 320 m – 110 m for the calculation of the shear variance and 128 m – 20 m for strain variance.

## 5.2 Internal wave available potential energy

As internal waves propagate, they induce disturbances of the ambient water column and cause vertical displacements of isopycnals. The amplitude and frequency of these disturbances (internal waves) will be analyzed with respect to variability in energy content and frequency distribution of the internal wave field.

During the deployment of the MOVE array especially the mooring at the continental rise, which is located directly in the core of the DWBC, was knocked down by up to several hundred meters. To account for high frequency mooring motions and to exclude these in spectral analyses of vertical displacements, measured temperatures were vertically interpolated from the original pressure time series ( $p$ ) onto 7-day lowpass filtered pressure time series ( $p_7$ ). Thus, temperature changes with periods smaller than 7 days which are only artifacts of the varying instrument depths are removed from the vertically interpolated temperature time series ( $T'$ )

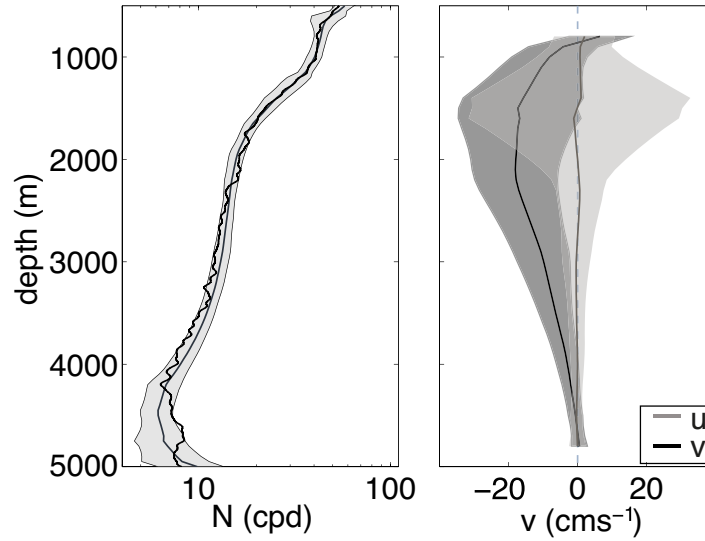


**Figure 5.3:** Left: Mean buoyancy frequency profile calculated from 13 CTD stations during 5 different cruises at the mooring location (black line), a 100 m vertical lowpass filter has been applied. Gray line denotes mean buoyancy profile determined from 14-day lowpass filtered MicroCAT data. Two standard deviations of the buoyancy frequency profile are denoted by the gray shading. Right: mean velocity profile of all current meters deployed during 2000-2005 with one standard deviation (gray shading).

and calculated vertical displacements are unaffected by mooring motions. Vertical displacements were then derived from temperature time series  $T'$  and the corresponding seven day lowpassed time series  $T_7$

$$\xi = -\frac{T' - T_7}{dT_7/dz}. \quad (5.6)$$

Vertical displacements are calculated from temperature data (instead of using density time series) because of the higher signal to noise ratio of the temperature measurements compared to the salinity/conductivity measurements and hence density data. Coherence spectra show no significant correlation between pressure and vertical displacements, thus calculated vertical displacements are not influenced by mooring motions. Vertical displacements over the 5-year period reach up to 250 m and amplitudes vary significantly over time (Fig. 7.5, upper panel). Enhanced vertical displacements can be seen at all depths during phases when the DWBC is at

the mooring location: Mean  $|\xi|$  of the 28-day segments of the time series that will be used in the spectral analysis show high correlations with the magnitude of the flow velocity parallel to the topography (between 0.74 – 0.91, Fig 7.5b).

To exclude temporal changes in internal wave spectra originating from changes in stratification rather than from the internal wave field itself, vertical displacements and temporally variable buoyancy frequencies  $N$  were used to calculate time series of available potential energies (APE):

$$\text{APE} = N^2 \xi^2 / 2. \quad (5.7)$$

Time series of buoyancy frequency  $N$  needed for the calculation of APE were determined by first differencing of 14-day lowpass filtered MicroCAT mooring data. Buoyancy frequency time series show considerable variability (up to a factor of two) especially in the lowest 1000 m.

For comparison a mean buoyancy frequency profile was derived from 13 CTD stations in direct vicinity of the westernmost mooring, measured during different seasons throughout the MOVE deployment periods (cf. Table 4.1). Resulting buoyancy profiles were 100 m lowpass filtered and are in good agreement with mooring time series of buoyancy profiles (Fig. 5.3) which proves the feasibility of calculating the buoyancy frequency profile from the mooring data despite the coarser resolution. By using the timeseries of the buoyancy frequency profile obtained from the mooring, temporal variations in  $N$  can be taken into account. Differences between moored and CTD profiles in the lowest 500 m most likely result from the low number of CTD stations in this depth range.

## 5.3 Internal wave spectra

For the analysis of internal wave kinetic and available potential energy mooring timeseries were divided into 28-day (temperature) or 14-day (velocity) half-overlapping segments, linearly detrended and a 20% cosine window applied to each segment. These segment lengths were chosen to resolve the entire internal wave frequency range and still allow for a good temporal resolution of the changes in

the internal wave field. The shorter segment length used in the analysis of the velocity time series was chosen due to the smaller amount of data compared to APE. Mean spectra over the entire five years as well as spectra measured during different DWBC strengths were calculated to investigate the influence of the DWBC and its interaction with the slope topography to the west of the mooring on the internal wave energy and frequency content.

As the mean flow follows the topography in southeastward direction (Chapter 3), the mooring-based velocities were rotated in an along (bearing  $117^\circ$ ) and a cross slope (bearing  $27^\circ$ ) component for spectral analysis.

## 5.4 Rotary spectra

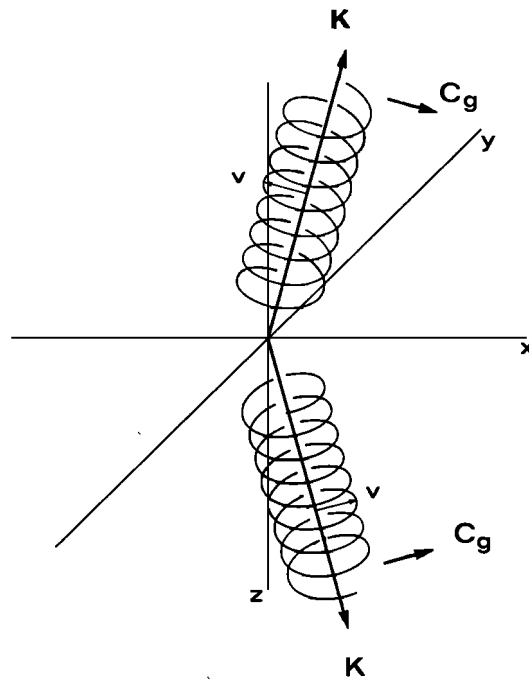


**Figure 5.4:** Propagation characteristics of internal waves including wavenumber vector  $\mathbf{k}$  and group velocity  $c_g$ . When looking downward a downward group velocity (energy propagation) can be identified by a clockwise rotation of the velocity vector  $\mathbf{v}$ , an upward propagation by a counterclockwise rotation. From Leaman and Sanford (1975)

Rotary component spectra (Gonella, 1972; Leaman and Sanford, 1975) of shipboard LADCP profiles can be used to separate clockwise and counterclockwise rotating velocity components and thereby identify the dominant energy propagation direction of the observed internal waves. Downward energy propagation can be identified by clockwise rotation (integrated clockwise variance of the rotary spectra,  $S^-$ ) and upward propagation by counterclockwise motions (integrated counterclockwise variance of the rotary spectra,  $S^+$ ) of the horizontal current vector  $\mathbf{v}$  with depth (Fig. 5.4).

Rotary spectra were calculated following Shcherbina et al. (2003) and LADCP profiles obtained during the considered five cruises were divided into 500 m long segments which overlapped by 400 m. To remove large scale vertical shear a second order polynomial was removed before a 20% cosine window was applied. However the higher wavenumber limit was kept at a corresponding wavelength of  $\lambda_{\min} = 110$  m (compared to  $\lambda_{\min} = 50$  m in Shcherbina et al., 2003) which was also used in the integration of the shear variance spectra in the finestructure parameterization.

The dominant energy propagation direction is determined using the following ratio:

$$r = \frac{S^- - S^+}{S^- + S^+} \quad (5.8)$$

where  $r = 1$  corresponds to purely downward and  $r = -1$  to purely upward energy transfer.

Changes in polarization characteristics of the observed internal waves and therefore also changes in the vertical energy propagation direction associated with changes in the DWBC strength and depth will be used to point to possible wave generation processes.



## 6 | Boundary current induced mixing

Diapycnal diffusivities (Eq. 5.1) and shear to strain variance ratios  $R_\omega$  obtained from CTD/LADCP data are divided into the two different flow situations (DWBC at the continental slope or no DWBC at the slope) and resulting transects including all stations available for the respective flow situation are shown in Fig. 6.1. During phases of a pronounced DWBC, the data show enhanced diapycnal diffusivities at the continental slope whereas only a very small intensification towards the bottom can be seen when the DWBC is absent. This indicates a pronounced change in the internal wave field and subsequent vertical mixing induced by the presence of strong currents like the DWBC at the continental slope.

In near inertial waves the particle movement is almost horizontal resulting in high vertical shear and small strain variance and consequently in higher shear to strain ratios  $R_\omega$ .  $R_\omega$  is a measure of the internal waves aspect ratio and if a single wave is assumed to dominate the observed variability,  $R_\omega$  can be related to its frequency by

$$R_\omega = \frac{\omega^2 + f^2}{\omega^2 - f^2} \quad (6.1)$$

(e.g. Henyey, 1991; Kunze et al., 1990; Polzin et al., 1995). The higher  $R_\omega$  values observed during DWBC phases (bottom panel in Fig. 6.1) might therefore indicate an increase in internal wave energy at near inertial frequencies.

Mean profiles of vertical diffusivities for the two velocity regimes indicate that the strong flow within the DWBC induces significantly elevated internal wave energy and subsequently vertical mixing along the continental slope up to approximately 1500 m above the bottom (Fig. 6.2). Here  $K_p$  reaches mean values of up to  $10^{-3} \text{ m}^2 \text{ s}^{-1}$  during phases when a pronounced DWBC is observed in the transect. When the DWBC is not flowing over the continental slope mean diapycnal diffusivities close to the seafloor are about an order of magnitude lower.

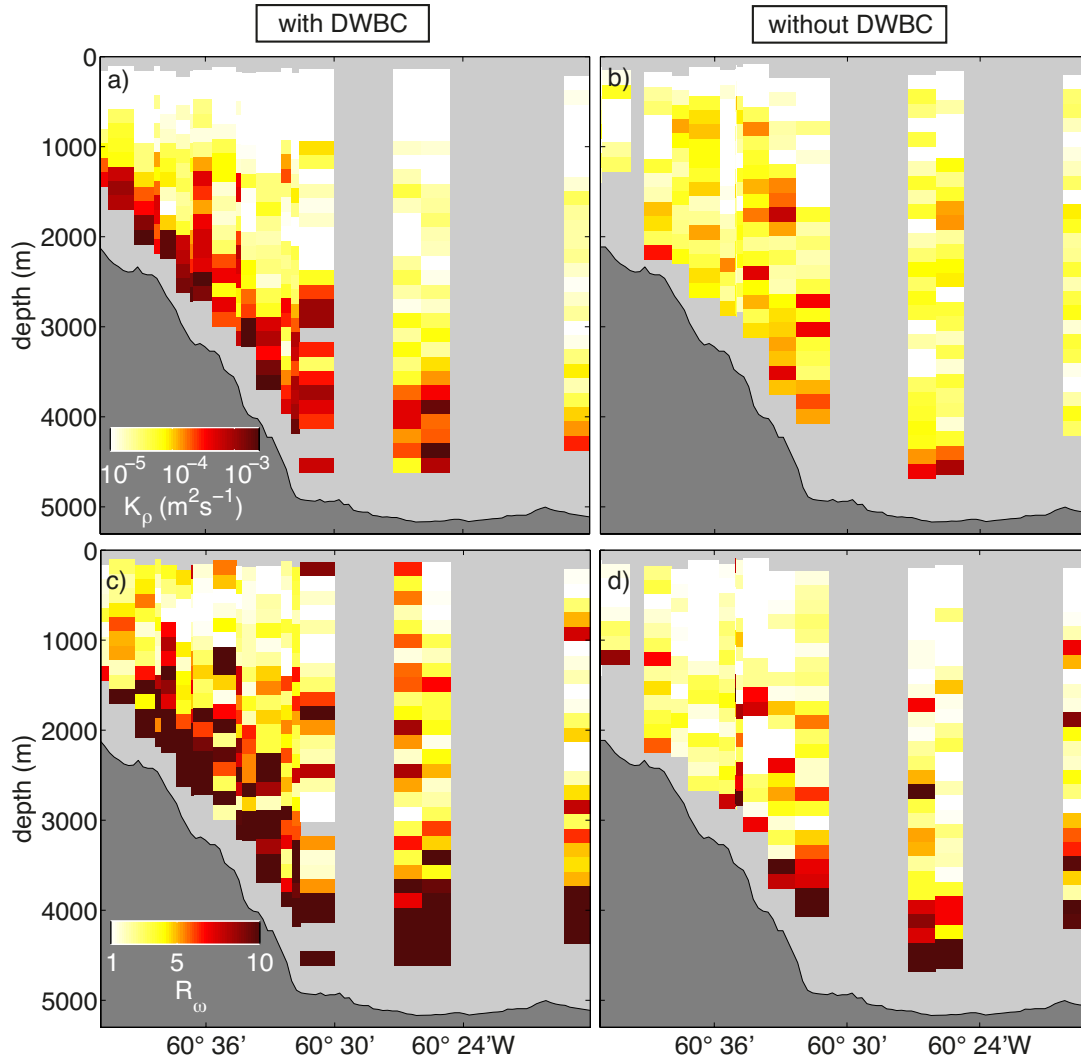


**Figure 6.1:** Sections of diapycnal diffusivities  $K_\rho$  calculated from shipboard measurements during times when the DWBC was present (So152, M53/3 and M62/1, panel a) and during times when it was absent (M66/1 and So171, panel b). Thereby each bar denotes one station. Shear to strain variance ratios  $R_\omega$  for both flow situations are shown in panels c) and d). Gray boxes denote bad data that were excluded from the analyses.

The influence of the choice of the integration limits for the shear and strain variances is assessed in Fig. 6.2b) and c) (see also discussion in Section 5.5.1). It can be seen that the exact magnitude of the calculated  $K_\rho$  values is sensitive on the integration interval especially for the shear variance in the lowest part of the watercolumn during strong DWBC phases (almost a factor of 7 in the bottommost

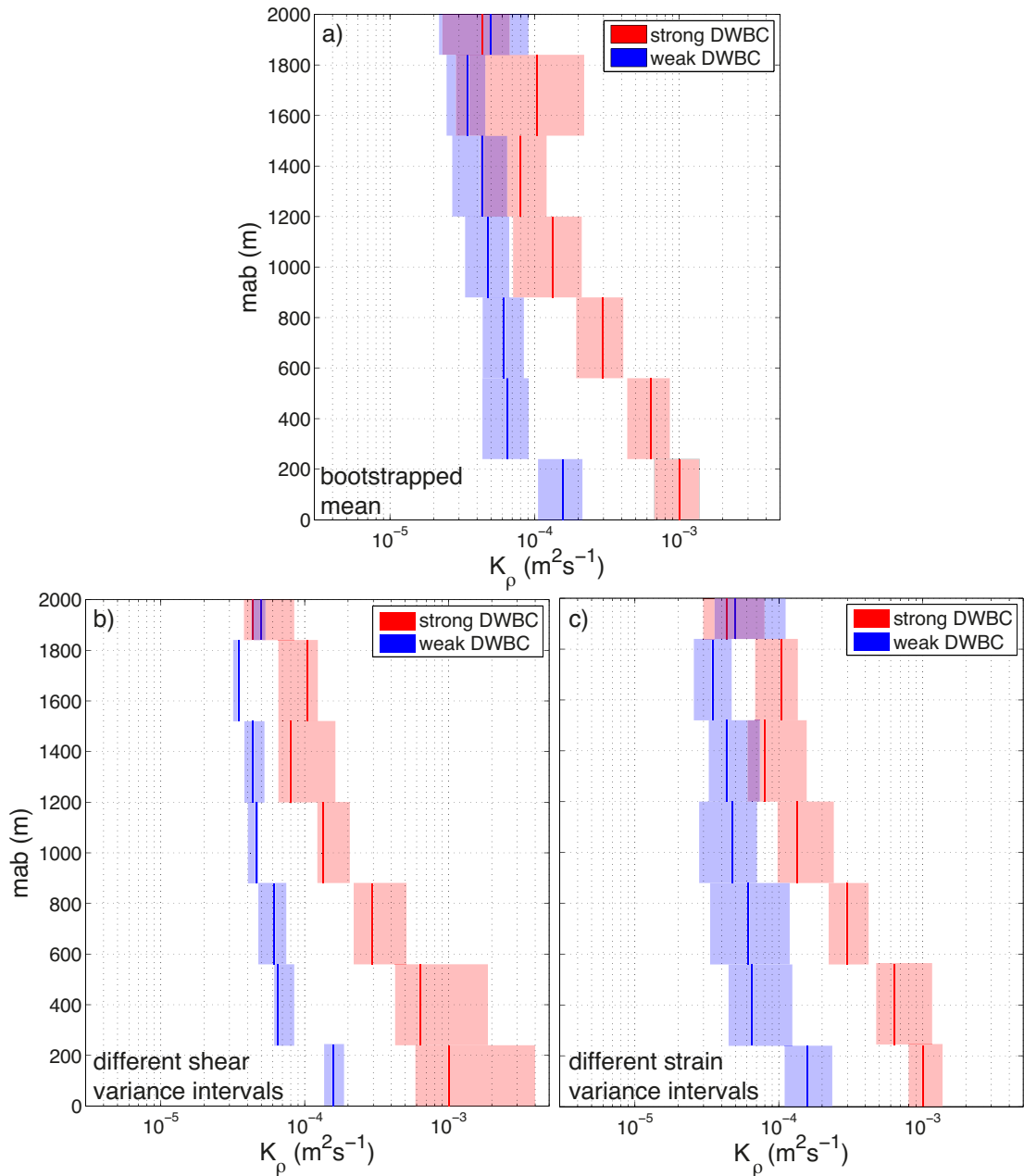


**Figure 6.2:** Panel a): Profiles of arithmetic means of vertical diffusivities for strong (red) and an absent (blue) DWBC as a function of meters above bottom (mab). Only the bottommost 2000 m are shown as higher up in the water column surface values from shallow stations start to influence the mean. Shading indicates 90% confidence intervals determined by bootstrapping of the  $K_\rho$  values. Panel b): Profiles of arithmetic means as in panel a) but shading indicates possible range of the mean value if the lowest wavelength in the integration interval of the shear variance is varied (between approximately 50 m and 160 m, see also Fig. 5.2) with constant strain variance integration limits. Panel c): as panel b) but for variations in the integration interval in the strain variance (lowest wavelength between approximately 10 m and 65 m).

segment between the extreme limits, Fig. 6.2b). The sensitivity of  $K_\rho$  on the integration intervals for the strain variance in contrast does not clearly depend on the flow situation or on depth.

Despite the given uncertainties in the calculation of  $K_\rho$  (cf. discussion in Chapter 5.1), the general pattern of enhanced vertical mixing during phases of a strong DWBC at the continental slope stays robust and is independent of the choice of the integration limits.

The observed increase in diapycnal diffusivities obtained from the finescale parameterization based on wave-wave interactions already is a strong indication for elevated internal wave energy during phases of a strong DWBC. The long-term response of the internal wave energy to changes in the current will be analyzed in the following Chapter using mooring timeseries of horizontal velocities and internal wave APE.

# 7 | Variability in the internal wave field induced by the DWBC

## 7.1 Internal wave kinetic energy

### 7.1.1 Mean spectra of internal wave kinetic energy

Time averaged velocity spectra were determined from sensors at similar depths during individual deployment periods. Velocity time series from the second, fourth and fifth deployment were combined to obtain a mean spectrum at an approximate depth of 900 m, time series from all deployment periods were used for the mean spectrum at a depth of roughly 1500 m, and from the first four deployments at a depth of 2200 m. The mean spectra are compared with the corresponding GM79 (Munk, 1981) predictions (Fig. 7.1) using local values of buoyancy frequency  $N_0 = 46$  cpd and  $b = 1827$  ( $e$ -folding scale of  $N(z)$ ), obtained from the mean temperature and salinity profiles from the CTD data.

The dominant spectral peak in the mean spectra is found at the M2 tidal constituent along with smaller peaks at the K1 and  $2 \times M2$  tidal frequencies. The peak at the tidal harmonic might be generated by interaction with the topography (Nikurashin and Legg, 2011). The variability in the cross slope velocity component in general is more energetic than in the along slope component except at the M2 tidal frequency.

No pronounced peaks occur at the inertial frequency in the mean spectra over the complete time span; an inertial peak is almost absent in the mean spectra at 2200 m depth; this will be discussed at the end of the section. The magnitude of horizontal velocity spectra is in good agreement with GM79 predictions except for the frequency range between M2 and the inertial frequency where spectral levels are below the GM prediction. Variability in spectral energy between individual

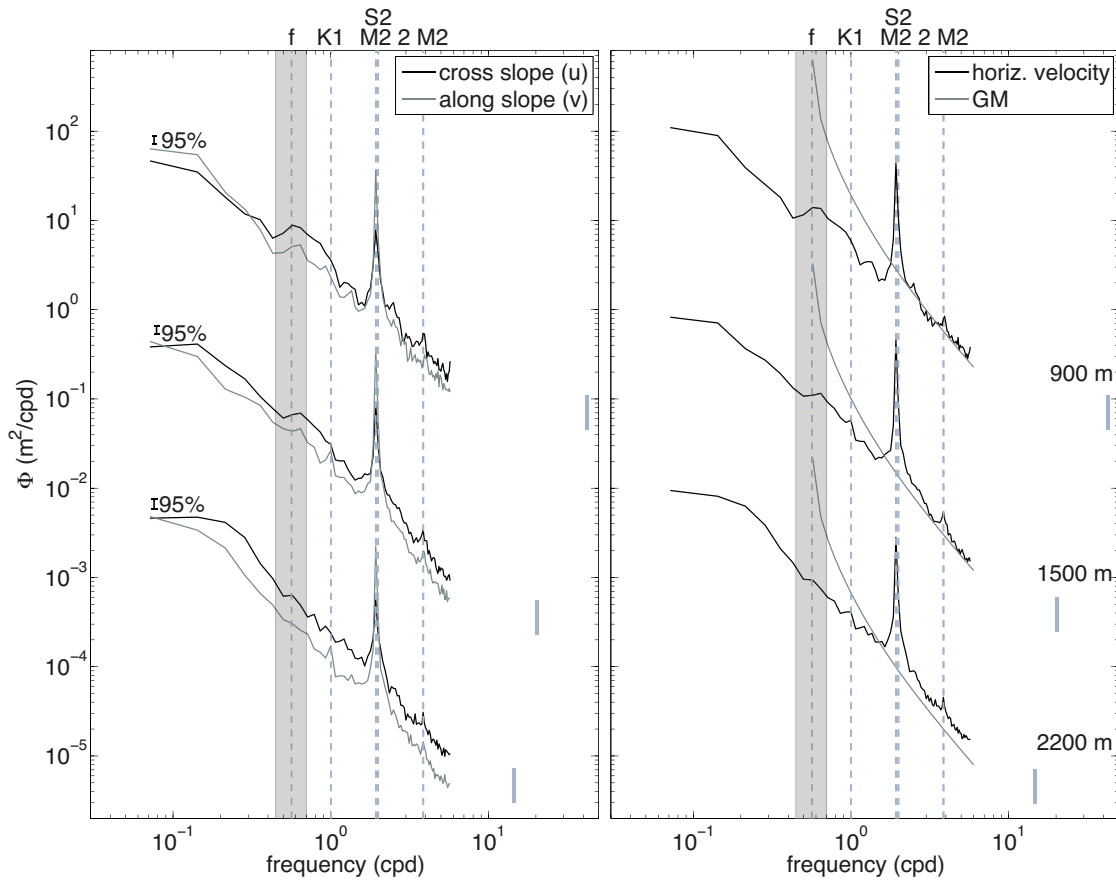


**Figure 7.1:** left: Average spectra of rotated horizontal velocities at depths of 900 m, 1500 m and 2300 m from all data available from the analyzed five deployments. Spectra are vertically offset and smoothed over 3 adjacent frequencies to reduce uncertainties in spectral magnitudes. Gray denotes spectra of along and black of cross slope velocity, 95% confidence intervals are shown on the left and dominant tidal, inertial and depth dependent buoyancy frequencies are denoted by vertical lines to the right of each spectrum. Gray shading around the inertial frequency indicates the range of the effective inertial frequency  $f_{\text{eff}}$  (see Chapter 7). right: Sum of horizontal velocity spectra (black) in comparison with the corresponding GM prediction (gray).

spectra reaches up to two orders of magnitude and it is only possible to obtain smooth spectra as shown in Fig. 7.1 because of the long time series available for this study.

## 7.1.2 Velocity dependence of internal wave kinetic energy

Significant changes in spectral magnitude and shape were found between the individual 14-day spectra demonstrating a high temporal variability in internal wave kinetic energy at both mooring locations. The highest spectral levels are found during times of strong southeastward flow (large negative  $v$ -component) in combination with a strong offshore flow (large positive  $u$ -component). Lowest internal wave energy is found for times of a northwest  $v$ -component together with an on-shore  $u$ -component. Taking this directional dependence into account rather than just considering the flow component parallel to the topography as the major influencing property, significantly increases the correlation between internal wave kinetic energy and the flow characteristics.

To investigate changes in spectra of horizontal velocity caused by the variability of the DWBC and the associated flow situation, spectra of 14-day segments were grouped according to  $v_{\text{slope}} = u - v$  where  $u$  and  $v$  are the cross and along slope velocity components (Chapter 5.3). Thereby  $v_{\text{slope}}$  is a mean velocity calculated individually at both moorings from the measurements of the RCM closest to the core of the DWBC (depending on deployment period between 1500 m and 2200 m) during the time of the data segment used for the calculation of the corresponding spectrum. It has its maximum for strong down-slope flow in a southeastward direction and is lowest for upslope flow in a northwestward direction (Fig. 7.2, panel a). A high  $v_{\text{slope}}$  could be an indication that further upstream the DWBC is closer to the slope than during times when there is a westward  $u$  component (reducing  $v_{\text{slope}}$ ). This would result in a weaker interaction of the strong flow within the DWBC with the slope topography.

Internal wave spectra were grouped according to the following intervals of  $v_{\text{slope}}$  (values in parenthesis for slope mooring):

- above a threshold of  $32.5 \text{ cm s}^{-1}$  ( $17.5 \text{ cm s}^{-1}$ )
- $15 \text{ cm s}^{-1} < v_{\text{slope}} < 32.5 \text{ cm s}^{-1}$  ( $7.5 \text{ cm s}^{-1} < v_{\text{slope}} < 17.5 \text{ cm s}^{-1}$ )
- $-2.5 \text{ cm s}^{-1} < v_{\text{slope}} < 15 \text{ cm s}^{-1}$  ( $-2.5 \text{ cm s}^{-1} < v_{\text{slope}} < 7.5 \text{ cm s}^{-1}$ )

- $v_{\text{slope}} < -2.5 \text{ cm s}^{-1}$  ( $v_{\text{slope}} < -2.5 \text{ cm s}^{-1}$  )

$v_{\text{slope}}$  was divided into four groups instead of considering just two flow situations (weak and strong flow) in order to show that there is a smooth transition in the response of the internal wave field on  $v_{\text{slope}}$  rather than an abrupt change at a specific velocity threshold.

Even though velocities within the DWBC are slightly decreasing towards the slope, shipboard measurements (Fig. 1, Stöber et al. (2008) their Fig. 6) indicate that velocities measured at the mooring locations are correlated with the flow directly over the slope. Thus, a correlation between the generation of internal waves and  $v_{\text{slope}}$  is expected.

Resulting mean spectra of rotated velocities in the different ranges of  $v_{\text{slope}}$  at depths of approximately 900 m and 2200 m are shown in Fig. 7.2 and Fig. 7.3. At 900 m depth (Fig. 7.2) an almost uniform increase of internal wave energy over the entire internal wave frequency range is associated with an increase in  $v_{\text{slope}}$  at both moorings. As in the mean spectra over the entire five years, energy is higher in cross than in along slope direction, except for the M2 tidal frequency where variability in along slope direction is higher, independent of the flow strength. The almost uniform increase in internal wave kinetic energy in all frequencies is in good agreement with findings of Polzin and Lvov (2011) who also found such an almost uniform increase during high internal wave kinetic energy periods at a depth of approximately 350 m using data obtained during the Long Term Upper Ocean Study (Lotus).

At 2200 m depth (Fig. 7.3), the changes in internal wave spectra are somewhat different. The intensification with increasing  $v_{\text{slope}}$  is more pronounced in low, near inertial frequencies. Furthermore, the increase is significantly stronger on the continental slope than at the continental rise despite the slightly weaker flow closer to the coast. This indicates a generation of the observed internal waves westward of the mooring locations where the DWBC core directly interacts with the slope topography.

The increase in spectral energy in subinertial frequencies during high  $v_{\text{slope}}$  indicates an increased eddy activity or a stronger meandering of the DWBC during these times.

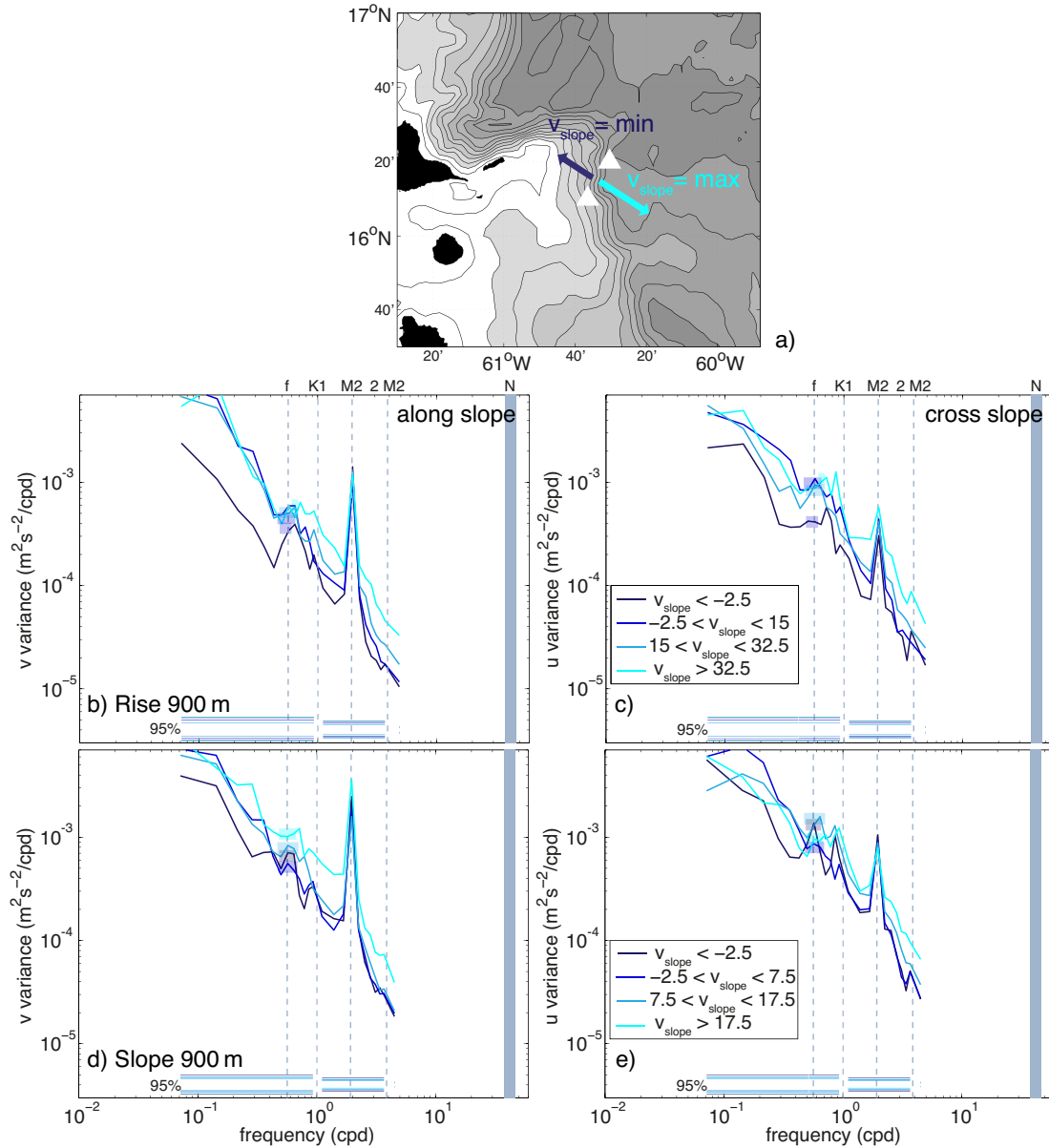


**Figure 7.2:** a) During high  $v_{\text{slope}}$  water is flowing down the continental slope in a southeastward direction, during lowest  $v_{\text{slope}}$  it is flowing upslope in a northwestward direction. b) Spectra of along ( $u$ ) and c) cross slope ( $v$ ) horizontal kinetic energy at the continental rise and at the continental slope (panel d and e) at a depth of 900 m grouped according to  $v_{\text{slope}}$ . At the continental rise data is available from deployment periods two, four and five, for the mooring located at the continental slope data from all deployments is combined to obtain the spectra. Inertial frequency as well as major tidal constituents are denoted by dashed lines, the range of buoyancy frequency  $N$  is denoted by the gray bar and 95% confidence intervals are shown at the bottom of each panel. The number of individual spectra going into each mean spectra is accounted for in the different confidence intervals. To decrease spectral uncertainties, spectral values at frequencies above 1 cpd were averaged over four adjacent frequencies, above a frequency of 4 cpd 25 values were averaged. Intervals of the respective  $f_{\text{eff}}$  are denoted by blue shadings around the inertial frequency.

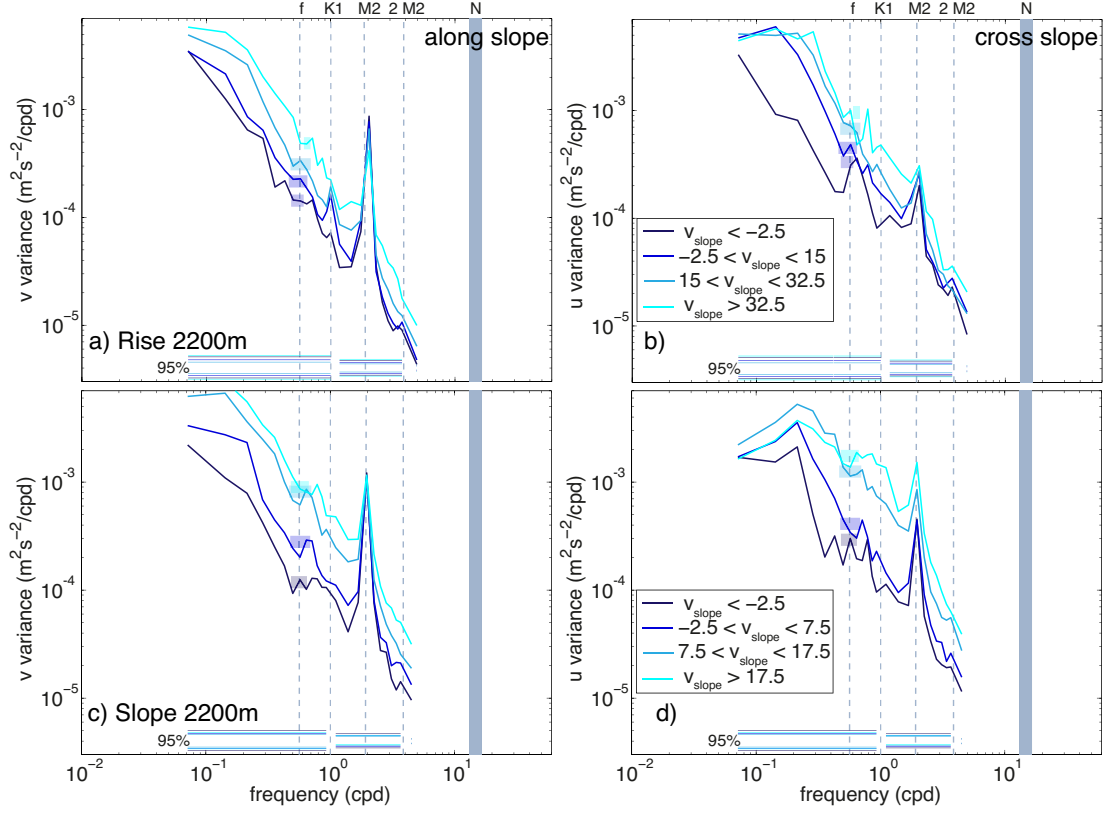


**Figure 7.3:** As Fig. 7.2 but at a depth of 2200 m. Data at the continental rise are available from deployment periods one – four and from all deployments at the continental slope.

The effective inertial frequency  $f_{\text{eff}}$ , being the low frequency limit of internal waves, depends on latitude and on relative vorticity  $\zeta$ :

$$f_{\text{eff}} = f + \zeta/2 \quad (7.1)$$

Due to the highly variable current in the study area the effective inertial frequency changes over time and can be approximated by  $f_{\text{eff}} \approx f + \frac{dv}{dx}$  since  $\frac{du}{dy} \ll \frac{dv}{dx}$  in this area.  $\frac{dv}{dx}$  is estimated by the difference in  $v$  between the two moorings at a depth of 1500 m as this depth approximately corresponds to the depth of the DWBC core and data are available over the entire period. A mean  $f_{\text{eff}}$  was calculated for each 14-day interval. Due to the strong and variable flow within the DWBC, the resulting effective inertial frequencies vary between approximately  $4.5 \times 10^{-1}$  cpd and  $7 \times 10^{-1}$  cpd. In Figs. 7.1, 7.2 and 7.3  $f_{\text{eff}}$  shows the range of the low frequency

internal wave limit for the different intervals of  $v_{\text{slope}}$ . Due to the large variability in  $f_{\text{eff}}$  (induced by  $\frac{dv}{dx}$ ) the transition from the internal wave frequency range to the subinertial range is either blurred in the mean spectra for the different  $v_{\text{slope}}$  or there are several peaks at the respective  $f_{\text{eff}}$  (see Fig. 7.3.d where three isolated peaks at different  $f_{\text{eff}}$  are visible for  $v_{\text{slope}} < -2.5 \text{ cm s}^{-1}$ ). The high variability of  $\frac{dv}{dx}$  likely leads to the blurring of the inertial peak in the mean spectra of the u and v-components (Fig. 7.1).

## 7.2 Internal wave available potential energy

### 7.2.1 Mean spectra of internal wave potential energy

Time averaged spectra of available potential energy measured by instruments deployed at similar depths during all five deployment periods were calculated from half-overlapping 28-day segments. The most prominent spectral peaks are found at the M2, S2 and K1 tidal frequencies (Fig. 7.4). Variability in the near inertial frequency range decreases towards the seafloor well below the prediction of the GM-model whereas the available potential energy observed in internal waves with high frequencies close to N at 1200 m depth are elevated compared to the GM prediction. These might be generated by wave trapping (Munk, 1981) by the local stratification. Even though the mean buoyancy frequency decreases with depth, a local maximum in N can occur at approximately this depth in the study area. High frequency waves would be trapped in this depth range of the local maximum in N which would result in the observed increase in high frequency internal waves (see also discussion in Chapter 8).

Comparatively high variability in frequencies below the inertial frequency in combination with the variable effective inertial frequency  $f_{\text{eff}}$  (discussed in Chapter 7)

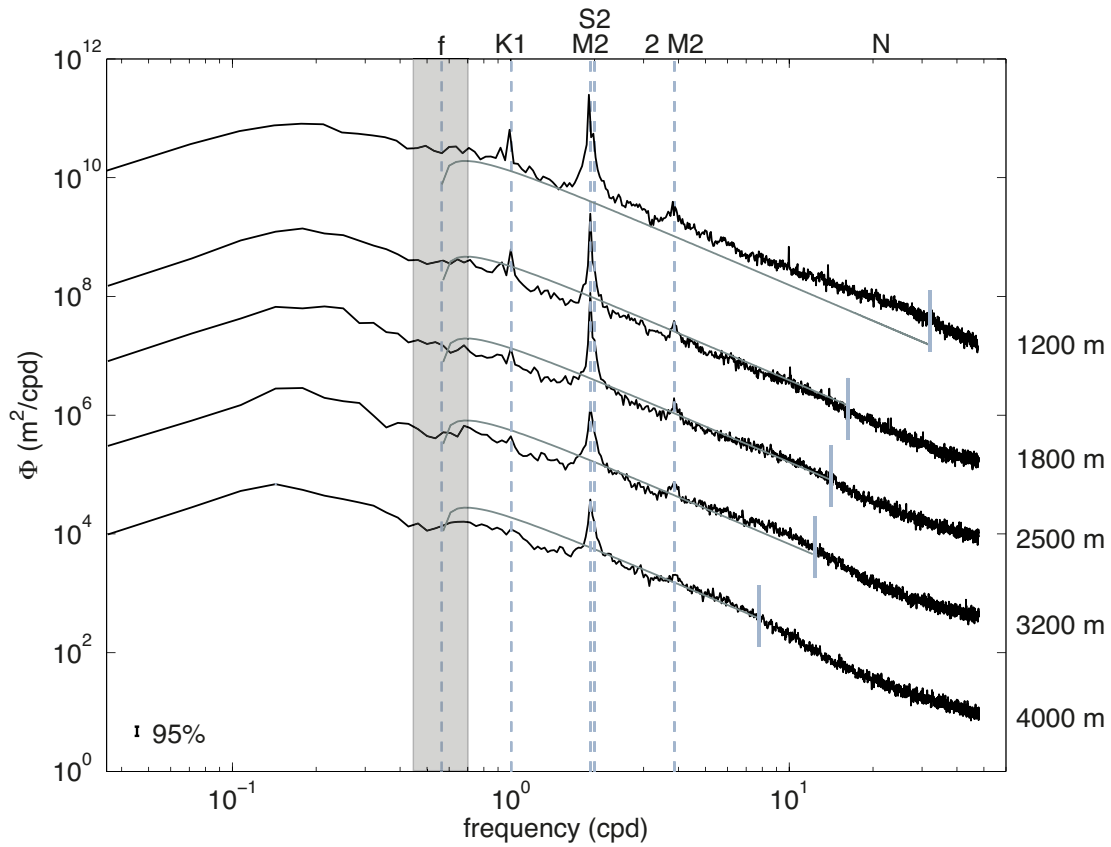


**Figure 7.4:** Mean spectra of available potential energy calculated from instruments in the respective depths using data from all deployment periods (black lines). Corresponding prediction of the GM79 spectra are shown in gray, 95% confidence interval is denoted by the vertical black line in the lower left corner and the range of  $f_{\text{eff}}$  at the depth of the DWBC core is denoted by gray shading. Spectra were averaged over 15 adjacent frequencies and depth dependent buoyancy frequencies are denoted by vertical lines to the right of each spectrum.

blur the transition between subinertial and internal wave frequency regimes in these mean spectra. Only a weak decrease in variability can be seen above the local buoyancy frequencies which will be discussed in Chapter 8.

## 7.2.2 Velocity dependence of internal wave available potential energy

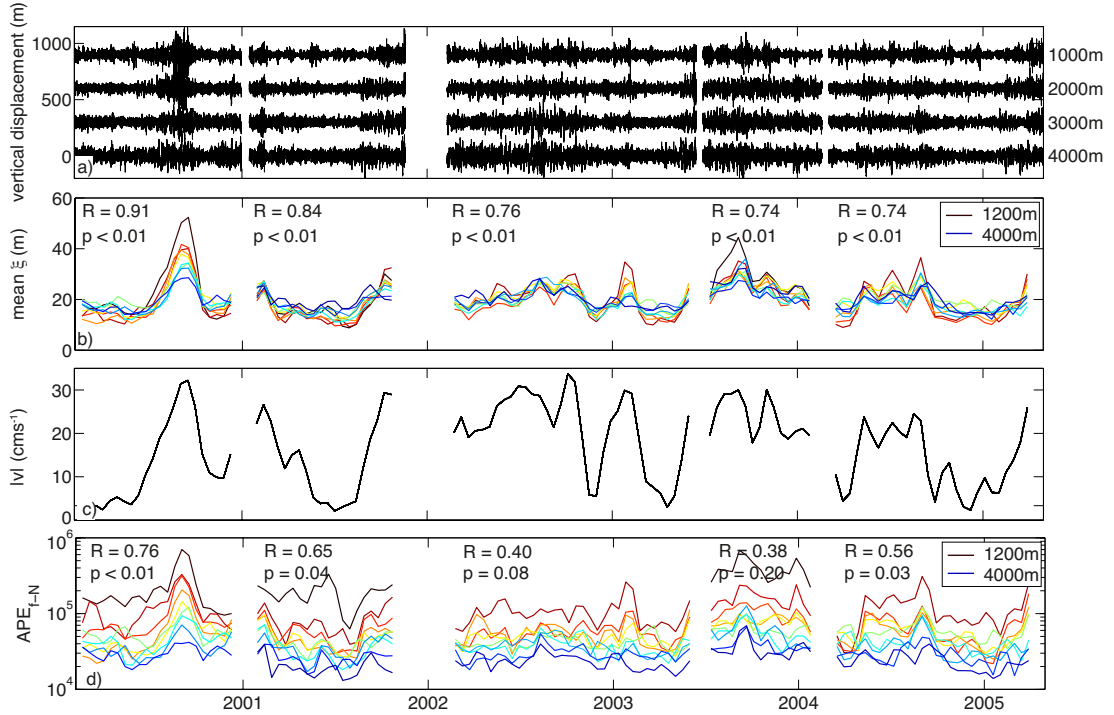


**Figure 7.5:** a) Vertical displacements calculated from temperature time series measured at the mooring at the continental rise. b) Mean  $|\xi|$  during the same 28-day half overlapping segment of the time series that were used for the calculation of  $|v|$ . c) Time series of 7-day lowpass filtered  $|v|$  at a depth of approximately 1500 m. d) Internal wave spectra of APE integrated between  $f$  and  $N$ . Colors denote deployment depths from 1200 m (dark red) to 4000 m (blue). Correlation coefficients ( $R$ ) and  $p$ -value ( $p$ ) between  $|\xi|$  and  $|v|$  (panel a) or internal wave APE and  $|v|$  (panel d) for each deployment period are given.

The time series of APE were split into 28-day, half overlapping segments, and spectra were calculated for each section in order to study the influence of the DWBC. Total internal wave APE at depths below 1200 m (in and below the DWBC) was determined from each spectrum of the 28-day segments by integrating from the inertial frequency  $f$  to the local buoyancy frequency  $N$ :

$$\langle APE \rangle = \int_f^N APE(\nu) d\nu \quad (7.2)$$

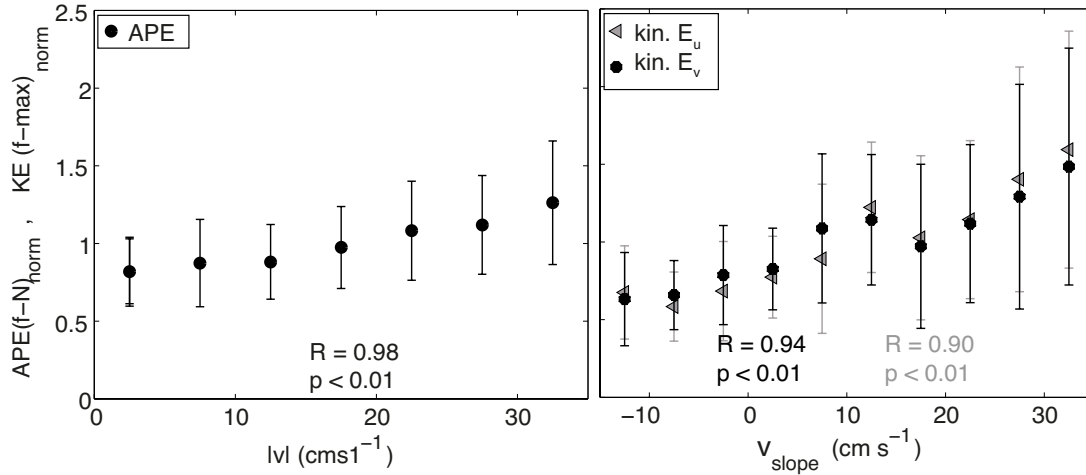


**Figure 7.6:** left: Integrated internal wave APE at and below the depth range of the DWBC (below 1200 m) binned with respect to  $|v|$ . right: kinetic energy (integrated between  $f$  and 1.8 cpd and 2.2 cpd to the maximum resolved frequency to exclude variability in the integrated kinetic energy due to variability in the tidal signal) at a depth of approximately 2200 m as a function of  $v_{slope}$ . Along slope component is denoted by black circles, cross slope component by gray triangles. Before mean values were calculated individual values were normalized by the mean of all integrated values obtained from the respective instrument. Thereby variability due to different deployment depths was eliminated. Standard deviations are shown for each mean value, correlation coefficients ( $R$ ) and p-values ( $p$ ) are given for each property.

Thereby the lower integration limit was kept constant at the inertial frequency  $f$  at depths below 3000 m (below the DWBC) and taken as  $f_{eff}$  at depths between 1200 m and 3000 m. As before  $f_{eff}$  was calculated at a depth of approximately 1500 m that corresponds to the depth of the DWBC maximum and here data from both moorings were available for all deployments. However taking a variable lower integration limit does not strongly change the results compared to those obtained with the fixed limit at the inertial frequency  $f$ .

APE varies significantly over time and with depth (Fig. 7.5, lower panel). However, no significant difference in the correlation between APE and  $v_{slope}$  and the correlation between APE and the absolute value of the flow component parallel to the slope ( $|v|$ ) was found. Therefore the directional dependence included in  $v_{slope}$  will be dropped and the correlation between internal wave APE and  $|v|$  will be studied in this chapter.

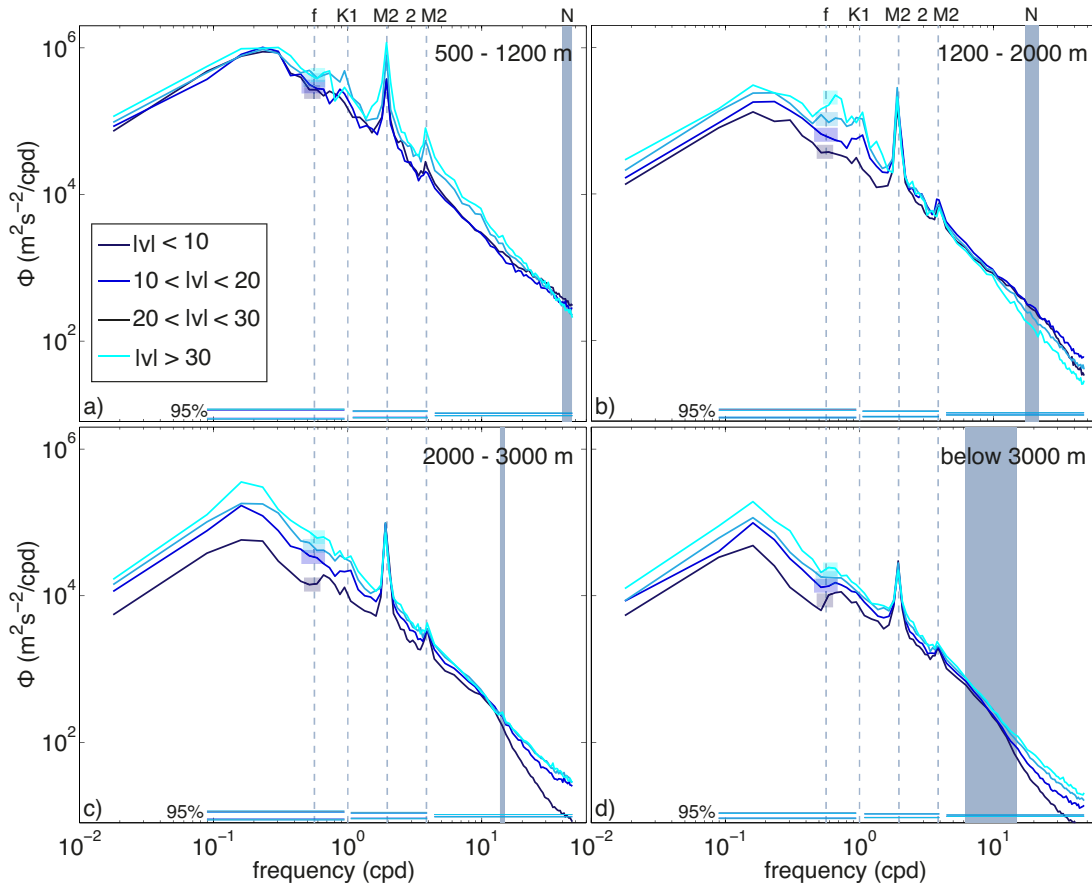


**Figure 7.7:** Power spectral density of APE in four different depth ranges at the continental rise: 500 m – 1200 m (panel a), 1200 m – 2000 m (panel b), 2000 m – 3000 m (panel c) and below 3000 m (panel d) grouped according to  $|v|$ . Inertial frequency as well as major tidal constituents are denoted by dashed lines, buoyancy frequency  $N$  is denoted by gray bar and 95% confidence intervals are shown at the bottom of each panel. The number of individual spectra going into each mean spectra is accounted for in the different confidence intervals. To decrease spectral uncertainties, spectral values at frequencies above 1 cpd were averaged over four adjacent frequencies, above a frequency of 4 cpd 25 values were averaged. Intervals of the respective range of  $f_{\text{eff}}$  are denoted by blue shadings around the inertial frequency.

Highest APE was found during times of high  $|v|$ , lowest for times of a weak  $|v|$ . Mean correlation coefficients between internal wave APE and  $|v|$  of individual deployment periods vary between 0.38 and 0.76. However the lowest correlations (and highest p-values) were found during the deployment periods where the variation in  $|v|$  is lowest and therefore its effect on the internal wave field is hard to determine. In order to analyze the influence of the DWBC strength on internal wave APE, all

APE values measured at and below the depths of the DWBC (below 1200 m) were binned in  $5 \text{ cm s}^{-1}$  intervals of mean  $|v|$  for individual 28-day segments. The velocity measured by the RCM closest to the depth of the DWBC-maximum was chosen for the calculation of  $|v|$ . Prior to the calculation of mean APEs in each velocity bin, all integrated APEs measured by each individual MicroCAT were normalized by the integration interval and by the mean of all APE values calculated from data obtained from the respective sensor. Thus changes in APEs due to variances in the ranges of integration (originating from changes in the upper integration limit due to different buoyancy frequencies  $N$  at different depths or in the lower limit due to  $f_{\text{eff}}$ ) and different APE energy levels at different depths are eliminated. Only relative changes in APE independent of stratification or  $f_{\text{eff}}$  remain which makes it possible to combine measurements from different depths to study the effects of the DWBC on the internal wave field (more specifically on the magnitude of internal wave energy per frequency). Otherwise this dependence would be blurred for example by the different upper integration limits ( $N$ ) in different depths.

A clear relation (correlation coefficient between mean APE in each velocity bin and  $|v|$  of 0.98) between internal wave APE and  $|v|$  can be seen (left panel in Fig. 7.6). Integrated internal wave kinetic energy at a depth of 2200 m (depth of the DWBC maximum) shows a very similar dependence on  $v_{\text{slope}}$  (correlation coefficients  $R_v = 0.94$  and  $R_u = 0.90$ , right panel in Fig. 7.6). In this integration the M2 tidal peak (1.8 cpd – 2.2 cpd) was excluded as variations in the tidal strength blur the relation of the internal wave kinetic energy on  $v_{\text{slope}}$  and the upper integration limit was set to 6 cpd (maximum resolved frequency).

Other processes next to the DWBC like e.g. wind intensity or eddies also modulate the internal wave field and the APE, which decreases the correlation between APE/kinetic energy and the flow.

Similar as for horizontal velocities, both the spectral amplitude and shape of  $\text{APE}(\nu)$  change over time and depend on the DWBC strength and on instrument depth. Therefore all spectra of 28-day data segments were grouped depending on the DWBC strength (now using  $10 \text{ cm s}^{-1}$  velocity intervals of  $|v|$ ), and according to their deployment depth: above the DWBC (500-1200 m), within the DWBC but away from (local) bottom topography (1200-2000 m), in the DWBC closer to slope topography (2000-3000 m) and below the DWBC ( $> 3000 \text{ m}$ ) (Fig. 7.7).

Spectral energy is elevated at all depths during times of a strong DWBC at the mooring position, but differences can be seen in the slope of spectra. These differences depend on depth and are similar to findings in the spectra of horizontal velocities: above the DWBC (500 m – 1200 m, Fig. 7.7.a) the spectral slope remains constant during high  $|v|$  with a small, almost constant increase in all internal wave frequencies up to 10 cpd.

In and below the DWBC (1200 m – bottom) the strongest increase in internal wave APE during high  $|v|$  is found in the near inertial frequency range. Above the  $2\times M2$  tidal frequency there is no (depth range 1200 m – 2000 m, Fig. 7.7.b) or a very small increase (depth range 2000 m – bottom, Fig. 7.7.c and d) in APE. The increase in APE in near inertial frequencies is strongest between 1200 m and 3000 m which corresponds to the depth range of the DWBC and indicates a generation of the observed waves by the interaction of the DWBC with the slope topography to the west of the moorings.



## 8 | Discussion

### 8.1 Diapycnal mixing

In order to analyze the influence of the DWBC on the intensity of vertical mixing, diapycnal diffusivities  $K_\rho$  were obtained from a finescale parameterization based on CTD and LADCP measurements from five cruises (2000-2005) (Fig. 6.1). It was possible to analyze the dependence of vertical mixing intensities on different background flow conditions as two of these cruises were carried out during a weak DWBC in the study area and three during a strong DWBC.

A sensitivity test of the calculated diapycnal diffusivities on the upper wavenumber limit in the integration intervals in the shear and strain spectra was carried out. Intervals corresponding to wavelengths of 320 – 110 m for shear and 128 – 20 m for strain variance were identified as suitable intervals (Chapter 5.1).

Significant differences in mixing rates were found in the deepest part of the profiles up to 1500 m above the bottom. Here elevated mean values of  $K_\rho$  of up to  $10^{-3} \text{ m}^2 \text{ s}^{-1}$  were observed during times when a pronounced DWBC was found close to the slope. This is about an order of maximum higher than mixing rates found during weak flow. Enhanced generation of internal waves due to interactions of the DWBC with the topography to the west of the mooring location and their subsequent local breaking is a possible mechanism resulting in the observed pattern of vertical mixing.

The shear/strain variance ratio  $R_\omega$  is a measure of the internal waves aspect ratio and can be related to its frequency (e.g. Henyey, 1991; Kunze et al., 1990; Polzin et al., 1995). Elevated values during DWBC phases indicate an increase especially of near inertial waves during these times.

## 8.2 Internal wave energy from timeseries

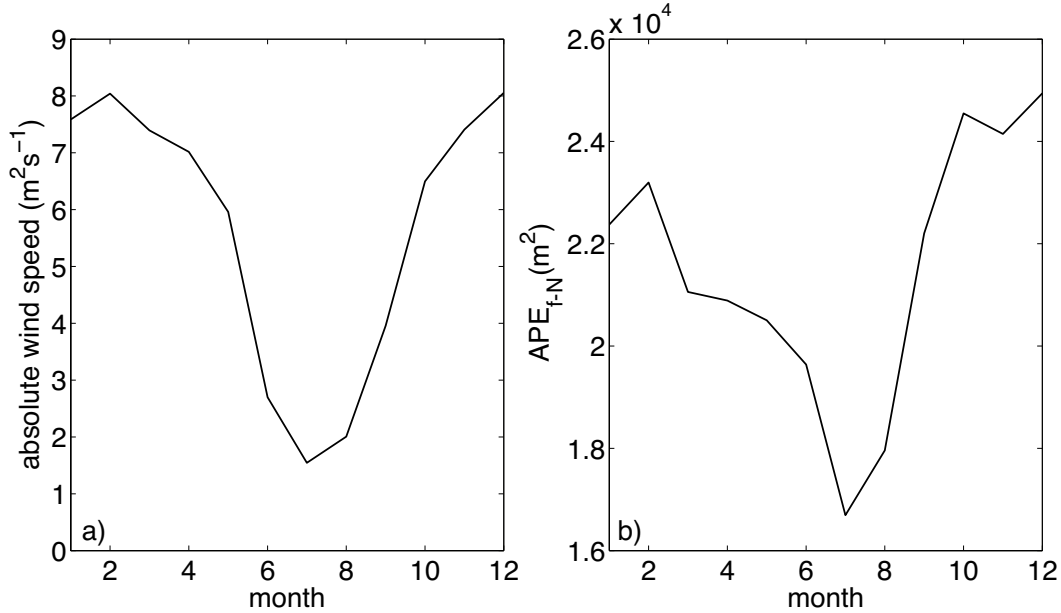


**Figure 8.1:** a) Mean monthly wind speed at the central mooring of the MOVE array in the years 2000 – 2005 from NCEP reanalysis wind data (Kalnay et al., 1996). b) Mean monthly integrated internal wave APE at the central MOVE mooring (M2, Fig. 3.1) from data obtained during the considered five deployment periods from all instruments located at depths between 1200 m and approximately 5000 m (depths range where data is available during all considered deployment periods).

Five continuous years of velocity and temperature time series from two boundary current moorings of the MOVE array were used to analyze temporal variability in the energy and frequency content of the internal wave field. Unlike in the open ocean where the energy contained in internal waves is strongly related to the wind field and therefore shows a seasonal cycle with a minimum in local summer (Fig. 8.1 and e.g. Alford, 2003), the variability in DWBC strength and position was found to be the mayor factor influencing the internal wave field at the location of the two boundary current moorings. For this study velocity and temperature measurements from one mooring located at the continental rise are supplemented by velocity time series of a mooring located further inshore on the continental slope. The mooring-based velocity time series were used to obtain internal wave spectra

for along and cross slope velocities while internal wave APE spectra were calculated from the temperature time series. Both types of spectra show a consistent dependence on both the DWBC strength and on depth (Fig. 7.2, Fig. 7.3 and 7.7). During strong flow energy is elevated in the entire internal wave frequency range at both moorings but spectral characteristics change significantly with depth. At depths shallower than the DWBC the increase in energy is nearly uniform over almost the entire internal wave frequency range. Below 1200 m however, the strongest increase is found at near-inertial frequencies, whereas energy in frequencies larger than that of the  $2\times M2$  tidal constituent remains almost unchanged. This is in good agreement with the generation process for low frequency, near inertial waves proposed by Nikurashin and Ferrari (2010b) as here the DWBC strongly interacts with the slope topography to the west of the mooring where the local water depth equals the depth of the DWBC core. At depths below the DWBC core (below 3000 m) the increase in energy in the near inertial frequency range is still visible but not as pronounced as at the depth of the core.

The increase in low frequency internal wave kinetic energy within the depth range of the DWBC at the continental slope is consistent with a source region close to the continental slope mooring. Wave breaking might have dissipated some of the energy of the generated waves before they reach the continental rise mooring, leading to a slightly smaller increase at this mooring during phases of a strong DWBC.

## 8.3 High frequency variability as proxy for mixing intensity

The high temporal resolution of measured temperature fluctuations, and thus vertical displacements, make it possible to include the high frequency variability above the buoyancy frequency into the analysis. Variability originating from vertical mixing, generated by breaking internal waves, is found in this high frequency range. This makes it a proxy for vertical mixing strength and was therefore analyzed to study whether the increase in internal wave energy also leads to an increase in the local vertical mixing intensity. Significant differences in the response of high fre-

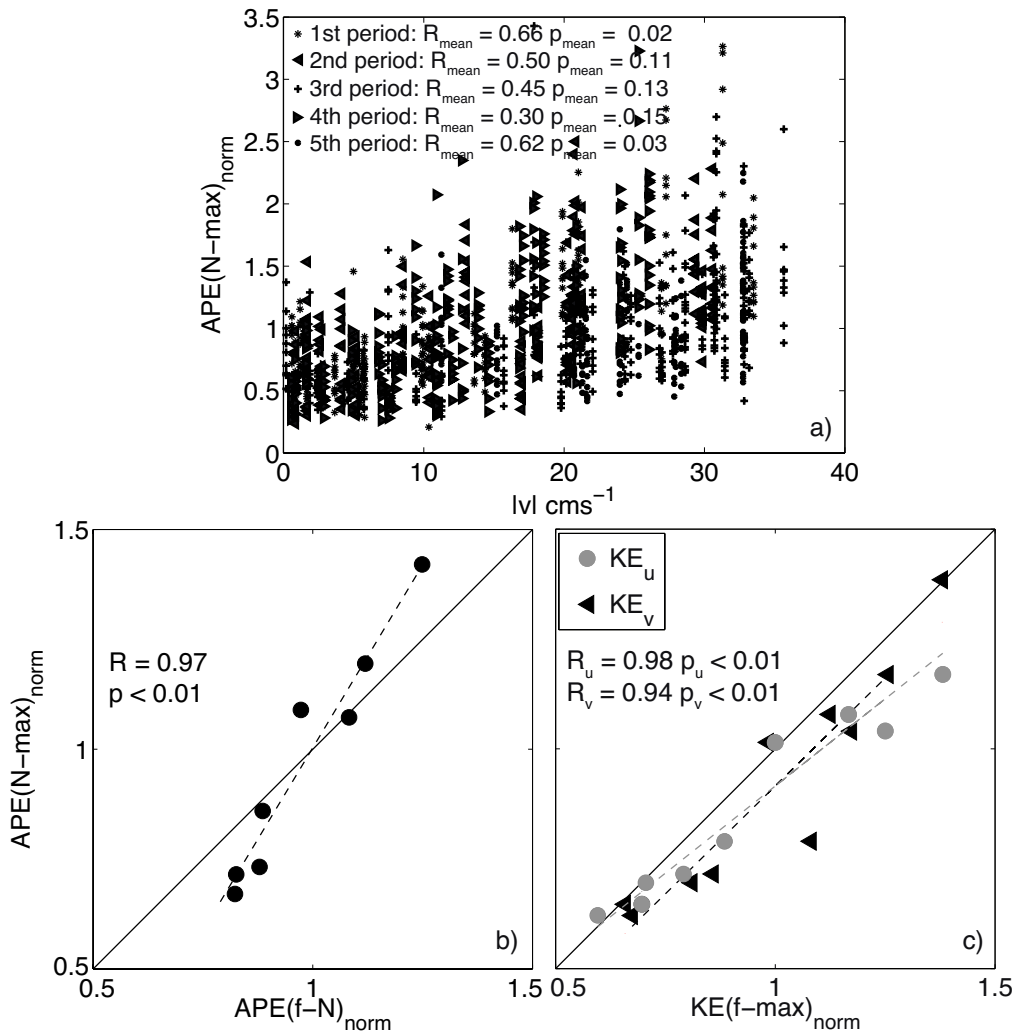


**Figure 8.2:** a) Dependence of normalized high frequency variability as indicator for vertical mixing intensity on  $|v|$ . Mean correlation coefficients ( $R$ ) and p-values ( $p$ ) for the individual deployment periods are given. b) Dependence of normalized high frequency variability on normalized integrated APE in the internal wave frequency band. Dots denote mean values in the velocity intervals used in Fig. 7.6, correlation coefficient ( $R$ ) and p-value are given on the left. For both plots data from instruments below 2000 m were used. c) Correlation between internal wave kinetic energy and high frequency variability in APE. As in Fig. 7.6 data from a depth of approximately 2200 m were used and the M2 tidal frequency was excluded from the integration.

quency variability to the DWBC strength were found between the different depth ranges in which the temporal resolution of the measurements resolves this frequency range (Fig. 7.7): Between 1200 m and 2000 m, energy in frequencies above the lo-

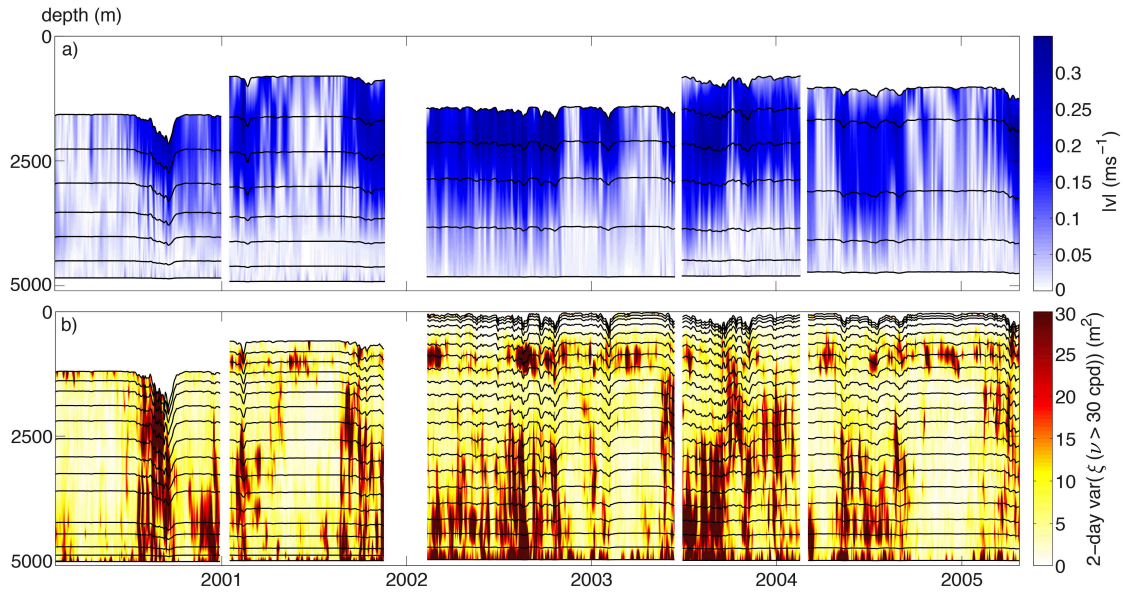
cal buoyancy frequency remains almost constant and independent of the DWBC strength even though internal wave APE is elevated during strong flows. Below 2000 m in contrast, there is a pronounced increase during strong DWBC phases, indicating intensified vertical mixing during these times.

Fig 8.2a shows a scatterplot of the correlation between the variability in the high frequency range and the flow component parallel to the topography  $|v|$ . For this plot APE spectra obtained from instruments deployed below 2000 m were integrated in the frequency range between  $N$  and 36 cpd as this is the maximum frequency range resolved by all instruments. To account for the differences in the integration intervals due to differences in  $N$ , integrated values were normalized by the respective frequency range. Furthermore integrated values were normalized by the mean of all values measured by the respective instrument, thereby relative changes of variability in the high frequency range are obtained. Correlation coefficients are significant (0.45 – 0.66) except for the fourth deployment period (0.30) where only small changes in  $|v|$  occur.

Possible mechanisms resulting in the observed increase of high frequency variability at greater depths during times of a strong DWBC would be an interaction of the generated internal waves with the topography of the continental slope or an increase in the generation of lee waves which then propagate their energy to high frequency waves via the nonlinear energy cascade. Hence, the large difference in mixing intensity during different DWBC phases shows the importance of local properties, especially strong currents, for the internal wave field and the associated mixing processes.

Direct comparison of normalized values of internal wave APE and kinetic energy with the corresponding APE in the high frequency range, both binned according to the same  $5 \text{ cm s}^{-1}$  intervals of  $v_{\text{slope}}/|v|$  used in Fig. 7.6, shows a high linear correlation of internal wave available potential energy (Fig 8.2b) and kinetic energy (Fig 8.2c) with high frequency variability and provides support for the applicability of finescale parameterizations.

The dependence of the variability in the high frequency range on internal wave APE is not 1:1, but an increase in internal wave APE leads to a disproportionately high increase in the high frequency range. In contrast the ratio of the increase in internal wave kinetic energy and high frequency variability is almost 1:1. As the



**Figure 8.3:** Time series of  $|v|$  (a) and of 2-day variances of high-pass filtered vertical displacements (b) with depth of measurement instruments denoted by black lines.

strongest increase in internal wave energy occurs in the near inertial range during phases of a strong DWBC, relative changes in spectral energy are more pronounced in internal wave kinetic energy than in available potential energy.

To study temporal changes in the inferred mixing intensity using the high frequency variability, time series of vertical displacements were high-pass filtered down to a frequency of 30 cpd and the 2-day variance was computed at all depths (Fig. 8.3). 30 cpd was chosen as cut off frequency as a trade off between the available temporal resolution and the maximum buoyancy frequencies at different depths. It is above the upper limit of the internal wave frequency range at depths approximately below 1200 m.

2-day variances change considerably over time and with depth: A general increase is evident for times of a strong DWBC when particularly high values are found within the bottommost 2000 m. As during phases of a strong DWBC more (or more energetic) internal waves seem to be generated this might subsequently result in local wave breaking close to the seafloor causing the observed increase in high frequency variability. Apart from the increase in the lower part of the water column, elevated energy in high frequencies is also persistently found at the depth

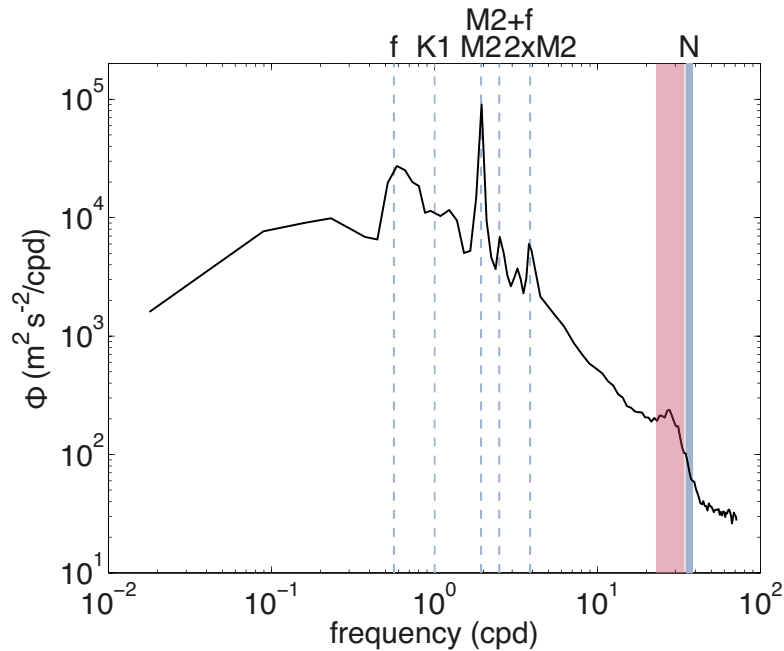


**Figure 8.4:** APE spectra in a depth of approximately 1100 m obtained from data measured by the MOVE mooring at the MAR. A local maximum in  $N$  leads to wave trapping at this depth in the frequency range denoted by the red shading.

of the interface between the DWBC and overlying watermasses where a small local maximum in the buoyancy frequency  $N$  could lead to wave trapping. This trapping of internal waves by a small local maximum in the stratification leads to an increase of internal wave APE slightly below the local buoyancy frequency as they can not leave the depths range of the local maximum in  $N$ . This can be clearly seen in the APE spectra obtained from measurements of the MOVE array at the MAR (Fig. 8.4). Here the overall variability is significantly smaller than within the DWBC and an increase in (high frequency) internal wave energy due to wave trapping can be seen.

As the frequency range in which this wave trapping occurs is not removed by the high-pass filter (cut off frequency of 30 cpd) at depths above approximately 1200 m, the increase in high frequency internal wave energy is visible in the high frequency variability. This is in good agreement with the observed high variance at the continental rise mooring at approximately 1000 m which is independent of the DWBC strength. It is a strong indication that the observed variability in the

high frequency range is related to physical processes and is not induced by noise. At depths below approximately 1200 m 30 cpd is above the permissible frequency range of internal waves and variability with higher frequencies is very likely to be caused by vertical mixing.

The correlations between enhanced vertical mixing during phases of a strong DWBC completes the energy cascade from the large scale DWBC via the generation of internal waves to mixing in the study area and therefore validates the application of parameterizations like those used in Chapter 6.

## 8.4 Vertical propagation of internal waves

A rough estimate of the ray paths of the offshore propagating internal waves generated at the continental slope at the depth of the DWBC core was made using the propagation characteristics given by the dispersion relation for freely propagating internal waves. The propagation direction for internal waves with near inertial and K1 tidal frequencies was determined for a constant stratification and the propagation path was then rescaled to the mean buoyancy frequency profile obtained from the available CTD data using the Wentzel–Kramers–Brillouin (WKB) transformation. As no precise estimate of the vertical and horizontal wavenumbers is available, the effect of the background flow field was omitted.

Near inertial waves generated at the depth of the DWBC core (approximately 2000 m) will propagate along their ray paths (Fig. 8.5) and encounter the mooring locations. However internal waves with frequencies lower than the K1 tidal frequency generated at a depth of 2000 m will not be measured by the mooring at the continental rise at depths shallower than approximately 1000 m due to their nearly horizontal propagation characteristic. This is consistent with the absence of a strong increase in energy of low frequency waves during a strong DWBC at the moorings at shallower depths. The higher spectral levels of horizontal velocities in cross slope direction compared to spectra of along slope direction and higher energy levels at the continental slope mooring compared to energy levels at the continental rise mooring are consistent with the offshore radiation of internal waves generated by the interaction of a strong DWBC with the continental slope

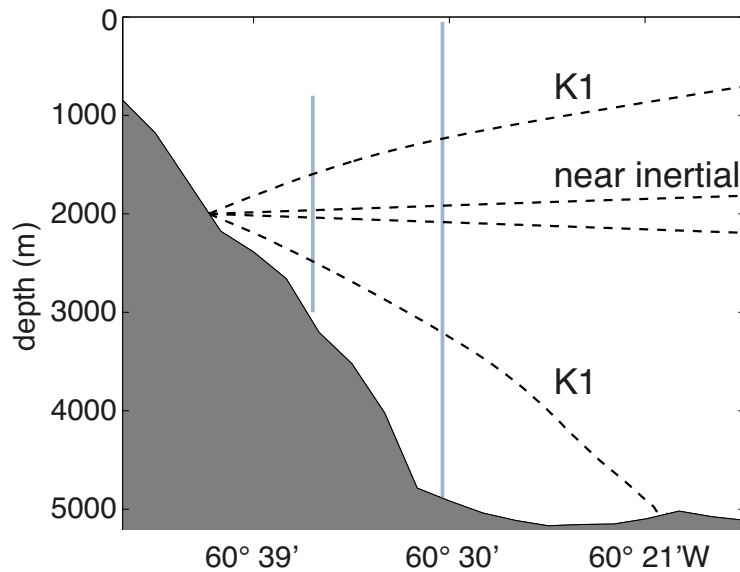


**Figure 8.5:** Internal wave ray paths of K1 and near inertial frequencies generated at the slope at a depth of approximately 2000 m. Mooring positions are denoted by vertical gray lines.

westward of the mooring location.

As internal waves generated at the depths where the DWBC interacts with the slope topography will propagate approximately along the ray paths estimated above, energy propagation will be upward at depths above the DWBC core and downward below. The direction of vertical energy propagation during the different flow situations can be estimated from rotary spectra analysis using shipboard LADCP profiles (Chapter 5.5.4). The left panel in Fig. 8.6 shows the ratio  $r$  of clockwise and counterclockwise spectral components as a function of the distance to the DWBC core depth. The resulting mean profile is in good agreement with the estimated internal wave ray paths for waves generated by the interaction of the DWBC with the topography as the downward energy propagation from the surface is decreasing and reverses into an upward energy transport slightly above the depth which corresponds to the depth at which the DWBC core is found. Below the core the energy propagation direction again reverses to a downward propagation which could correspond to downward propagating near inertial waves generated

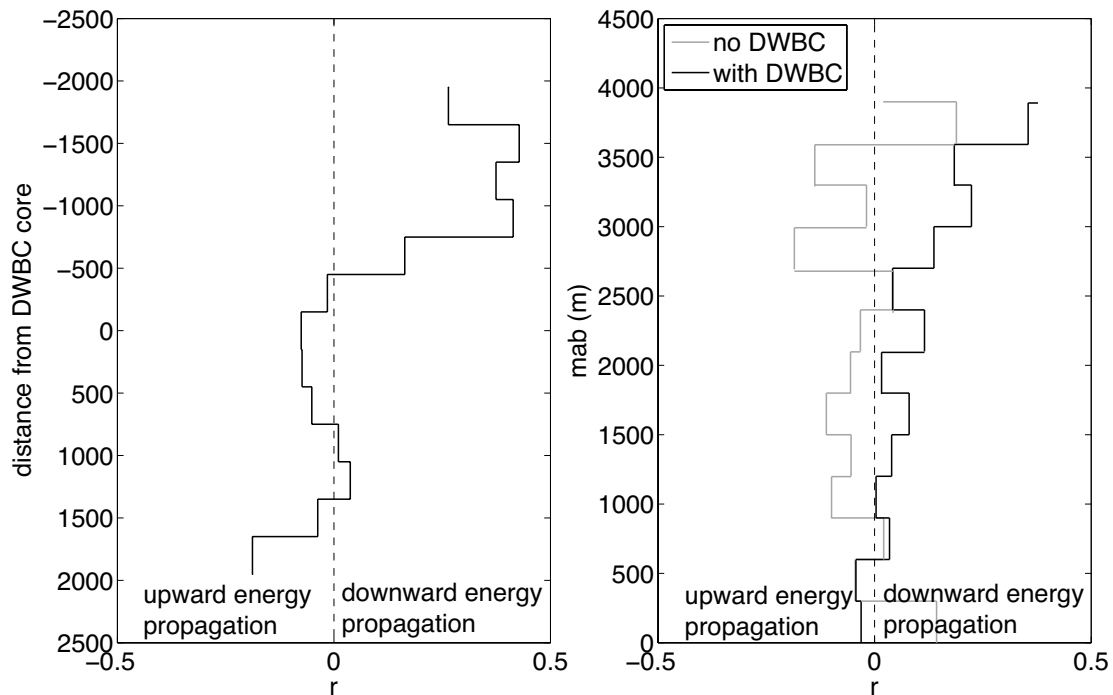


**Figure 8.6:** left: Ratio of downward to upward energy propagation during a strong DWBC as a function of the distance to the DWBC core depth. The depth of the core of the DWBC was determined individually for each cruise (approximately 1300 m for S152, 2000 m for M53/3 and 1200 m for M62/1). Thereby only stations between  $60^\circ 40.2' W$  and  $60^\circ 32.4' W$  were considered as here the DWBC is most pronounced and internal waves generated by the interaction of the DWBC with the slope topography are most likely to show up in the vertical energy propagation direction. right: Ratio of downward to upward propagating energy for both flow situations of a strong (black) and an absent (gray) DWBC at the continental slope as a function of meters above bottom (mab). Negative ratios correspond to upward, positive ratios to downward energy propagation.

by the interaction of the DWBC with the topography. In the deepest part of the mean profile energy propagation is again upward probably due to internal waves generated at the (local) bottom topography, independent from the interaction of the DWBC with the slope topography further to the west. In mean profiles of vertical energy propagation as a function of meters above bottom (right panel in Fig. 8.6) the expected net downward energy flux (positive  $r$ ) is found at depths more than 1000 m above the bottom during phases when the DWBC was flowing over the slope, whereas close to the seafloor (up to 500 mab) there is a mean net upward energy propagation. The downward energy flux in the upper part of the

water column is probably induced by downward propagating near inertial waves which were generated by the wind. The vertical energy propagation is dominantly upward (negative  $r$ ) during times when the DWBC is not flowing over the continental slope except close to the surface where also a downward energy flux is observed.



## 9 | Summary and Conclusions

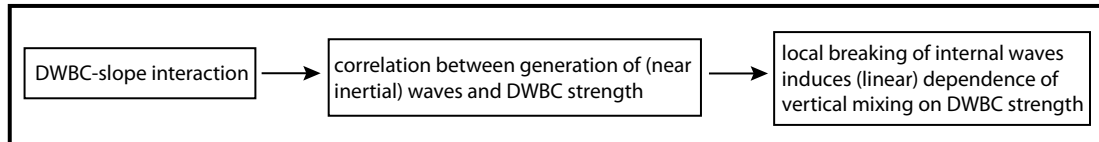


**Figure 9.1:** The DWBC interacts with the topography of the continental slope westward of the mooring locations and generates low frequency, near inertial waves which break and induce a significantly enhanced vertical mixing during phases of a strong flow.

Using five years of continuous mooring data combined with shipboard CTD/LADCP profiles from five cruises, temporal variability on all scales of the energy cascade from the conversion of large scale energy within the DWBC into internal waves and finally into vertical mixing was studied.

The results of this analysis emphasize the importance of the interaction between strong currents and local bottom topography for the internal wave field and the subsequent vertical mixing (Fig. 9.2); the energy in the internal wave field over the continental slope at 16°N in the tropical North Atlantic shows strong variability depending on the strength and location of the DWBC in both time series of horizontal velocities (Chapter 7.1.2) and vertical displacements (Chapter 7.2.2). Most pronounced changes in internal wave energy are thereby found at depths below approximately 1200 m in low frequency, near inertial waves. Mean values of diapycnal diffusivities at the seafloor, obtained from a finestructure parameterization, differ by approximately an order of magnitude between phases when the DWBC is flowing over the continental slope ( $K_\rho \approx 10^{-3} \text{ m}^2 \text{ s}^{-1}$ ) and phases when it is absent ( $K_\rho \approx 10^{-4} \text{ m}^2 \text{ s}^{-1}$ , Chapter 6). Diapycnal diffusivities of  $K_\rho \approx 10^{-3} \text{ m}^2 \text{ s}^{-1}$  are enhanced by approximately two orders of magnitude compared to pelagic values (Ledwell et al., 1993; Kunze and Sanford, 1996; Ledwell et al., 2010) and can be considered as mixing hot spots.

The generation of near inertial waves by the interaction of the DWBC with the

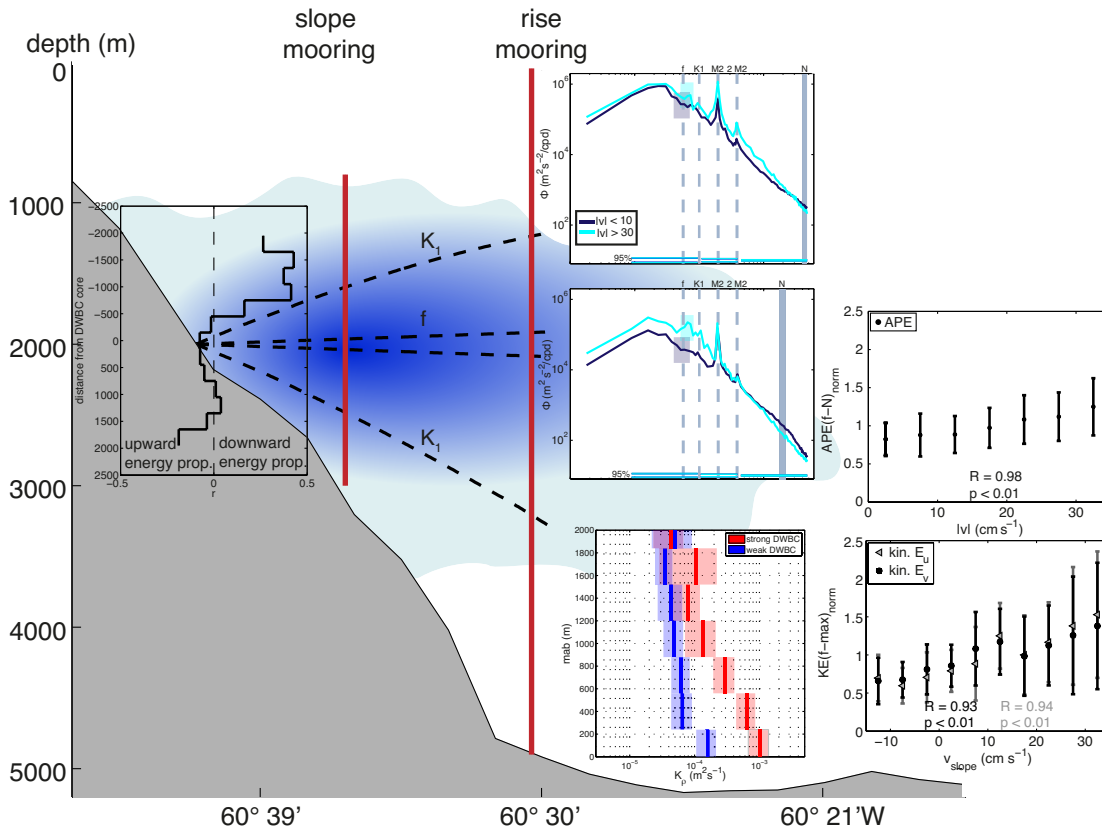


**Figure 9.2:** During phases of a strong DWBC over the continental slope internal waves, primarily with near inertial frequency, are generated westward of the moorings where the local water depth equals the depth of the DWBC core. They propagate offshore and are measured by the moorings at depths below approximately 1200 m consistent with estimated internal wave ray paths of low frequency internal waves. At depths above 1200 m only a small almost constant increase in all frequencies is found. The internal wave energy is linearly related to the flow strength within the DWBC. Local breaking of the internal waves induces significantly enhanced diapycnal mixing in the bottommost 1200 m during phases of a strong DWBC.

slope topography to the west of the mooring locations (where the local water depth equals the depth of the DWBC core) as described by Nikurashin and Ferrari (2010b) is proposed as mechanism leading to the observed increase in low frequency internal waves and associated vertical mixing during phases of a strong DWBC. Thereby energy is transferred from lee waves and waves with harmonic frequencies of  $f$  (forced by inertial currents) to waves with the inertial frequency via a triad interaction. The topography in the vicinity of the mooring location favors such a

---

generation of low frequency, near inertial internal waves as it provides topographic features with wavelengths  $\lambda_t$  that are suitable for the generation of lee waves as well as a strong flow over the slope. For a bottom flow speed of  $U_0 = 0.2 \text{ m s}^{-1}$ , the topographic wavelength range for the radiation of stationary lee waves is between approximately 1.7 km ( $\frac{2\pi}{\lambda_t} < \frac{N}{U_0}$ ) and 30 km ( $\frac{2\pi}{\lambda_t} > \frac{f}{U_0}$ ) in the study area.

Variability in the high frequency range (above the local buoyancy frequency  $N$ ) was shown to be a viable proxy for turbulent mixing (Chapter 8.3). Strongly elevated values were found during strong flows in the bottommost 2000 m and a linear correlation with internal wave energy suggests a local breaking of the generated internal waves inducing vertical mixing. Variance in the high frequency range close to the seafloor (Fig. 8.3) differs by approximately a factor of up to 7–8 between weak and strong flow which is in good agreement with the factor of 10 increase observed in  $K_\rho$  values obtained from the finestructure parameterization.

A local maximum in  $N$  at a depth of approximately 1000 m leads to the trapping of high frequency waves. These waves with frequencies close to the local buoyancy frequency induce high frequency variability in this depth range independent of the DWBC strength.

Vertical energy propagation directions deduced from rotary spectra using LADCP profiles show a divergence of the energy propagation approximately at the depth that corresponds to the depth of the DWBC core (Chapter 8.4). This is in good agreement with the proposed generation of near inertial waves by the interaction of the DWBC with the slope topography to the west of the mooring location where the local water depth equals the depth of the DWBC core.

This study provides observational evidence that in addition to wind generated internal waves and baroclinic tides the generation of (near inertial) internal waves due to flow-topography interactions is another major generation factor of internal waves. Mean internal wave energy at depths below 1200 m increases by approximately a factor of two between weak and strong flow phases (Fig. 7.6) and induces enhanced diapycnal mixing especially at the seafloor. Here it differs by an order of magnitude between phases of a strong or an absent DWBC over the continental slope.

Even though the area covered by the Atlantic DWBC is very small compared to global ocean scales, the observed mechanism is very likely to also play an important

role in many other areas of strong flow like e.g. the Antarctic Circumpolar Current (ACC) where enhanced diapycnal diffusivities were already observed (St. Laurent et al., 2012; Waterman et al., 2012; Sheen et al., 2013) or the Kuroshio Current where shear layers induced by low-frequency internal waves were found by Rainville and Pinkel (2004). The significant response of internal wave energy and diapycnal mixing rates to strong currents like the DWBC interacting with (slope) topography emphasized the importance of including regional characteristics into global budgets of internal wave energy and diapycnal diffusivities as well as in models.

Furthermore these results also point to a possible feedback mechanism between large scale current systems and internal wave energy which subsequently influences vertical mixing rates. These would be affected by a shift of major currents like the DWBC which in turn would feedback on the global circulation.

## 10 | Outlook

The timeseries obtained by the moorings deployed within the MOVE project provide an excellent data basis for the analysis of a long term, statistically significant correlation between the flow speed within the DWBC and changes in the internal wave field. However moored instruments like the  $\chi$ pod (Moum and Nash, 2009) measuring temperature fluctuations with a temporal resolution of 120 Hz allows to infer timeseries of mixing rates. This would permit direct quantitative analyses of the impact of the excess internal wave energy during periods of a strong DWBC on the subsequently induced vertical mixing rates over long time periods. A similar analysis could be carried out with timeseries of closely spaced ( $\Delta z \approx 10$  m) temperature sensors to detect temperature inversions and using Thorpe scales to calculate the corresponding mixing rates.

Microstructure instruments would enable the direct measurements of vertical profiles of energy dissipation without the application of a parameterization. Autonomously profiling microstructure measurement devices are started to be used to obtain timeseries of profiles of energy dissipation in a specified depth range (e.g. D.J. Wain, presentation at "Knowledge for the Future" 2013). Even though they are free floating and therefore drift with the current, they might by a measure to obtain a temporal average of vertical mixing intensity within a relatively small area by direct measurements as single profiles can be highly effected by the patchiness of vertical mixing. However these measurements are still very expensive and time consuming. If in the future measurement devices and processing routines become available for microstructure measurements carried out with a watersampler rosette simultaneously to LADCP/CTD measurements, this would significantly simplify and speed up the measurement of dissipation rates. Even though first tests in this direction are already carried out, obstacles like the tethered operation mode, the rosette movements and the disturbances induced by the rosette itself are at present still difficult to overcome.

Further studies on changes in the characteristics of the internal wave field could

have been carried out using the decomposition of the observed internal wave into normal modes using the available temperature (vertical displacement) timeseries. Thereby information on changes in the vertical structure of the internal wave field, e.g. is it getting (or to what extent) more vertically complex during phases of a strong DWBC?

Additional current meters further up in the water column (within the uppermost 800 m, Alford and Zhao, 2007) would also have permitted a normal mode decomposition of the vertical structure of the internal wave velocity signal and furthermore the estimation of horizontal energy fluxes (Alford and Zhao, 2007):

$$\mathbf{F} = \int_{-H}^0 \langle \mathbf{u}(z') p'(z') \rangle dz' \quad (10.1)$$

where  $\langle \rangle$  denotes an average over one waveperiod and  $p'$  is the baroclinic pressure anomaly. Next to the magnitude of horizontal energy fluxes at the mooring location and the related possible assessment of the significance of this mechanism in relation to other processes or the geographic setting, this would probably yield further information on the main generation site of the observed internal waves. Furthermore the role of tides for energy transport in this setting of very strong background current currents could have been determined.

A more thorough study of the generation of lee waves in combination with the strong background flow within the DWBC subsequently also leading to the generation of the observed near inertial waves would have been possible if high resolution bottom topography data upstream of the mooring location would have been available.

Analyses of the MOVE timeseries obtained at the MAR or the center of the western Atlantic basin could provide insights into other processes that influence the internal wave field and that are masked in the DWBC region by the dominant influence of the flow-topography interaction on the internal wave field. These could include seasonal variations in combination with wind forcing, tides, influences on the internal wave field and vertical mixing rates by critical layers in the stratification due to wave trapping which could also cause the high frequency variability at the continental rise mooring at a depth of approximately 1000 m. In the calmer setting of the mooring at the MAR with less overall variability, wave trapping in

---

the depth range of a local maximum of the buoyancy frequency induces a visible, significant peak just below the local  $N$  in vertical displacement spectra obtained from mooring measurements at a depth of approximately 1100 m (Fig. 8.4). Furthermore the influence of topography and critical topographic angles away from strong currents on the internal wave field could be analyzed using especially mooring timeseries obtained at the MAR. In combination with moored microstructure measurements the long-term quantitative effect of e.g. critical topographic angles on vertical mixing rates could be estimated.



# Bibliography

- Alford, M. and M. Whitmont, 2007: Seasonal and spatial variability of near-inertial kinetic energy from historical moored velocity records. *J. Phys. Oceanogr.*, **37**, 2022–2037.
- Alford, M. and Z. Zhao, 2007: Global patterns of low-mode internal-wave propagation. Part I: Energy and energy flux. *J. Phys. Oceanogr.*, **37** (7), 1829–1848.
- Alford, M. H., 2003: Redistribution of energy available for ocean mixing by long-range propagation of internal waves. *Nature*, **423**, 159–162.
- Alford, M. H., A. Y. Shcherbina, and M. C. Gregg, 2013: Observations of near-inertial internal gravity waves radiating from a frontal jet. *J. Phys. Oceanogr.*, **43** (6), 1225–1239.
- Alford, M. H., et al., 2011: Energy flux and dissipation in Luzon Strait: Two tales of two ridges. *J. Phys. Oceanogr.*, **41** (11), 2211–2222.
- Briscoe, M. G., 1975: Preliminary results from the trimoored internal wave experiment (IWEX). *J. Geophys. Res.*, **80** (27), 3872–3884, doi:10.1029/JC080i027p03872.
- Cairns, J. L. and G. O. Williams, 1976: Internal wave observations from a midwater float, 2. *J. Geophys. Res.*, **81** (12), 1943–1950, doi:10.1029/JC081i012p01943.
- Carter, G. S. and M. C. Gregg, 2002: Intense, variable mixing near the Head of Monterey Submarine Canyon. *J. Phys. Oceanogr.*, **32** (11), 3145–3165.
- D’Asaro, E., C. Lee, L. Rainville, R. Harcourt, and L. Thomas, 2011: Enhanced turbulence and energy dissipation at ocean fronts. *Science*, **332**, 318–322.
- Eden, C. and R. J. Greatbatch, 2008: Diapycnal mixing by meso-scale eddies. *Ocean Modelling*, **23** (3–4), 113 – 120.
- Ellison, T. H., 1957: Turbulent transport of heat and momentum from an infinite

- rough plane. *J. Fluid Mech.*, **2**, 456–466, doi:10.1017/S0022112057000269.
- Eriksen, C. C., 1998: Internal wave reflection and mixing at Fieberling Guyot. *J. Geophys. Res.*, **103 (C2)**, 2977–2944.
- Etopo2, 2001: Global Gridded 2-minute Database. *US Department of Commerce, National Oceanic and Atmospheric Administration, National Geophysical Data Center*, <http://www.ngdc.noaa.gov/mgg/global/etopo2.html>.
- Friedrichs, C. and L. Wright, 1995: Resonant internal waves and their role in transport and accumulation of fine sediment in Eckernförde Bay, Baltic Sea. *Cont. Shelf Res.*, **15 (13)**, 1697 – 1721.
- Garabato, A. C. N., K. L. Polzin, B. A. King, K. J. Heywood, and M. Visbeck, 2004: Widespread intense turbulent mixing in the Southern Ocean. *Science*, **303 (5655)**, 210–213.
- Garrett, C. and W. Munk, 1972a: Space-time scales of internal waves. *Geophys. Fluid Dyn.*, **3 (1)**, 225–264.
- Garrett, C. and W. Munk, 1972b: Space-time scales of internal waves. *Geophys. Fluid Dyn.*, **3 (1)**, 225–264, doi:10.1080/03091927208236082.
- Garrett, C. and W. Munk, 1975: Space-time scales of internal waves: A progress report. *J. Geophys. Res.*, **80 (3)**, 291–297, doi:10.1029/JC080i003p00291.
- Garrett, C. and W. Munk, 1979: Internal Waves in the Ocean. *Annu. Rev. Fluid Mech.*, **11**, 339–369, doi:10.1146/annurev.fl.11.010179.002011.
- Gonella, J., 1972: A rotary-component method for analysing meteorological and oceanographic vector time series. *Deep Sea Research and Oceanographic Abstracts*, **19 (12)**, 833–846.
- Gregg, M. C., 1989: Scaling turbulent dissipation in the thermocline. *J. Geophys. Res.*, **94 (C7)**, 9686–9698, doi:10.1029/JC094iC07p09686.
- Gregg, M. C. and E. Kunze, 1991: Shear and strain in santa monica basin. *Journal of Geophysical Research: Oceans*, **96 (C9)**, 16 709–16 719, doi:10.1029/91JC01385.

- Gregg, M. C., T. B. Sanford, and D. P. Winkel, 2003: Reduced mixing from the breaking of internal waves in equatorial waters. *Nature*, **422 (6931)**, 513–515.
- Hellweger, F. and A. Gordon, 2002: Tracing Amazon River water into the Caribbean Sea. *J. Mar. Res.*, **60 (4)**, 537–549.
- Henry, F. S., 1991: Scaling of internal wave predictions for  $\epsilon$ . *Dynamics of Internal Gravity Waves in the Ocean: Proc. 'Aha Huliko'a Hawaiian Winter Workshop*, Honolulu, HI, University of Hawaii at Manoa, 233–236.
- Jayne, S. R. and L. C. St. Laurent, 2001: Parameterizing tidal dissipation over rough topography. *Geophys. Res. Lett.*, **28 (5)**, 811–814, doi:10.1029/2000GL012044.
- Johnston, T., D. Rudnick, and E. Pallàs-Sanz, 2011: Elevated mixing at a front. *J. Geophys. Res.*, **116**, C11 033, doi:10.1029/2011JC007192.
- Jones, W. L., 1968: Reflexion and stability of waves in stably stratified fluids with shear flow: a numerical study. *J. Fluid Mech.*, **34**, 609–624, doi:10.1017/S0022112068002119.
- Kalnay, E., et al., 1996: The NCEP/NCAR 40-year reanalysis project. *Bull. Amer. Meteor. Soc.*, **77 (3)**, 437–471.
- Kanzow, T., U. Send, and M. McCartney, 2008: On the variability of the deep meridional transports in the tropical North Atlantic. *Deep-Sea Res. I*, **55 (12)**, 1601–1623.
- Kanzow, T., U. Send, W. Zenk, A. D. Chave, and M. Rhein, 2006: Monitoring the integrated deep meridional flow in the tropical North Atlantic: Long-term performance of a geostrophic array. *Deep-Sea Res. I*, **53 (3)**, 528–546.
- Kirchner, K., M. Rhein, C. Mertens, C. W. Böning, and S. Hüttl, 2008: Observed and modeled meridional overturning circulation related flow into the Caribbean. *J. Geophys. Res.*, **113 (C3)**, C03 028, doi:10.1029/2007JC004320.
- Klymak, J. M., et al., 2006: An estimate of tidal energy lost to turbulence at the Hawaiian Ridge. *J. Phys. Oceanogr.*, **36 (6)**, 1148–1164.

- Kuhlbrodt, T., A. Griesel, M. Montoya, A. Levermann, M. Hofmann, and S. Rahmstorf, 2007: On the driving processes of the Atlantic meridional overturning circulation. *Rev. Geophys.*, **45** (2), doi:10.1029/2004RG000166.
- Kundu, P. and I. Cohen, 2008: Fluid mechanics. *Academic Press*.
- Kunze, E., 1985: Near-inertial wave propagation in geostrophic shear. *J. Phys. Oceanogr.*, **15** (5), 544–565.
- Kunze, E., E. Firing, J. M. Hummon, T. K. Chereskin, and A. M. Thurnherr, 2006: Global abyssal mixing inferred from Lowered ADCP shear and CTD strain profiles. *J. Phys. Oceanogr.*, **36** (8), 1553–1576.
- Kunze, E. and T. B. Sanford, 1986: Near-inertial wave interactions with mean flow and bottom topography near Caryn Seamount. *J. Phys. Oceanogr.*, **16**, 109–120.
- Kunze, E. and T. B. Sanford, 1996: Abyssal mixing: Where it is not. *J. Phys. Oceanogr.*, **26** (10), 2286–2296.
- Kunze, E., A. J. Williams, and M. G. Briscoe, 1990: Observations of shear and vertical stability from a neutrally buoyant float. *Journal of Geophysical Research: Oceans*, **95** (C10), 18 127–18 142, doi:10.1029/JC095iC10p18127.
- Lauderdale, J. M., S. Bacon, A. C. Naveira Garabato, and N. P. Holliday, 2008: Intensified turbulent mixing in the boundary current system of southern Greenland. *Geophys. Res. Lett.*, **35** (4), L04611, doi:10.1029/2007GL032785.
- Leaman, K. D. and T. B. Sanford, 1975: Vertical energy propagation of inertial waves: A vector spectral analysis of velocity profiles. *J. Geophys. Res.*, **80**, 1975–1978, doi:10.1029/JC080i015p01975.
- Ledwell, J. R., E. T. Montgomery, K. L. Polzin, L. C. St. Laurent, R. W. Schmitt, and J. M. Toole, 2000: Evidence for enhanced mixing over rough topography in the abyssal ocean. *Nature*, **403** (6766), 179–182.
- Ledwell, J. R., L. C. St. Laurent, J. B. Girton, and J. M. Toole, 2010: Diapycnal mixing in the Antarctic Circumpolar Current. *J. Phys. Oceanogr.*, **41** (1), 241–246.

- Ledwell, J. R., A. J. Watson, and C. S. Law, 1993: Evidence for slow mixing across the pycnocline from an open-ocean tracer-release experiment. *Nature*, **364**, 701–703.
- Levine, M. D., 2002: A modification of the garrett–munk internal wave spectrum. *J. Phys. Oceanogr.*, **32** (11), 3166–3181.
- Liang, X. and A. M. Thurnherr, 2012: Eddy-modulated internal waves and mixing on a midocean ridge. *J. Phys. Oceanogr.*, **42** (7), 1242–1248.
- Mauritzen, C., K. L. Polzin, M. S. McCartney, R. C. Millard, and D. E. West-Mack, 2002: Evidence in hydrography and density fine structure for enhanced vertical mixing over the Mid-Atlantic Ridge in the western Atlantic. *J. Geophys. Res.*, **107** (C10), doi:10.1029/2001JC001114.
- McComas, C. H. and F. P. Bretherton, 1977: Resonant interaction of oceanic internal waves. *J. Geophys. Res.*, **82**, 1397–1412.
- Moum, J. N. and J. D. Nash, 2009: Mixing measurements on an equatorial ocean mooring. *J. Atmos. Oceanic Technol.*, **26** (2), 317–336.
- Müller, P. and M. Briscoe, 2000: Diapycnal mixing and internal waves. *Oceanography*, **13** (2), 98–103.
- Müller, P., D. J. Olbers, and J. Willebrand, 1978: The Iwex spectrum. *Journal of Geophysical Research: Oceans*, **83** (C1), 479–500, doi:10.1029/JC083iC01p00479.
- Munk, W., 1981: Internal waves and small scale processes. *Evolution of Physical Oceanography*.
- Munk, W. and C. Wunsch, 1998: Abyssal recipes II: energetics of tidal and wind mixing. *Deep-Sea Res. I*, **45** (12), 1977 – 2010, doi:DOI:10.1016/S0967-0637(98)00070-3.
- Munk, W. H., 1966: Abyssal recipes. *Deep Sea Research and Oceanographic Abstracts*, **13** (4), 707–730.
- Nikurashin, M. and R. Ferrari, 2010a: Radiation and dissipation of internal waves

- generated by geostrophic motions impinging on small-scale topography: Application to the Southern Ocean. *J. Phys. Oceanogr.*, **40** (9), 2025–2042.
- Nikurashin, M. and R. Ferrari, 2010b: Radiation and dissipation of internal waves generated by geostrophic motions impinging on small-scale topography: Theory. *J. Phys. Oceanogr.*, **40** (5), 1055–1074.
- Nikurashin, M. and R. Ferrari, 2011: Global energy conversion rate from geostrophic flows into internal lee waves in the deep ocean. *Geophys. Res. Lett.*, **38** (8), doi:10.1029/2011GL046576.
- Nikurashin, M. and S. Legg, 2011: A mechanism for local dissipation of internal tides generated at rough topography. *J. Phys. Oceanogr.*, **41** (2), 378–395.
- Nikurashin, M., G. K. Vallis, and A. Adcroft, 2013: Routes to energy dissipation for geostrophic flows in the Southern Ocean. *Nature Geosci.*, **6** (1), 48–51.
- Osborn, T. R., 1980: Estimates of the local rate of vertical diffusion from dissipation measurements. *J. Phys. Oceanogr.*, **10** (1), 83–89.
- Polzin, K. L. and Y. V. Lvov, 2011: Toward regional characterizations of the oceanic internal wavefield. *Rev. Geophys.*, **49**, RG4003.
- Polzin, K. L., J. M. Toole, J. R. Ledwell, and R. W. Schmitt, 1997: Spatial variability of turbulent mixing in the abyssal ocean. *Science*, **276** (5309), 93–96.
- Polzin, K. L., J. M. Toole, and R. W. Schmitt, 1995: Finescale parameterizations of turbulent dissipation. *J. Phys. Oceanogr.*, **25** (3), 306–328.
- Rainville, L. and R. Pinkel, 2004: Observations of energetic high-wavenumber internal waves in the Kuroshio. *J. Phys. Oceanogr.*, **34** (7), 1495–1505.
- Rhein, M., K. Kirchner, C. Mertens, R. Steinfeldt, M. Walter, and U. Fleischmann-Wischnath, 2005: Transport of South Atlantic water through the passages south of Guadeloupe and across 16°N, 2000–2004. *Deep-Sea Res. I*, **52** (12), 2234–2249.
- Rhein, M., L. Stramma, and U. Send, 1995: The Atlantic Deep Western Boundary Current: Water masses and transports near the equator. *Journal of Geophysical*

- Research: Oceans*, **100 (C2)**, 2441–2457, doi:10.1029/94JC02355.
- Rhein, M., M. Walter, C. Mertens, R. Steinfeldt, and D. Kieke, 2004: The circulation of North Atlantic Deep Water at 16°N, 2000-2003. *Geophys. Res. Lett.*, **31 (14)**, 4, 114305, doi:10.1029/2005GL023568.
- Sandstrom, H. and J. A. Elliott, 1984: Internal tide and solitons on the Scotian Shelf: A nutrient pump at work. *J. Geophys. Res.*, **89 (C4)**, 6415–6426.
- Schott, F. A., J. Fischer, and L. Stramma, 1998: Transports and pathways of the upper-layer circulation in the western tropical Atlantic. *J. Phys. Oceanogr.*, **28 (10)**, 1904–1928.
- Scott, R. B., J. A. Goff, A. C. Naveira Garabato, and A. J. G. Nurser, 2011: Global rate and spectral characteristics of internal gravity wave generation by geostrophic flow over topography. *J. Geophys. Res.*, **116 (C9)**, C09029, doi:10.1029/2011JC007005.
- Send, U., M. Lankhorst, and T. Kanzow, 2011: Observation of decadal change in the Atlantic meridional overturning circulation using 10 years of continuous transport data. *Geophys. Res. Lett.*, **38 (24)**, L24606, doi:10.1029/2011GL049801.
- Shcherbina, A. Y., L. D. Talley, E. Firing, and P. Hacker, 2003: Near-surface frontal zone trapping and deep upward propagation of internal wave energy in the Japan/East Sea. *J. Phys. Oceanogr.*, **33**, 900–912.
- Sheen, K. L., et al., 2013: Rates and mechanisms of turbulent dissipation and mixing in the Southern Ocean: Results from the diapycnal and isopycnal mixing experiment in the southern ocean (DIMES). *Journal of Geophysical Research: Oceans*, **118 (6)**, 2774–2792, doi:10.1002/jgrc.20217.
- St. Laurent, L. and C. Garrett, 2002: The role of internal tides in mixing the deep ocean. *J. Phys. Oceanogr.*, **32 (10)**, 2882–2899.
- St. Laurent, L., A. C. Naveira Garabato, J. R. Ledwell, A. M. Thurnherr, J. M. Toole, and A. J. Watson, 2012: Turbulence and diapycnal mixing in Drake Passage. *J. Phys. Oceanogr.*, **42 (12)**, 2143–2152.

- Stöber, U., M. Walter, C. Mertens, and M. Rhein, 2008: Mixing estimates from hydrographic measurements in the Deep Western Boundary Current of the North Atlantic. *Deep-Sea Res. I*, **55** (6), 721 – 736.
- Tandon, A. and C. Garrett, 1996: On a recent parameterization of mesoscale eddies. *J. Phys. Oceanogr.*, **26** (3), 406–411.
- Tennekes, H. and J. L. Lumley, 1972: *A first course in turbulence*. The MIT press.
- Thorpe, S. A., 1975: The excitation, dissipation, and interaction of internal waves in the deep ocean. *J. Geophys. Res.*, **80**, 328–338.
- Thorpe, S. A., 2005: *The turbulent ocean*. Cambridge University Press.
- Thurnherr, A. M., 2012: The finescale response of Lowered ADCP velocity measurements processed with different methods. *J. Atmos. Oceanic Technol.*, **29** (4), 597–600.
- van Haren, H., L. Maas, and H. van Aken, 2002: On the nature of internal wave spectra near a continental slope. *Geophys. Res. Lett.*, **29** (12), doi:10.1029/2001GL014341.
- Visbeck, M., 2002: Deep velocity profiling using lowered acoustic doppler current profilers: Bottom track and inverse solutions. *J. Atmos. Oceanic Technol.*, **19** (5), 794–807.
- Walter, M. and C. Mertens, 2013: Mid-depth mixing linked to North Atlantic Current variability. *Geophys. Res. Lett.*, doi:10.1002/grl.50936.
- Walter, M., C. Mertens, and M. Rhein, 2005: Mixing estimates from a large-scale hydrographic survey in the North Atlantic. *Geophys. Res. Lett.*, **32** (13), doi: 10.1029/2005GL022471.
- Walter, M., et al., 2010: Rapid dispersal of a hydrothermal plume by turbulent mixing. *Deep Sea Research Part I: Oceanographic Research Papers*, **57** (8), 931–945.
- Waterman, S., A. C. Naveira Garabato, and K. L. Polzin, 2012: Internal waves and Turbulence in the Antarctic Circumpolar Current. *J. Phys. Oceanogr.*, **43** (2),

259–282.

Watson, A. J., J. R. Ledwell, M.-J. Messias, B. A. King, N. Mackay, M. P. Meredith, B. Mills, and A. C. Naveira Garabato, 2013: Rapid cross-density ocean mixing at mid-depths in the Drake Passage measured by tracer release. *Nature*, **501 (7467)**, 408–411.

Wunsch, C. and R. Ferrari, 2004: Vertical Mixing, Energy, and the General Circulation of the Oceans. *Annu. Rev. Fluid Mech.*, **36**, 281–314, doi: 10.1146/annurev.fluid.36.050802.122121.

Wyrski, K., 1961: The thermohaline circulation in relation to the general circulation in the oceans. *Deep Sea Research (1953)*, **8 (1)**, 39 – 64.



# Publications

I presented preliminary results of this study on the following international conferences, workshop and in seminars as first author:

Köhler, J., Walter, M., Mertens, C., Stöber, U., Kanzow, T. and M. Rhein, *Temporal variability in the internal wave field and associated mixing in the Atlantic Deep Western Boundary Current* at the "6<sup>th</sup> Warnemünder Turbulence Days – Turbulent processes below the mesoscale" on Vilm, Germany. August 2013, talk.

Köhler, J., Walter, M., Mertens, C., Stöber, U., Kanzow, T. and M. Rhein, *Variability in the internal wave field and associated mixing in the western tropical Atlantic* at the IAHS-IAPSO-IAPSEI General Assembly „Knowledge for the Future“ in Gothenburg, Sweden. June 2013, talk.

Köhler, J., Walter, M., Mertens, C., Kanzow, T. and M. Rhein, *How does the DWBC influence the internal wave field?* in the oceanographic seminar at the University of Hawaii at Manoa, USA. June 2012, talk.

Köhler, J., Mertens, C., Walter, M., Kanzow, T., and M. Rhein, *Temporal variability of the generation of near internal waves by the Deep Western Boundary Current at 16°N* at the AGU Ocean Science Meeting in Salt Lake City, USA. February 2012, poster.

Köhler, J., Mertens, C., Walter, M., Rhein, M., and T. Kanzow, *Internal waves and associated mixing in the Deep Western Boundary Current at 16°N* at the European Geosciences Union General Assembly in Vienna, Austria. April 2011, talk.

Results of this study are accepted for publication in Journal of Physical Oceanography:

Janna Köhler, Christian Mertens, Maren Walter, Uwe Stöber, Monika Rhein and Torsten Kanzow: *Variability in the internal wave field induced by the Atlantic Deep Western Boundary Current at 16° N.*

# Acknowledgments

There are many persons who strongly supported me in multiple ways during my PhD time and without whom this thesis would not exist. First of all I want to thank Maren Walter and Christian Mertens who always had an open door and two open ears for me. They made sure I did not get lost in the data and provided valuable advice and encouragement when it was needed. Thank you very much!

Prof. Monika Rhein not only gave me the opportunity to write this thesis but also supported me in many ways with her positive, supportive and reassuring attitude as well as with her scientific knowledge. I want to thank Prof. Torsten Kanzow who made available his support in a number of ways by kindly providing the (pre-processed) mooring data, by giving valuable feedback and support in the process of writing the manuscript accepted for publication in *Journal of Physical Oceanography* and by being the co-evaluator of this thesis. Furthermore this study would not have been possible without the continuous efforts of Prof. Uwe Send and his co-workers in maintaining the MOVE array.

Special thanks go to Antje Buss who was a perfect office mate and provided support in many ways as well as Uwe Stöber who had to endure endless questions which he patiently answered. During the entire time I was strongly supported by all members of the oceanography working group in numerous ways either by giving technical support, scientific input, encouragement, tips for the presentation of results or advice of all sorts.

The membership in the Bremen International Graduate School for Marine Sciences "GLOMAR" gave me the opportunity to participate in several international conferences, workshops, a mentoring program and for a research stay in the department of oceanography at the University of Hawaii at Manoa by giving financial support. Moreover their soft skill and scientific course program was of great value during my PhD thesis and will be helpful in the future. The very friendly and competent support by the scientific coordinator of GLOMAR Dr. Christina Klose is highly appreciated as well as the support provided by Prof. Carsten Eden who agreed to

be a member of my thesis committee.

Furthermore I want to thank Prof. Glenn Carter of the School of Ocean and Earth Science and Technology at the University of Hawai'i for giving me the opportunity for a research stay, to participate in a research cruise in the Samoa Passage and for helpful and interesting scientific discussions. During this stay as well as during the cruise I had the chance to discuss my work with a large number of people whose support is highly appreciated.

Last but not least I want to thank my parents who supported me in every possible way. They sometimes had a hard time coping with their highly strung daughter but still they never ceased to back me up!